

# REPORT DOCUMENTATION PAGE

AFRL-SR-BL-TR-01-  
0278

Public reporting burden for this collection of information is estimated to average 1 hour per response, including the time for reviewing the data needed, and completing and reviewing this collection of information. Send comments regarding this burden estimate or any other aspect of this collection of information to Washington Headquarters Services, Directorate for Information Operations and Reports, 1215 Jefferson Management and Budget, Paperwork Reduction Project (0704-0188), Washington, DC 20503.

Training  
is for  
use of

1. AGENCY USE ONLY (Leave blank)			2. REPORT DATE 01/15/01	3. REPORT TYPE AND DATES COVERED Final Technical Report 09/01/96 - 08/31/00
4. TITLE AND SUBTITLE Electron Transfer Chemistry in Optical Materials: An EPR Investigation of Radiation-Induced Defects in Chemically Modified Materials			5. FUNDING NUMBERS Grant F49620-96-1-0443 Acct. Z1144/429319	
6. AUTHOR(S) David J. Singel				
7. PERFORMING ORGANIZATION NAME(S) AND ADDRESS(ES) Montana State University Bozeman, MT 59717			8. PERFORMING ORGANIZATION REPORT NUMBER	
9. SPONSORING / MONITORING AGENCY NAME(S) AND ADDRESS(ES) Air Force Office of Scientific Research 801 North Randolph Street Room 732 Arlington, VA 22203-1977			10. SPONSORING / MONITORING AGENCY REPORT NUMBER	
11. SUPPLEMENTARY NOTES				
12a. DISTRIBUTION / AVAILABILITY STATEMENT Unlimited Access			12b. DISTRIBUTION CODE AIR FORCE OFFICE OF SCIENTIFIC RESEARCH (AFOSR) NOTICE OF TRANSMITTAL DTIC. THIS TECHNICAL REPORT HAS BEEN REVIEWED AND IS APPROVED FOR PUBLIC RELEASE LAW AFR 190-12. DISTRIBUTION IS UNLIMITED.	
13. ABSTRACT (Maximum 200 Words)  The Final Technical Report for Grant F49620-96-1-0443 "Electron Transfer Chemistry in Optical Materials: an EPR Investigation of Radiation-Induced Defects in Chemically Modified Materials" details the construction, and Performance-evaluation of a 94.9 GHz EPR (electron paramagnetic resonance) spectrometer, operating in both CW (continuous wave) and pulsed modes. The first application of this instrument in the study of radiation induced defects in optical materials – a neutron-irradiated $\alpha$ -Al <sub>2</sub> O <sub>3</sub> single crystal fiber, and $\gamma$ -irradiated of vitreous silica samples – are also described. A major finding of this work is that, owing to excellent sensitivity for volume-limited samples, high-frequency EPR instrumentation makes it possible to characterize paramagnetic centers in <i>optical fibers</i> . This capability is illustrated by reported spectroscopic, line shape, and analytical studies of Cr <sup>3+</sup> , Fe <sup>3+</sup> , and color centers (electrons trapped at anion vacancies) at ppm levels in an $\alpha$ -Al <sub>2</sub> O <sub>3</sub> fiber. Special characteristics of high-magnetic fields for improving and facilitating EPR spectroscopy and analysis (spin-counting) are detailed. An emergent feature of high-frequency EPR spectroscopy is the apparent ease of eliciting saturation and rapid passage effects. Pioneering efforts in the systematic characterization and theoretical simulation of these effects are reported. Preliminary results suggest that passage effects can be harnessed to provide enhanced sensitivity and pronounced relaxation-dependent selectivity in the EPR spectroscopy.				
14. SUBJECT TERMS			15. NUMBER OF PAGES 101	
			16. PRICE CODE	
17. SECURITY CLASSIFICATION OF REPORT Unclassified	18. SECURITY CLASSIFICATION OF THIS PAGE Unclassified	19. SECURITY CLASSIFICATION OF ABSTRACT Unclassified	20. LIMITATION OF ABSTRACT Unlimited Access	

NSN 7540-01-280-5500

Standard Form 298 (Rev. 2-89)  
Prescribed by ANSI Std. Z39-18  
298-102

01-30-01 A 07:47 RCV'D

**Final Technical Report**

*Grant F49620-96-1-0443*

*Acct Z1144/429 319*

**Electron Transfer Chemistry in Optical Materials:  
An EPR Investigation of Radiation-Induced Defects in Chemically  
Modified Materials**

*David J. Singel*

*Department of Chemistry and Optical Technology Center  
Montana State University  
Bozeman, MT*

**20010427 096**

## Executive Summary

The Final Technical Report for Grant F49620-96-1-0443 "Electron Transfer Chemistry in Optical Materials: an EPR Investigation of Radiation-Induced Defects in Chemically Modified Materials" details the construction, and performance-evaluation of a 94.9 GHz EPR (electron paramagnetic resonance) spectrometer, operating in both CW (continuous wave) and pulsed modes. The first application of this instrument in the study of radiation induced defects in optical materials – neutron-irradiated  $\alpha$ -Al<sub>2</sub>O<sub>3</sub> single crystal fiber, and  $\gamma$ -irradiated of vitreous silica samples – are also described.

A major finding of this work is that, owing to its excellent sensitivity for volume-limited samples, high-frequency EPR instrumentation makes it possible to characterize paramagnetic centers in *optical fibers*. This capability is illustrated by reported spectroscopic, line shape, and analytical studies of Cr<sup>3+</sup>, Fe<sup>3+</sup>, and color centers (electrons trapped at anion vacancies) at ppm levels in an  $\alpha$ -Al<sub>2</sub>O<sub>3</sub> fiber. Special characteristics of high-magnetic fields for improving and facilitating EPR spectroscopy and analysis (spin-counting) are detailed.

An emergent feature of high-frequency EPR spectroscopy is the apparent ease of eliciting saturation and rapid passage effects. Pioneering efforts in the systematic characterization and theoretical simulation of these effects are reported. Preliminary results suggest that passage effects can be harnessed to provide enhanced sensitivity and pronounced relaxation-dependent selectivity in the EPR spectroscopy.

The personnel that participated in this work are:

David J. Singel, PI; Vladimir Krymov, Visiting Scientist for the Physico-Technical Institute Donetsk; Dwight A. Schwartz, postdoctoral research associate; Eric D. Walter, graduate student research assistant; and Sean J. McIlwain, undergraduate research aide.

Publications and presentations emanating from this work are listed below:

- “High-Frequency (94.9 GHz) EPR Spectroscopy of a Spin 3/2 Center in a Neutron-Irradiated Sapphire Single Crystal.” D.A. Schwartz, Eric D. Walter, Sean J. McIlwain, Vladimir N. Krymov, and David J. Singel, *Appl. Magn. Res.* (1999) **16** 223-236.
- “EPR Studies of Optical Materials: Characterization and Control” Invited Lecture, OpTeC Conference on Optical Science and Laser Technology, Bozeman, MT September 1995.
- “Magnetic Resonance Spectroscopy of Optical Materials” Invited Lecture, OpTeC Conference on Optical Science and Laser Technology, Bozeman, MT. August 1997.
- “High Field EPR Spectroscopy of Optical Materials” Invited Lecture, Optical Science and Laser Technology Conference, Bozeman, MT. August 1998.
- “Experts Workshop on High Field EPR Spectroscopy”, Workgroup Leader, Washington, DC. September 1998.
- “High Field EPR Spectroscopy of Optical Materials OpTeC Conference on Optical Science and Laser Technology, Bozeman, MT. August 1999.
- “Passage Effects in High-frequency EPR Spectroscopy of Optical Materials“ OpTeC Conference on Optical Science and Laser Technology, Bozeman, MT. August 2000.
- “Passage Effects in High-frequency EPR Spectroscopy” Invited Lecture, International conference on Magnetic Resonance, Florence, Italy 2000.

## Table of Contents

Standard From 298	Cover Page	
<b>Title Page</b>	i	
<b>Executive Summary</b>	ii	
<b>Table of Contents</b>	iii	
<b>Project Summary</b>		
1.	Introduction	1-2
2.	Instrumentation	3-5
3.	Experiments and Results	5-22
3.1	Neutron Irradiated Sapphire Single-crystal Fiber	5-12
3.2	$\gamma$ -Irradiated Vitreous Fused Silica	12-21
4.	Literature Cited	22-25
<b>Appendices</b>		
Appendix I	Schematics and Specifications of the 94.9 GHz Microwave Bridge	I-1 I-19
Appendix II	LabVIEW Code for EPR Spectrometer Control, Data Acquisition, and Manipulations	II-1 II-10
Appendix III	Search for High-Field Zeeman Effects in the 94.9 GHz EPR Spectrum of Cr <sup>3+</sup> in $\alpha$ -Al <sub>2</sub> O <sub>3</sub>	III-1 III-21
Appendix IV	C++ Code for Simulation Of Rapid Passage Effects in High-frequency EPR	IV-1 IV-15

## 1. Introduction

The research program on “Electron Transfer Chemistry in Optical Materials ” at Montana State University had two primary objectives:

- Development and implementation of a high-frequency (94.9 GHz) EPR instrument;
- Application of high-frequency EPR spectroscopy to redox active centers in solid-state materials, in particular, materials of interest in opto-electronics.

This report provides technical details on the instrument that has been constructed at Montana State University, and results obtained in the initial experimental work undertaken with the instrument.

Since its earliest days of application, EPR (electron magnetic resonance) spectroscopy has conventionally been performed at operating frequencies of order  $10^1$  GHz. Following the pioneering efforts of the Lebedev group in Moscow [1], there is currently a surge of interest in the development and application of EPR spectroscopy at “high” frequencies, of order  $10^2$  GHz. This interest is more developed in the European community than in the United States. There is and multinational workgroup on high-frequency EPR in Europe, featuring numerous research groups in over 8 nations. In the United States, by contrast progress in this field has been slow. *The system implemented at Montana State University is only high-frequency instrument west of the Mississippi River, and one of only a few instruments in the country capable of operation in both pulsed and CW modes.*

The leap in spectrometer frequency from ~9.5 to 95 GHz, with its corresponding impact on external magnetic field strengths, provides a powerful means to alter the balance between the Zeeman and non-Zeeman interactions (electron-nuclear hyperfine and electron-electron fine structure interactions) of a spin system, and thus, to alter their relative importance in shaping the

spectral display. An important goal of such manipulations is to forge a stronger link between the features of a spectrum and the physical quantities to be measured. For example, in arguably the most fruitful realm of application, high fields are used to magnify the spectral effects of Zeeman anisotropy in free-radicals, so that the Zeeman powder pattern is prominently featured in the spectral display. High-frequency EPR thus promotes direct, precise measurement of the principal values (g-values) of the Zeeman interaction, and thereby facilitates the identification of the radical and the characterization of its environment [1,2]. Conversely, high fields have also been utilized to reduce line-broadening effects in the central transitions of  $Mn^{2+}$  ions, thereby heightening sensitivity to hyperfine interactions [3]. There are a number of additional important benefits that high-frequency EPR spectroscopy can afford. Most notably is the promise of high sensitivity in volume limited samples. This feature has especially important ramifications for the study optical fiber materials. In previous EPR studies of such systems investigators studied “preforms” – the bulk material from which fibers are drawn. ***The work detailed is the first demonstration that high-frequency EPR brings high sensitivity to the study of paramagnetic centers in fibers, including both metal ion inclusions and radiation induced “free-electron” defects.***

An final feature of interest is the utility in the study of high-multiplicity spin systems - in particular, systems that have zero-field splittings which are comparable to the microwave frequency,  $\nu_0$ , of conventional spectrometers, and therefore are considerably smaller than  $\nu_0$  in “high-frequency” instruments. ***The work presented here shows that high-frequency EPR leads to a simplification of the otherwise complicated spectra.*** Such simplification enables improved quantification both of the number of paramagnetic centers and the parameters that determine the spectrum.

## 2. Instrumentation

The high-frequency EPR instrument that was constructed at Montana State University entails:

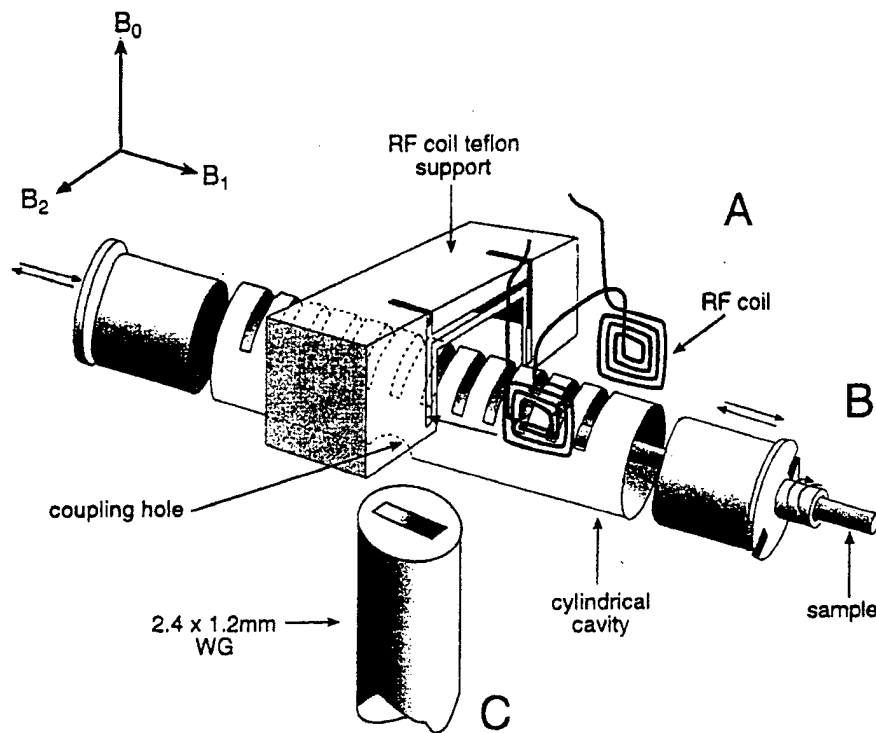
- an Oxford Instruments Teslatron split-pair superconducting magnet system with “intelligent” power supply (IPS-120-10) for operation from 0-3.7 T;
- a 94.9 GHz microwave bridge obtained from collaborators at the Physico-Technical Institute of Donetsk, Ukraine;
- a TE011 cavity assembly made by collaborators at the Physico-Technical Institute of Donetsk, Ukraine;
- a probe - constructed locally - that links the bridge and cavity, and provides for cavity-tuning, microwave coupling, sample rotation, and field modulation. The installation of the bridge, and the design and implementation of the probe was done by Vladimir Krymov of Donetsk, while at Montana State University.

The magnet system allows for computer-controlled sweeping of the field exerted by the split-pair, over an operating range of 0 - 3.7 T, with a maximum rate of 0.33 T/min and a resolution of 3.3  $\mu$ T. Further details of the system are available from Oxford Instruments. The fixed current leads of the magnet are optimized for low helium consumption while sweeping the field through its full range. For many spin systems, in particular those with appreciable fine-structure interactions, high-frequency EPR spectroscopy requires wide-ranging field sweeps. The requirement argues against magnet systems in which current is swept in an auxiliary, rather than the main, magnet coil. While such dual coil systems are thought to enjoy a compelling advantage in substantially reduced helium consumption, the magnet system implemented in this work, with its optimized current lead configuration, gives satisfactory performance: less than 100 liters were required during the first month of continuous operation. The magnetic field was calibrated, for these measurements, by the method of Burghaus and Möbius [13]. The calibrated

value of the field consistently lay within 9 G of the nominal value on the Oxford Teslatron display.

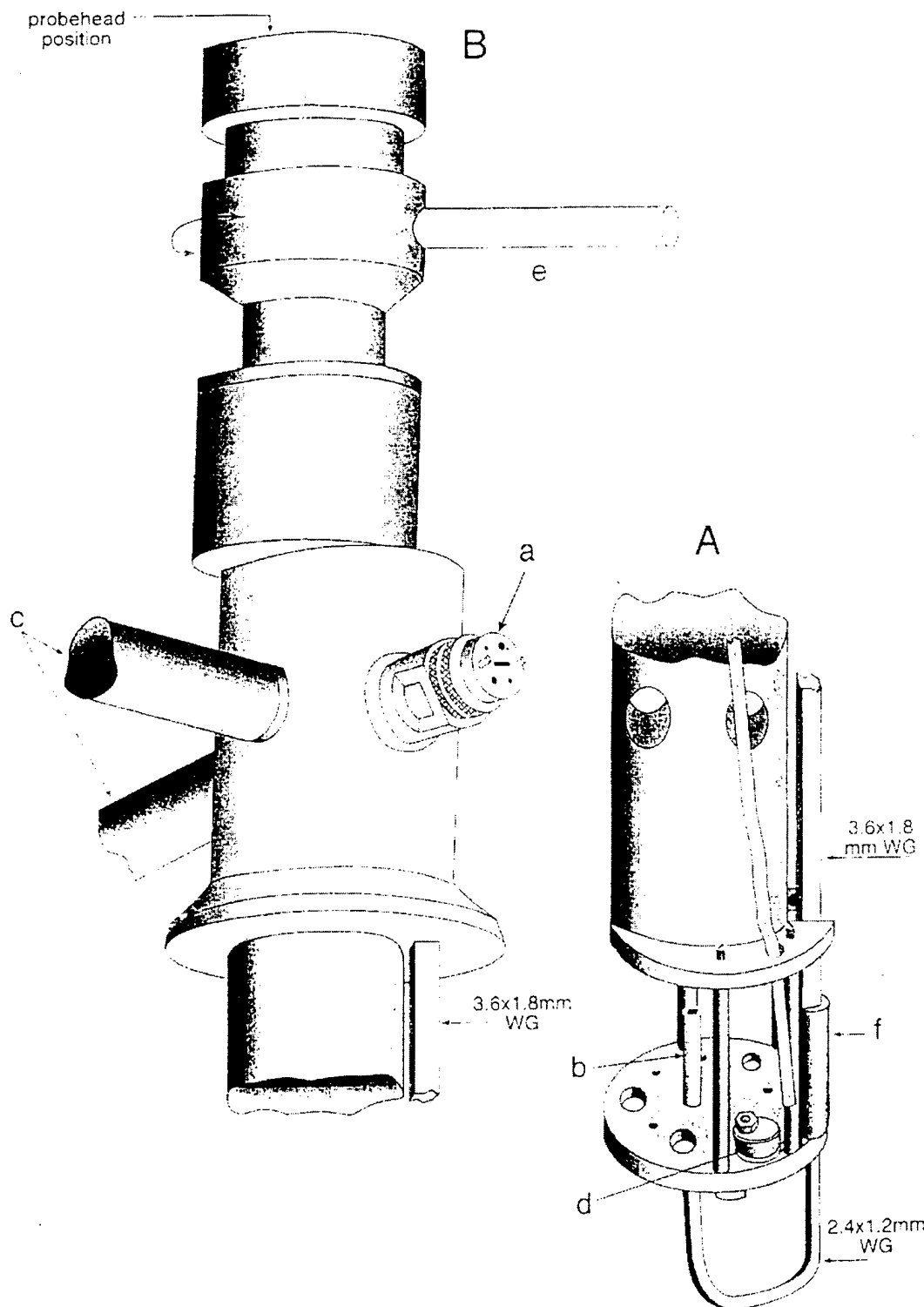
The bridge features a highly stabilized oscillator (STAMO) with a fixed frequency of 94.9 GHz; operation entails both pulsed and CW (continuous-wave) modes. The maximum microwave field in the cavity is ~3.6 G with incident power of 250 mW. When operating in CW mode, the maximum power is limited by fixed attenuation to 5.5 mW. A heterodyne detection scheme is employed in the bridge, with dual outputs in phase-quadrature; phase settings are continuously variable by manual adjustment. Further details of the bridge design, including: principles of operation, block diagram of the microwave assembly, lists of the electronic components, and performance specifications are included in Appendix I. Field modulation at frequencies up to 150 kHz, and maximum amplitude of 15 G can be applied; two computer-interfaced lock-in amplifiers (EG&G PAR models 5207 and 5208) are used to detect the modulated signal.

The cavity assembly is illustrated on the following insert pages. The first shows a schematic of the assembly, which features a (slotted) TE<sub>011</sub> right circular cylindrical side-wall coupled to the waveguide transmission line through an iris. As indicated in the illustrations, the waveguide is part of an assembly that remains “fixed” in the magnet, while the cavity is part of an assembly that is removable, thus facilitating sample changing. Both parts are designed to be accommodated within an Oxford Instruments CF935G dynamic continuous flow cryostat (operating at temperatures as low as 3.8 K). The cavity is spring mounted on the probe to insure an appropriate fit of the coupling components. Coupling is adjusted varying the by orientation of the cylinder axis of the microwave cavity. This movement is accomplished by rotating the entire removable assembly by means of the arm at the top of the probe; the alignment of this axis can be varied through  $\pm\pi/8$  from its nominal orientation, perpendicular to the external field. The resonant frequency for the TE<sub>011</sub> model of the cavity is made to match the 94.9 GHz oscillator frequency by remote movement (knurled knob control) of one of the cavity endwalls. The



### Schematic of the microwave cavity assembly

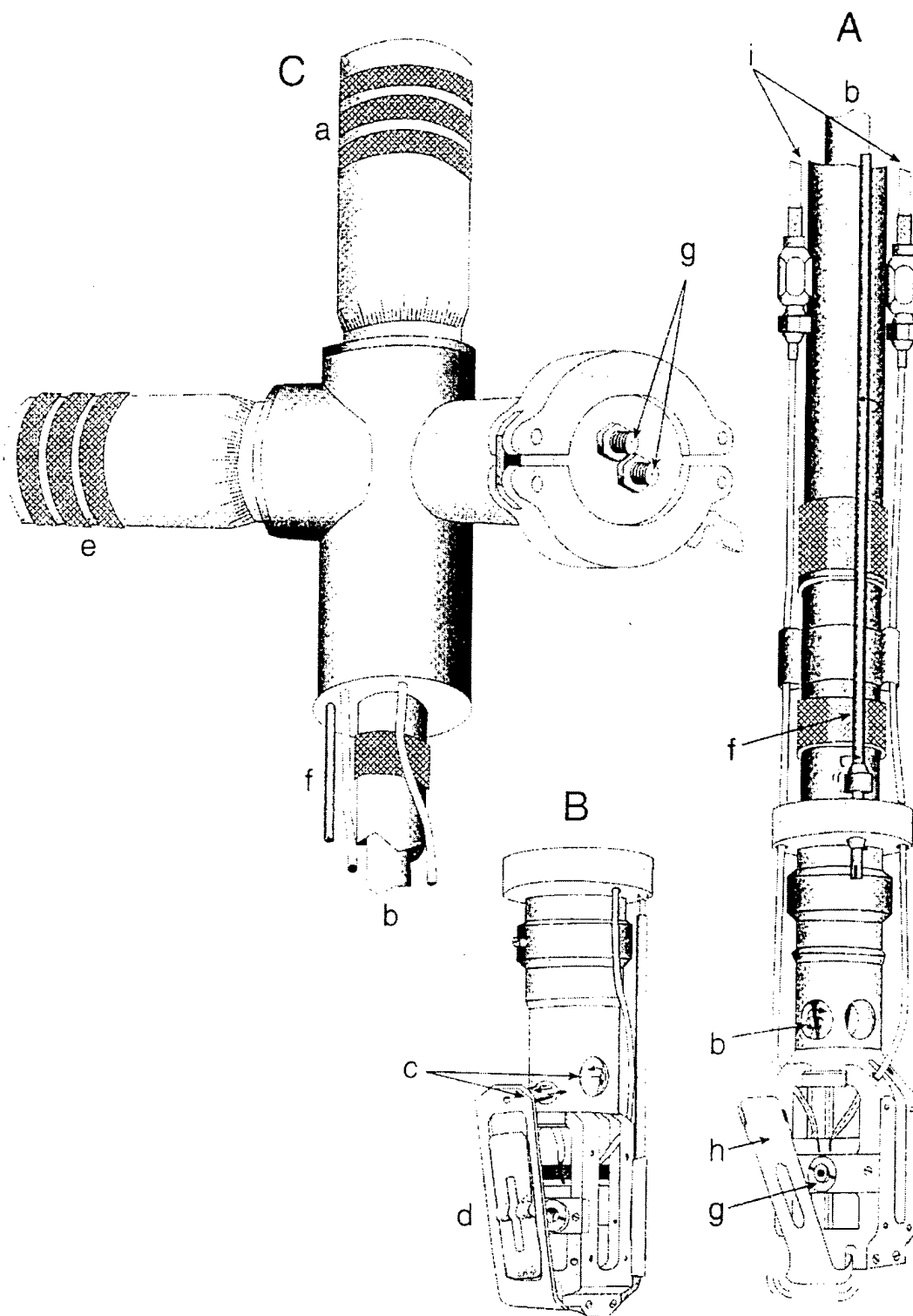
The microwaves are coupled from the W-band transmission line (C) through the iris coupling hole into the right circular cylindrical resonator, which is slotted to enable penetration of the of the oscillating rf fields (depicted, A) or audio fields for field modulation (not depicted). The sample is introduced through holes centered in the plungers (B), whose lateral position is adjust to match the cavity resonance and fixed microwave frequency.



**Views of the exterior, fixed assembly portion of the EPR probe**

(A) Bottom end showing the waveguide transition (f) and bend to reach the microwave cavity (b). A temperature sensing element is mounted at (d).

(B) Top end showing connection of waveguide to the microwave bridge (a), clearance for electrical connections (c) and arm (e) for adjusting the orientation of the cavity and the microwave coupling.



#### Views of interior, removable portion of the EPR probe

(A, B) Views showing the cavity assembly (B) and its extension (A) toward the top of the probe. The internal rod (b), with a cone at its bottom, pushes against lever (d) thus adjusting the position of the cavity plunger. The clamped (h) sample holder (g) is rotated by a shaft (f) and gear assembly.

(C) Views of the top of the probe showing adjustment knobs for control of cavity tuning (a) and sample rotation (e) with respective control rods (b and f). Inputs and cables (i) for rf and audio fields are shown.

position of the other wall is varied by the introduction of spacers to keep the coupling hole approximately in the center of the cavity. This adaptation allows for the introduction of a rotating-shaft and gear assembly for sample rotation about the cylinder axis of the cavity, as indicated in the figures. Cables and wiring for magnetic field modulation (and ultimately for ENDOR (electron nuclear double resonance), as depicted) and for temperature sensing are also illustrated. The basic features this system, in particular the remote adjustable tuning and coupling schemes were developed over years of collaboration between Lebedev and Krymov.<sup>1</sup>

The spectrometer is operated with software that was written under the LabView programming package at Montana State University. This software systems provides for control: of the magnetic field stationary setting, or field sweep between specified values at a specified rate; the magnetic field modulation frequency and amplitude, and the settings (phase, gain, harmonic, offset, time-constant) of lock-in amplifiers, when the system is operating in CW mode. In pulsed mode the master clock, pulse forming units (Stanford Research Systems, DG535), boxcar integrator (SRS 250/280), and D/A conversion system (SRS 245) are software controlled. The software system provides a convenient user interface for adjustment of the various control and acquisition settings, and for display and manipulation of the output EPR spectra. This computer display is illustrated on the accompanying insert pages. The LabView “code” is reproduced in Appendix II.

### **3. Experimental and Results**

#### **3.1. Neutron-irradiated sapphire single-crystal fiber**

Interest in this system - as part of a broader study of electron-transfer chemistry in optical materials - is sparked by the photobleaching and thermoresistant spectral hole-burning phenomena that it exhibits [4,5]. These phenomena have attracted interest to the material as a candidate for application in optical data-storage technologies based on spectral hole-burning [6].

### Dialog Parameters

Title	CWEPR
Sample (don't Use VI::<>  or return)	
b dpa	
Temperature	
degrees	1294.0
Kelvin	10
Sample Rotation	
Degrees	0.00
Experiment Type	
Pulsed	
CWEPR	
Operator	DAS
Boxcar Parameters	
Number Averaged	10
Gate Width (nsec.)	10
Sensitivity (mV)	10
Tuning Position	
Coupling Position	0
Pulse Widths (nsec.)	
Delay1 (nsec.)	
Delay2 (nsec.)	
Rep Rate (Hz)	

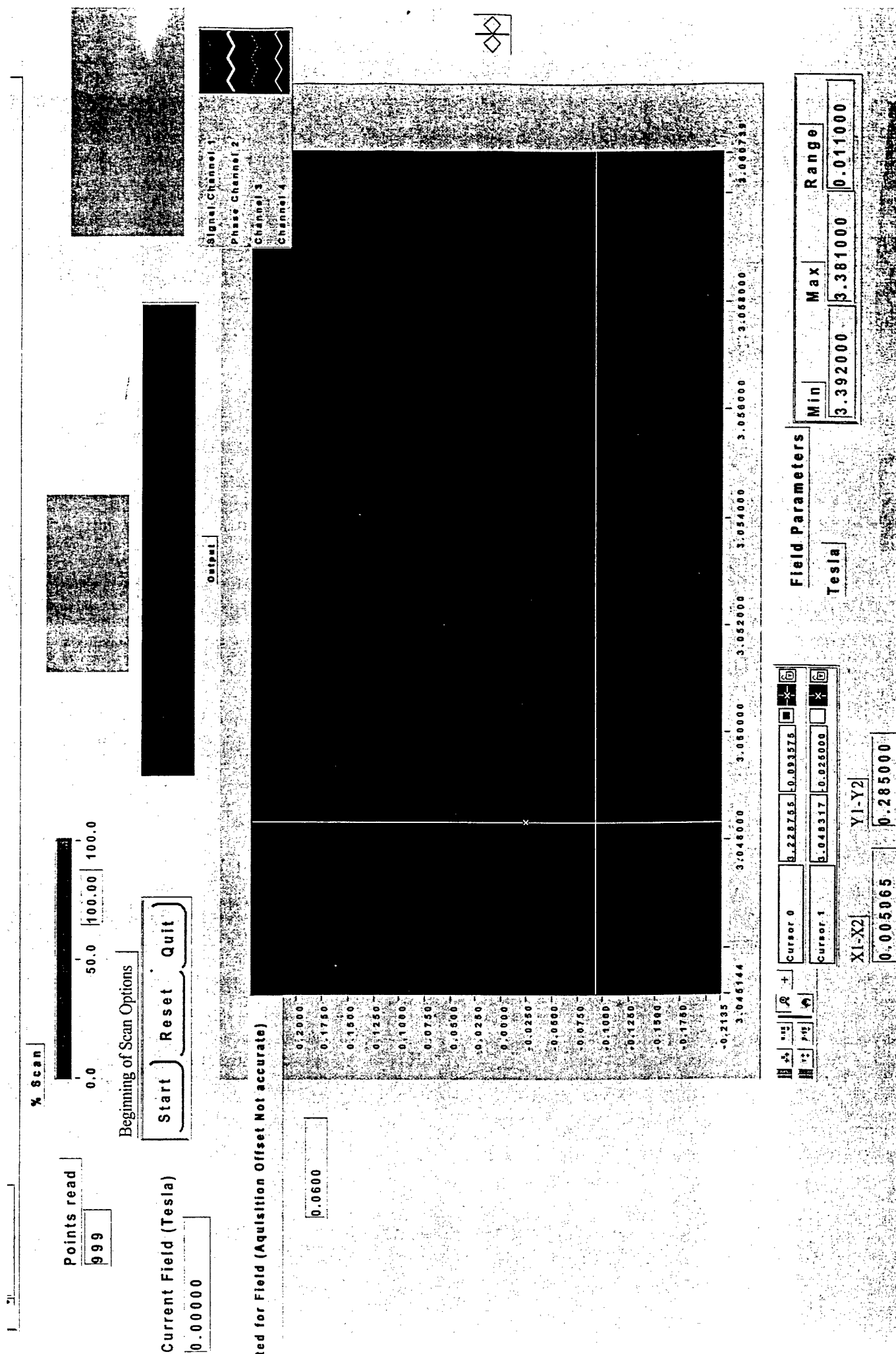
### Echo Timing Parameters

Tuning Position	
Coupling Position	0
Pulse Widths (nsec.)	
Delay1 (nsec.)	
Delay2 (nsec.)	
Rep Rate (Hz)	

### Control Parameters

Set Acquisition Frequency	20.00
Lock-in	
Multiplier	3
Resolvable Feature Size(G)	0.03000
Center Field(Tesla)	3.750
Range (Tesla)	3.750
Frequency (GHz)	194.90000
Attenuator 1 (mA)	0.000
Attenuator II (mA)	58.00000
Field Sweep Parameters	
Phase (deg.)	1F or 2F
Time Constant	1F
Frequency (KHz)	75.00
Look-up Phase	OFF
G/min.	0.0100
T/sec.	0.0000
G/sec.	1.6667
AutoOffset	
Sensitivity	3.00
Amplitude (Volts)	3.00
Slope	FF
Number of Data points	4000

Labview Routine for EPR Control and Data Acquisition: Experiment Set-Up Screen



## Labview Routine for EPR Control and Data Acquisition: Experiment In-Progress Screen

Neutron-irradiation of ostensibly white sapphire, followed by thermal annealing, generates a series of new optical absorption bands [7]. Laser irradiation in these bands can produce a frequency-selective bleaching of the irradiated band, accompanied by an intensity increase in other bands [8]. This process has been modeled as photo-induced electron transfer among mono- and di-anion vacancies with one or two electrons trapped at each vacancy - i.e., among F and F<sub>2</sub> centers having various “oxidation-states” (0, +1, +2) and spin multiplicities (S=0, 1/2, 1, 3/2, 2), as tabulated below [7,8]. Compelling structural evidence for this model, however, is lacking. Since EPR spectroscopy is well-established as a choice method for identifying, characterizing, and quantifying paramagnetic color centers - and thus for providing crucial information required for understanding the performance, and for optimizing the preparation of such materials. Motivated both by the photo-chemical properties of neutron-irradiated, thermally annealed sapphire, and its potential applications, we launched an EPR investigation aimed at determining the nature of the paramagnetic centers in this material.

**Model for Induced Centers:**

Oxygen Vacancies	Trapped Electrons	S	$\lambda_{\max}$ (nm)
F <sup>+</sup>	1	1/2	205
F	1	0	258
F <sub>2</sub> <sup>++</sup>	2	1	450
F <sub>2</sub> <sup>+</sup>	2	3/2	355
F <sub>2</sub>	2	0	300

Samples were obtained from Professor Aleksander Rebane at Montana State University. Crystals were prepared by Professor William Yen (University of Georgia) by a laser-heated pedestal growth method, with starting materials of 99.999% purity [12]. This method enjoys a smallness-of-scale that facilitates rapid preparation of a wide variety of crystal samples. Crystals fabricated by this method, however, are generally small: our sapphire samples have the shape of a right circular cylinder, 0.5 mm in diameter and 10 mm in length. *Note that these fiber-like samples have a volume that is a factor of 10<sup>2</sup> smaller than sample volumes typically enjoyed in*

*X-band experiments.* Crystals were neutron-irradiated with a dose of  $\sim 10^{19}/\text{cm}^2$  and annealed at  $\sim 600$  K by Professor Ilmo Sildos (University of Tartu, Estonia) [4,5].

### 3.1.1. *Spectroscopy*

Initial results of the high-frequency EPR investigation on this material have been published in Ref. 27. Three predominant sets of EPR signals (evident in Figure 1), were readily identified as  $\text{Cr}^{3+}$  ( $S=3/2$ ) and a pair of crystallographically equivalent  $\text{Fe}^{3+}$  ( $S=5/2$ ) impurity ions. High-frequency EPR instrumentation played a key role in facilitating the identification of the high spin multiplicity  $\text{Cr}^{3+}$  and  $\text{Fe}^{3+}$  centers. Numerous weaker EPR signals are also apparent in spectra displayed with expanded vertical scales (see Figure 2). These spectra presumably belong to the neutron induced color centers, and have subsequently been more carefully investigated (as exemplified in Figure 3); the spectra, as detailed below, are complex; a full analysis is underway now that the major signals have been identified.

In Ref. 27, the following EPR parameter values were published:

$\text{Cr}^{3+}$   $g_{\parallel} = 1.9812 \pm 0.0001$ ,  $|D| = 5.738 \pm 0.003$  GHz,  $g_{\perp} = 1.9814 \pm 0.0001$ ;

$\text{Fe}^{3+}$   $g = 2.0034 \pm 0.0001$  and  $|D| = 5.033 \pm 0.002$  GHz, and  $|a - F| = 0.986 \pm 0.006$  GHz.

The estimated errors are evaluated by propagation of an estimated error in  $B_{\text{res}}$  of 1.7 G, which derives from errors in observation and calibration [13].

Comparison of the amplitudes of the  $\text{Fe}^{3+}$  or  $\text{Cr}^{3+}$  EPR signals (adjusted for their different values of  $S$  and  $S_{\pm}$ ) with those measured under equivalent conditions for an EPR dosimetry standard ( $\text{E}'$  centers in “wet” suprasil silica exposed to a dose of 3 Mrad  $^{60}\text{Co}$   $\gamma$ -irradiation)<sup>17</sup>, gives an experimental estimate of  $10^{16}$  ions/ $\text{cm}^3$  for both  $\text{Fe}^{3+}$  and  $\text{Cr}^{3+}$ . This concentration corresponds to a substitution ratio of  $10^{-6}$ , a value similar to the purity of starting material.

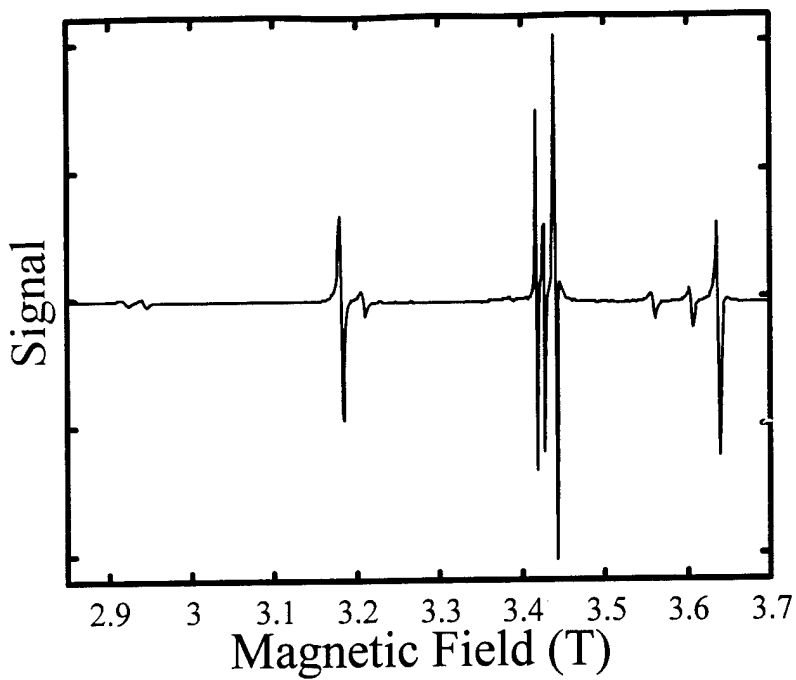


**Figure 1.** 94.9 GHz EPR spectrum of a neutron-irradiated sapphire single crystal recorded at room temperature and with the external field making an angle,  $\Theta=0.18\pi$ , with respect to the crystal c axis. The microwave power was 3  $\mu$ W. The field was swept at 0.33 T/min and modulated at 75 kHz with an amplitude of 10 G. Lock-in detection was employed with a time-constant of 100 msec.

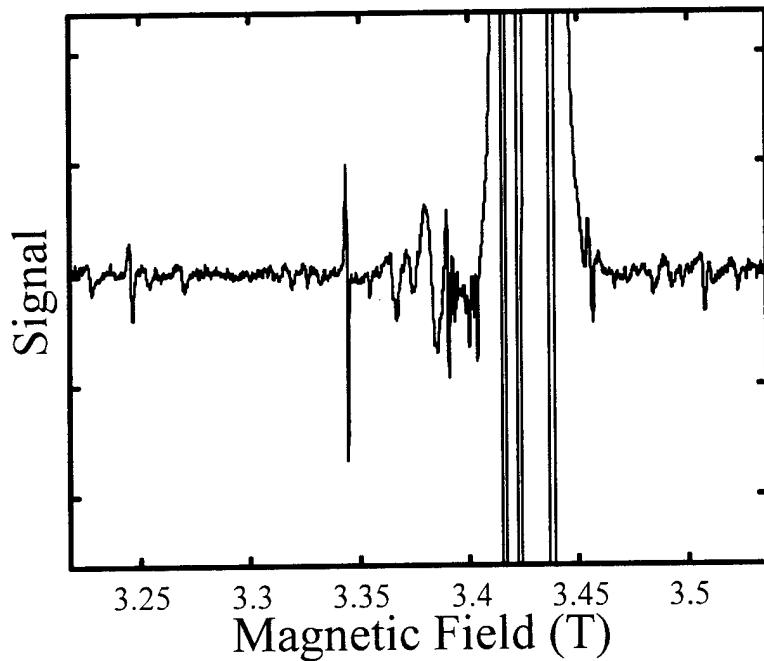


**Figure 2.** 94.9 GHz EPR spectrum of a neutron-irradiated sapphire single crystal recorded at room temperature and with the external field at  $\Theta=0.18\pi$ . The microwave power was 5 nW. The field was swept at 100 G/min and modulated at 75 kHz with an amplitude of 1.5 G. Lock-in detection was employed with a time-constant of 100 msec.

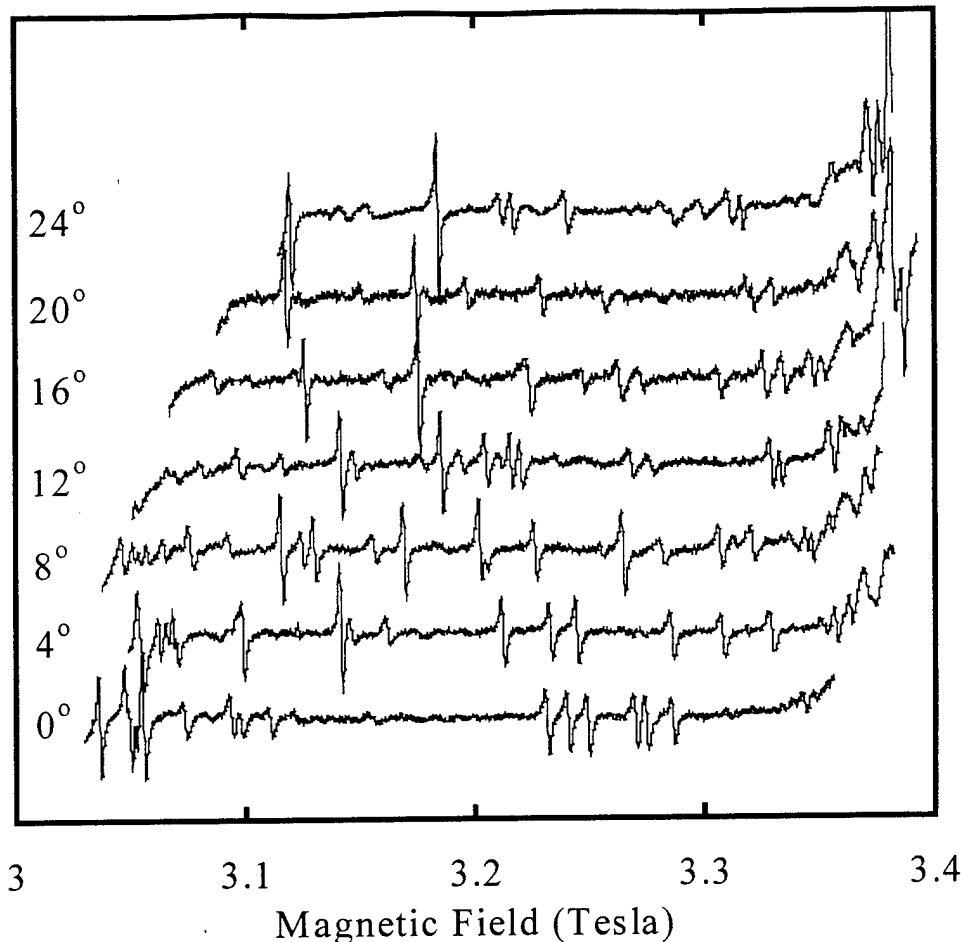


**Figure 3.** Detail of 94.9 GHz EPR spectra of a neutron-irradiated sapphire single crystal recorded at room temperature and with the external field making the designated angles (degrees) with respect to the crystal c axis. The microwave power was 3 nW. The field was swept at 100G/min and modulated at 100 kHz with an amplitude of 1 G. Lock-in detection was employed with a time-constant of 30 msec.

For  $\text{Cr}^{3+}$ , Zverev and Prokhorov previously reported  $g_{||} = 1.982 \pm 0.002$ ,  $g_{\perp} = 1.979 \pm 0.009$ , and

$D = -5.73 \pm 0.03$  GHz [14]; Kornienko and Prokhorov [15] reported for  $\text{Fe}^{3+}$  the parameter values –

$g$  (isotropic) =  $2.0030 \pm 0.0006$ ,  $D = +5.034 \pm 0.001$  GHz, and  $|a - F| = 0.990 \pm 0.001$  GHz. A remark is in order concerning the  $\text{Cr}^{3+}$  parameters values. Manenkov and Prokhorov [22] originally reported the  $g$ -values,  $g_{||} = 1.984$ ,  $g_{\perp} = 1.9867$  based on work at 8.96 and 11.97 GHz. The values cited above were obtained later in “more complete” work at 37.86 GHz [14]. In later work by several other groups [23-25], values closer to the original ones [22] appear. The suggestion was made in Ref. 27, that the conventional spin-Hamiltonian used to describe the  $\text{Cr}^{3+}$  might not be entirely adequate. In particular, “high-spin Zeeman” terms linear in field and

cubic in spin angular momentum – which are admissible in the most general spin-Hamiltonian for an S=3/2 system, but are conventionally ignored – had been suspected as the origin of this discrepancy. A detailed analysis of the Cr<sup>3+</sup> spectra was subsequently undertaken by us to address this issue; elements of this work are given in Appendix III. The major conclusion is that the high-field Zeeman terms are negligible, and the discrepancy simply emanates from some author’s repeated quotation of Prokhorov’s original, less accurate results.

The presence of transition metal ions in this material, at concentrations that may be similar to that of the color centers, raises additional, fundamental issues. In their pioneering study of the optical absorption spectra of neutron damaged sapphire [7], Evans and Stapelbroek found transition metal ion concentrations to be less than ~5 ppm. They provided detailed arguments that the absorption spectra were not assignable to substitutional metal ion impurities, but neither they nor subsequent investigators fully considered the effect that their presence might have on the production or aggregation of lattice defect centers. Redox active ions should be expected to impact the solid-state, electron-transfer chemistry that occurs in the preparation (irradiation and thermal annealing) and the utilization (optical photo-bleaching, hole-burning) of this material. For example, a recent study of the effects of neutron-radiation on metal ion doped sapphires clearly shows that the presence of the ions alters the distribution among radiation-induced products; in particular, new products involving F centers associated with metal ions are reported [19]. Dose-response effects are modulated by the radiation-induced valence changes in Cr and Fe centers - an effect also reported in  $\gamma$ -irradiation studies [20]. Such effects, while not well-understood systematically, have nevertheless been exploited empirically to impart radiation hardness to optical materials [21]. For photo-ionization and electron-transfer processes, the potential effects of redox active are even more obvious. Studies of the optical properties of neutron-irradiated sapphire must include an assessment of transition metal content, and must be designed to control for, and to exploit, their effects.

### 3.1.2. Line shapes of the Chromium(III) centers.

An analysis of the line shapes of the  $\text{Cr}^{3+}$  EPR signals discussed above, demonstrated (see Figure 4) that the line shapes adhere very closely to (derivative) Lorentzian form (width of  $\sim 30$  MHz) and deviate noticeably from Gaussian shapes. This result seemed surprising. Inasmuch as the measured  $\text{Cr}^{3+}$  spin concentration in the sample is  $10^{16}/\text{cm}^3$ , the interaction with neighboring aluminum nuclear moments would be expected to be the dominant line broadening effect. This interaction, however, would certainly lead to an inhomogeneous Gaussian broadening of the lines.  $\text{Cr}^{3+}$ - $\text{Cr}^{3+}$  dipolar interactions could lead to spin-exchange line broadening effects, but concentrations of  $10^{20}/\text{cm}^3$ , would be required to produce the observed line widths.

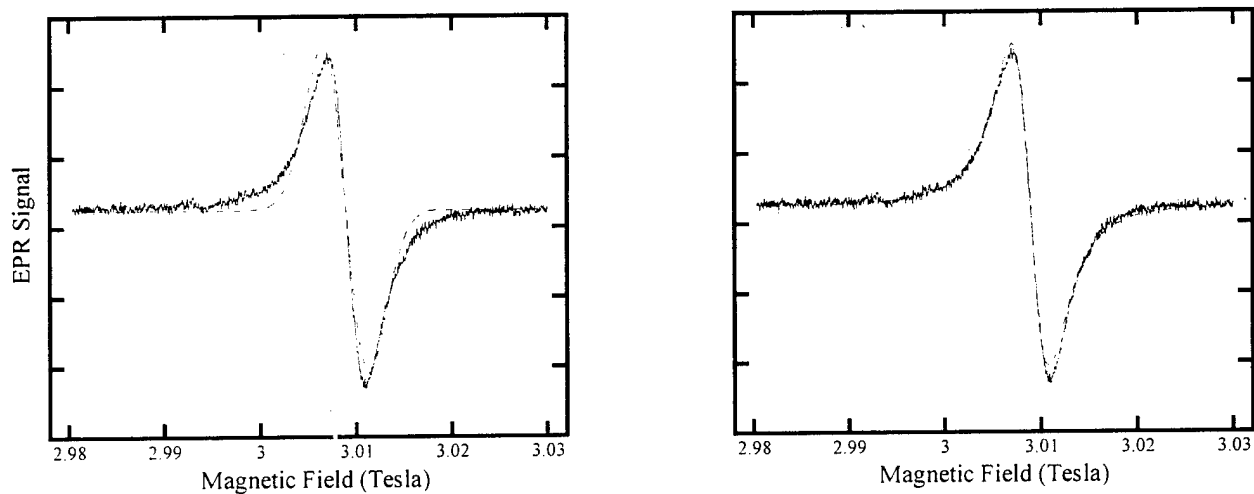


**Figure 4.** Line shape analysis of  $\text{Cr}^{3+}$  EPR spectra. The same experimental spectrum ( $M_s = \pm 1/2$  transition with the field aligned along the crystal c axis.) is depicted in both the right and left panels. The least squares best fit derivative Gaussian (left panel) and Lorentzian (right panel) are superimposed (dashed lines) on the spectra. The Lorentzian shape gives an excellent representation of the data, with a line width of 19 G.

These results can be explained by assuming that the distribution of the impurity centers is not uniform within the lattice; the centers are segregated from the bulk material. The global concentration (measured by spin counting) could thus remain small, while the local concentration (reflected in the line shape) could be very large, as dictated by the degree of segregation. To test this idea, surface specific elemental analyses – SIMS (secondary ion mass spectrometry) and XPS (x-ray photoelectron spectroscopy) – were carried out at the ICAL facility

of Montana State University. The results of these and the EPR measurements are given in the table below.

Analysis Method	EPR intensity	EPR line width	SIMS	XPS
Range of Sample Probed	Global	Near-neighbor Spins	Depth of ~10 Å	Depth of ~500 Å
Cr Concentration	$10^{16}/\text{cm}^3$	$6 \times 10^{20}/\text{cm}^3$	$4 \times 10^{21}$	$1 \times 10^{20}$

The SIMS and XPS support the idea of that the chromium ions are substantially segregated and further reveal that they are congregated near the very surface of the fiber. It remains to be determined whether this clustering occurs during the laser pedestal crystallization process, or during the subsequent irradiation and annealing of the particular sample studied. It has previously been noted, however, that the optical  $T_2$ 's of materials grown by laser pedestal methods tend to be markedly smaller than those of materials made by slower methods of growth methods. It is therefore tempting to suggest that the segregation occurs during the crystallization process: this partitioning would explain both the anomalous EPR and optical homogeneous line widths.

### 3.2. $\gamma$ -Irradiated Vitreous Fused Silica

The paramagnetic defects, generically known as E'-centers, induced by  $\gamma$ -irradiation of fused silica glassy samples have been studied in detail for many years [29]. A study of a sample of such material was undertaken with one major goal in mind: *to establish the performance of the instrument built in the time-domain, spin-echo mode of operation*. Further study of this material was warranted by the opportunity to utilize it in a program of high-frequency EPR dosimetry, with the goal of assaying novel, biological radiation shielding material, as reported in the NASA innovation magazine [30]. The CW EPR radiation dosimetry studies led to an appreciation of prevalence of “rapid passage” effects in high-frequency EPR spectroscopy, and *the emergence of a new line of investigation aimed at elucidating and harnessing these effects*.

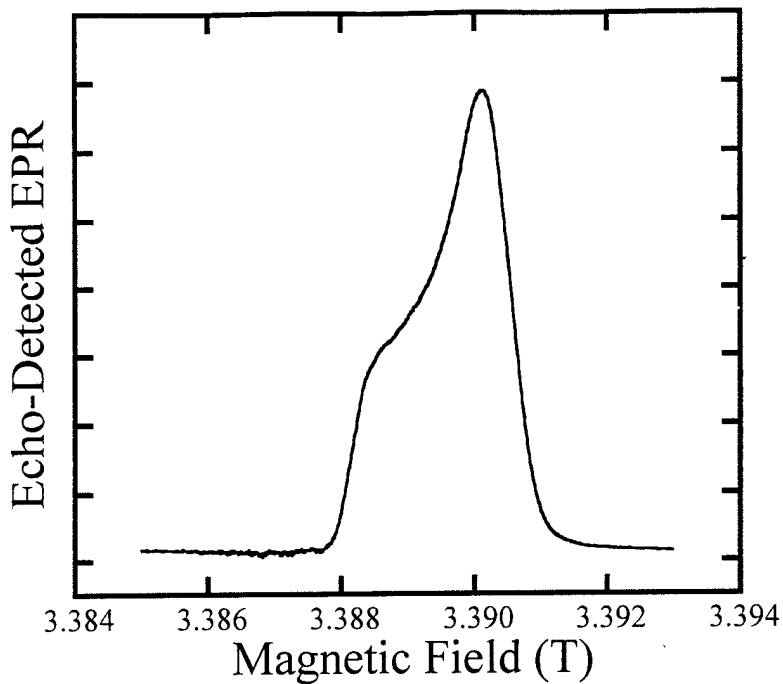


Figure 5. Echo-detected EPR spectrum of  $^{60}\text{Co}$   $\gamma$ -irradiated suprasil fused silica glass. Experimental details are given in the text. Absent field-modulation and lock-in detection the integral form of the spectrum is registered.

### 3.2.1. Benchmarking of spin echo capabilities.

$\text{E}'$ -centers in  $\gamma$ -irradiated fused silica glass are a standard test sample for evaluating pulsed EPR instrumentation. An echo-detected EPR spectrum of such a sample is shown in Figure 5. The sample is a 0.35 mm diameter rod of suprasil quartz subjected to 100 Mrad of  $^{60}\text{Co}$   $\gamma$ -irradiation. The echo-detected method employed involves application of two, 94.9 GHz microwave pulses with peak power  $\sim$ 230 mW, duration 36 nsec separated by a delay of 200 nsec and detection on the resulting echo at a subsequent delay of  $\sim$  200 nsec with a boxcar integrator whose gate width was  $\sim$ 50 nsec. The echo cycle was repeated at a rate of 1 kHz. The sample was at room temperature in these experiments. For echo-detected EPR spectroscopy, the sequence is

continually repeated as the magnetic field is scanned. An exponential average of the prior 300 echoes was acquired at each field step to compose the spectrum. Single-shot signal-top-noise ratios were  $10^2$  under these conditions. This result, is similar to performance standards at lower microwave frequencies (e.g., X-band ( $\sim 10$  GHz) , provided the sample is increased to its optimum size at the lower frequency ( $10^1$  greater diameter and  $10^1$  greater length). This result thus indicates a improvement in sensitivity of as much as  $10^3$  at 95 GHz, *for volume limited samples*.

### 3.2.2 Saturation and Passage effects in high-frequency EPR

CW EPR spectra of the same fused silica sample are shown in Figure 6. The two phase-quadrature microwave signal channels are displayed (absorption signal, solid line; negative dispersion signal dashed line) together with the vector magnitude response (dotted line). Under

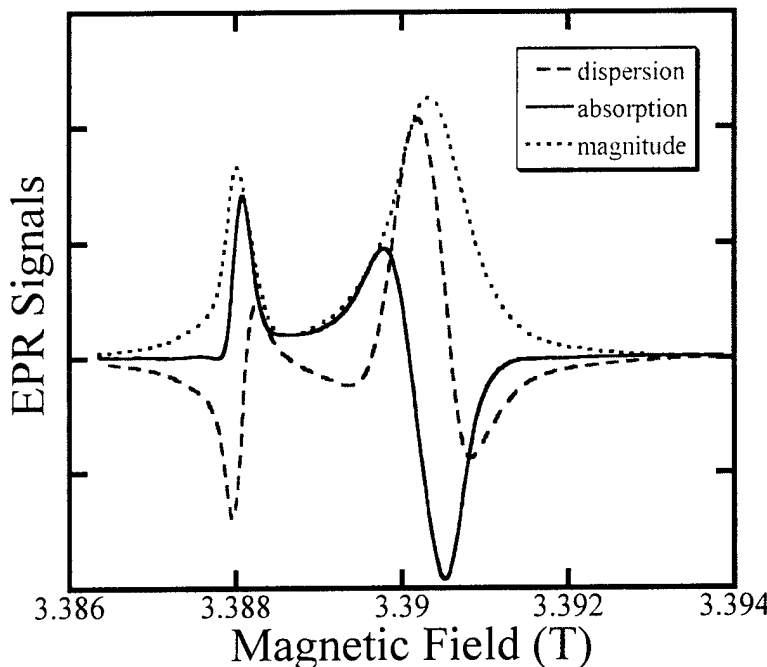


**Figure 6.** Absorption, Dispersion, and Magnitude EPR spectra of E' center in irradiated quartz. Microwave frequency 94.9 GHz, power 55 nW (-50.6 dB attenuator setting), scan-rate 200 G/min, time constant 0.1 sec, modulation frequency 75 kHz, modulation amplitude 2.5 G.

non-saturating conditions, the absorption and dispersion signals comprise a simple Hilbert transform pair – as is neatly illustrated in Figure 6. If the microwave power is increased sufficiently, this simple relationship is broken. The absorption signal amplitude reaches a stationary level (saturation); moreover an apparent partial integration of the derivative (field-modulated and lock-in detected) CW EPR signals can occur, as vividly illustrated in Figure 7

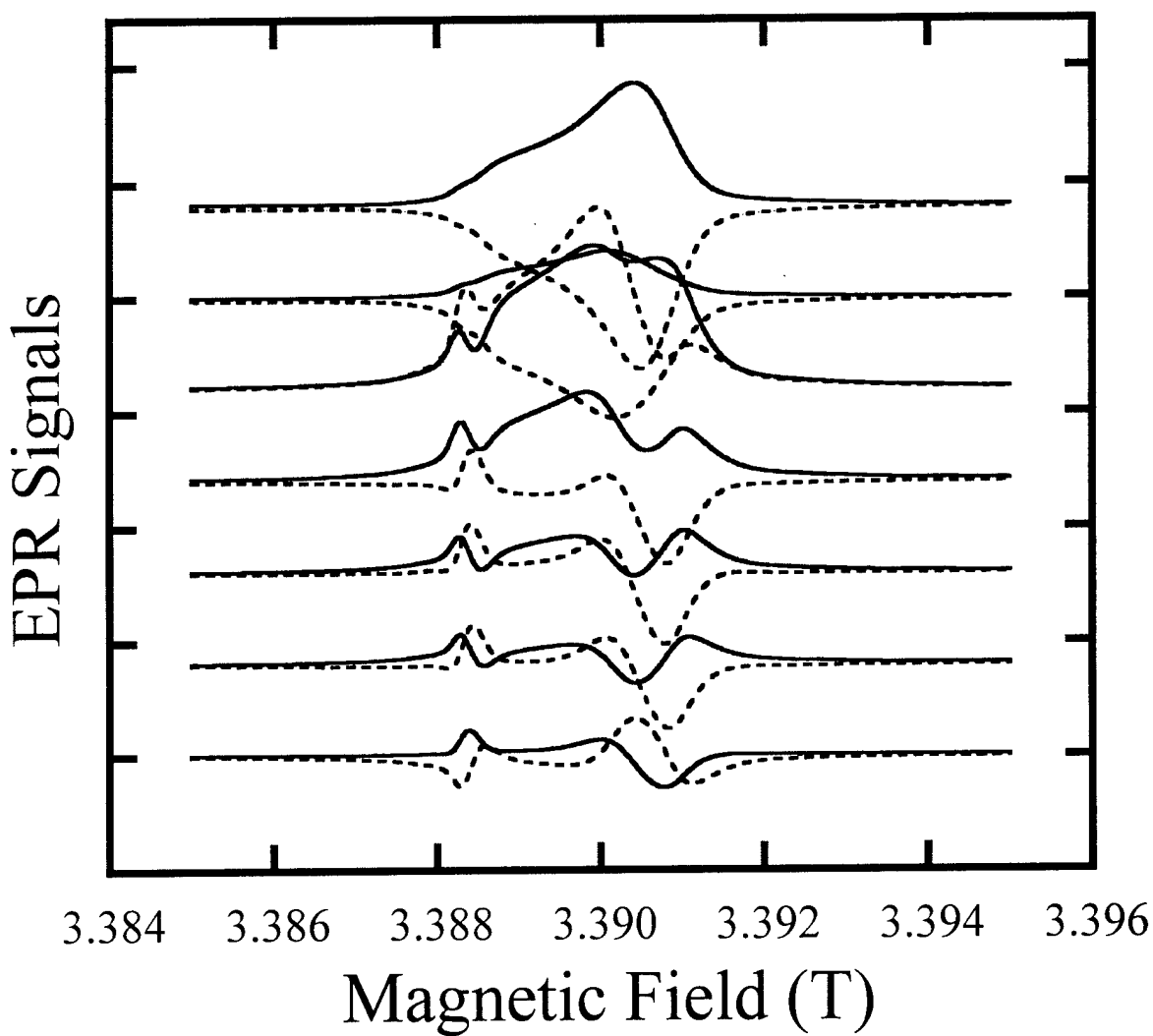


**Figure 7.** Power dependence of phase quadrature EPR signals of the irradiated quartz sample (Figs. 5 and 6). The detector phase is adjusted such that at non-saturating powers (bottom spectrum) the solid line is the absorption and the dashed line is the dispersion spectrum (Fig. 6). Acquisition parameters are the same as in Fig. 6, apart from microwave power, which varies top-to-bottom as: -11.7, -28.9, -39.0, -42.8, -45.9, -48.5, and -50.6 dB from full power (5 mW).

[31]. (Only the passage effects are illustrated; the signals are “peak normalized” thus relative amplitude information is not exhibited). An intriguing aspect of high-frequency EPR spectroscopy is the *apparent* ease of reaching saturation in the study of dilute paramagnetic centers in solids. To operate in the linear, non-saturating it has been necessary to operate the instrument built MSU at incident microwave powers of  $\sim$ nW, far from its 5 mW peak CW power. Farrar et al. [32] in a 140 GHz study of a tyrosyl radical in a photosynthetic reaction centers, found that the dispersion signal, in-phase with the field modulation, obtained under rapid passage conditions, enabled an crucial enhancement of signal-to-noise ratio over the conventional absorption signal, and also provided better resolution (less power-broadening) of hyperfine structure. Lebedev and co-workers [33] have also published 140 GHz EPR spectra obtained as conventional absorption signals, as well as both dispersion signals in phase and in phase-quadrature with the field modulation, and by analysis of these signals have obtained estimates of characteristic relaxation times.

Studies of this behavior have a number of antecedents in solid-state EPR at conventional frequencies (not to mention the entire field of saturation-transfer EPR in fluids [34]). In pioneering work, Hyde used rapid passage methods discern the presence distinct color centers with overlapping spectra in irradiated LiF [35]. Very recently Godbole and Sastry [36] revisited this idea, and demonstrated that certain spectral displays can be used to “edit” complex EPR spectra involving multiple paramagnetic centers with distinct relaxation properties: specifically, in a crystal of  $\text{CaF}_2$  co-doped with  $\text{U}^{3+}$  and  $\text{Gd}^{3+}$  they established conditions under which an overlapping  $\text{U}^{3+}$  spectrum was edited from the spectral display, leaving a “clear  $\text{Gd}^{3+}$  spectrum”. Mailer and Taylor [37] found a signal enhancement of at least 500 in ferricytochrome c by detecting rapid passage EPR signals in the dispersion mode. Ammerlaan and van der Wiel[38] measured longitudinal relaxation times of vacancies in silicon by analysis of the temperature dependence of dispersion EPR lineshapes obtained under passage conditions. Such examples make it clear that there are significant advantages to be gained in signal strength, spectral

selectivity, sensitization to dynamics that can be accessed by departing from the conventional practice. At the same time it must be admitted that, in contrast to the study of dynamics in fluids by saturation-transfer EPR, the application of these potential tools in the EPR of solids has been limited.

In part, this limitation is arguably related to instrumentation. Good signal-to-noise ratios in dispersion EPR are hampered by demodulation of source noise. This problem has been mitigated by the use of a bimodal resonator[39] and high-bandwidth, loop-gap resonators[40]. High-frequency resonators with quality factors of  $\sim 5000$  enjoy a similar bandwidth to low Q loop-gap resonators, and are thus likewise well-suited to dispersion detection. A second aspect can be linked to the complexity of the underlying theory. The Bloch equations augmented with sinusoidal modulation of the magnetic field are not, in general, analytically solvable. Portis [31] and Weger [32] derived certain expressions that are applicable in certain limiting cases (although not always experimentally useful ones). Their work (reprised also by Ammerlaan and van der Weil [38] elucidated much of the basic phenomena, in particular the nature of the absorption and dispersion signals obtained in phase and in phase quadrature with the field modulation. Cullis used a spin temperature approach in treating this problem [43]. He specifically considered issues of spectral line width, and power-broadening; moreover, on the basis of his analysis, he suggested new techniques for measuring relaxation properties. Solutions to this problem have been advanced – especially in the realms of coherent optics and saturation-transfer EPR - involving Fourier or Floquet [44] expansions, followed by evaluation of the expansion coefficients by continued fraction, recursive, and other mathematical approaches [34,45-46]. Grivet [47] carried out numerical solutions of these augmented Bloch equations by direct numerical integration of the equations using the fourth-order Runge-Kutta algorithm [48]. While computational solutions such as these do not directly advance our understanding, they do provide a valuable tool to simulate the behavior, and thereby providing conceptual support to the experimental work, and enabling its extension to situations not yet encountered experimentally.

Rapid passage techniques in solid-state EPR spectroscopy thus appears to have the potential to yield large enhancements of signal amplitudes, and to provide selectivity that can be used for spectral-editing. Moreover, passage phenomena are particularly prevalent in high-frequency EPR. Accordingly, a pilot program combining high-frequency EPR spectroscopy of test-bed materials and numerical integration of the underlying equations of motion was initiated to explore the feasibility of realizing this potential. The test-bed centers studied the E' center formed in irradiated vitreous silica, and the free radical BDPA ( $\alpha,\gamma$ -bis diphenylene- $\beta$ -phenylallyl) incorporated into a matrix of atactic polystyrene (PS) – the same sample employed by Farrar et al.[32]

In the numerical work, the simple approach of Grivet [47] was followed, namely numerical integration of the rotating-frame, coupled equations of motion:

$$\begin{aligned}\frac{dM_x}{dt} &= -\frac{M_x}{T_2} - \gamma M_y \Delta B(t) \\ \frac{dM_y}{dt} &= \gamma M_x \Delta B(t) - \frac{M_y}{T_2} - \gamma M_z B_1 \\ \frac{dM_z}{dt} &= \gamma M_y B_1 - \frac{M_z}{T_1} + \frac{M_0}{T_1} \\ \Delta B(t) &= B_{\text{res}} - (B_0 + B_m \cos(\omega_m t))\end{aligned}$$

in which  $B_0$  is the external field,  $B_1 = \gamma\omega_1$  is the microwave field ( $\gamma$ , the magnetogyric ratio for the electron spin),  $B_{\text{res}}$  is center of the resonance line at the operative microwave frequency,  $B_m$  is the modulation amplitude,  $\omega_m$  is the modulation angular frequency, and  $T_1$  and  $T_2$  are respectively the phenomenological longitudinal and transverse relaxation times. The equations of motion are integrated for a series of resonance offsets ( $B_0 - B_{\text{res}}$ ), and the inhomogeneous resonance by weighting these responses according to the intrinsic overall line shape. Through this integration we obtain the time-varying response of the absorption ( $M_y$ ) and dispersion ( $M_x$ ) signals at each sampled  $B_0$ . By transformation of these time-domain signals the signal

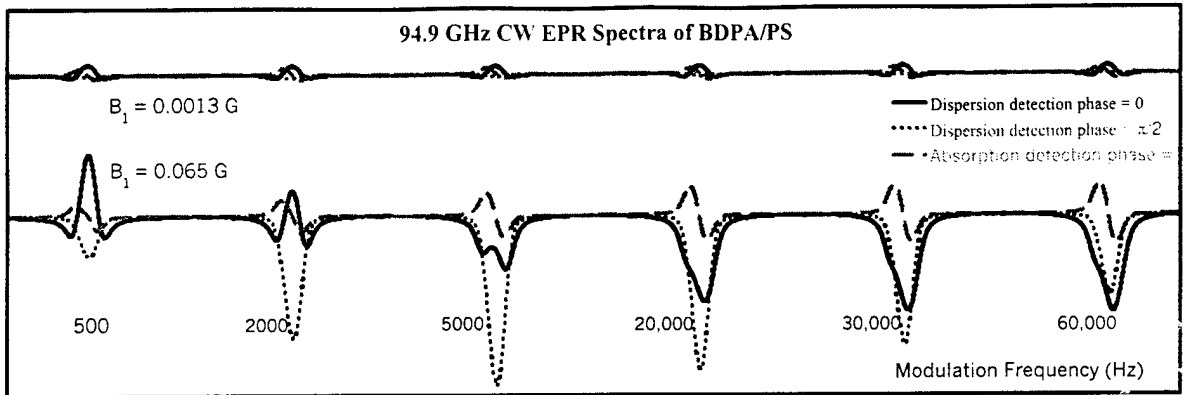


**Figure 8.** 94.5 GHz EPR spectra of BDPA in polystyrene (ambient temperature), as function of microwave power and field modulation frequency (amplitude 1G). Absorption and Dispersion signals are shown; the latter are registered in phase and in quadrature with the field modulation. Dispersion phase is inverted relative to figure 9.

components at harmonics of  $\omega_m$  are determined that are in phase and in phase-quadrature with the field modulation. This approach is not computationally efficient, but is very transparent in its mathematics and performance. Computations are carried out on SGI Octane or Origin 200/2000 workstations. (Further detail and C++ code are provided in Appendix IV).

The primary results of this work include:

- An experimental survey of power and modulation frequency effects on the BDPA/PS sample; exemplary results are shown in Figure 8. For clarity, only the 1<sup>st</sup> harmonic in-phase absorption and in-phase/phase-quadrature dispersion signals are shown. At the lower power illustrated, the spectral properties are independent of modulation frequency and correspond essentially to the linear, slow-passage regime. At the higher, saturating power level, the absorption signal remains at modest amplitude, but both dispersion signals grow dramatically. The phase-quadrature component has the shape of an undifferentiated absorption line, retains an “authentic” line width, and exhibits a amplitude maximum when  $\omega_m \approx 1/T_1$ . The in-phase signal has a dispersion derivative line shape at low  $\omega_m$  that evolves to a power-broadened undifferentiated absorption shape with increasing  $\omega_m$ . The crossover point (zero amplitude at the line center) occurs also when  $\omega_m$  is close to  $1/T_1$ .

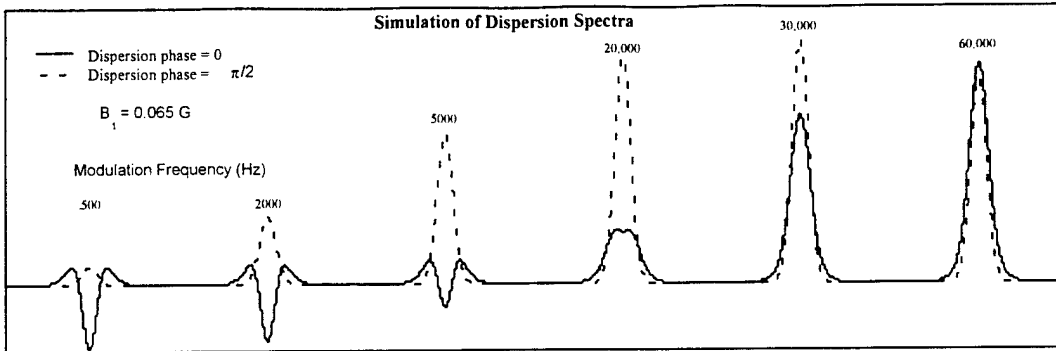
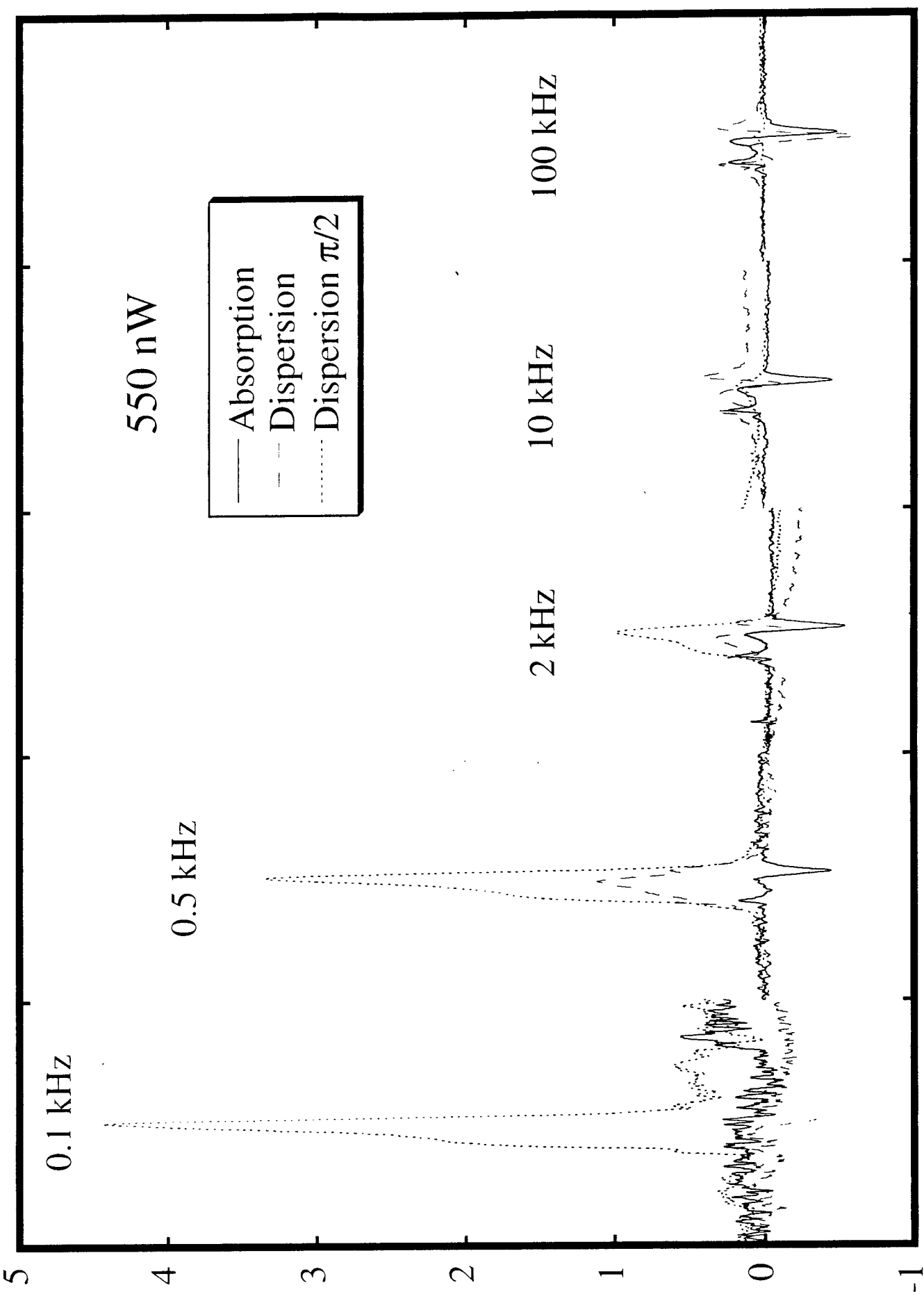


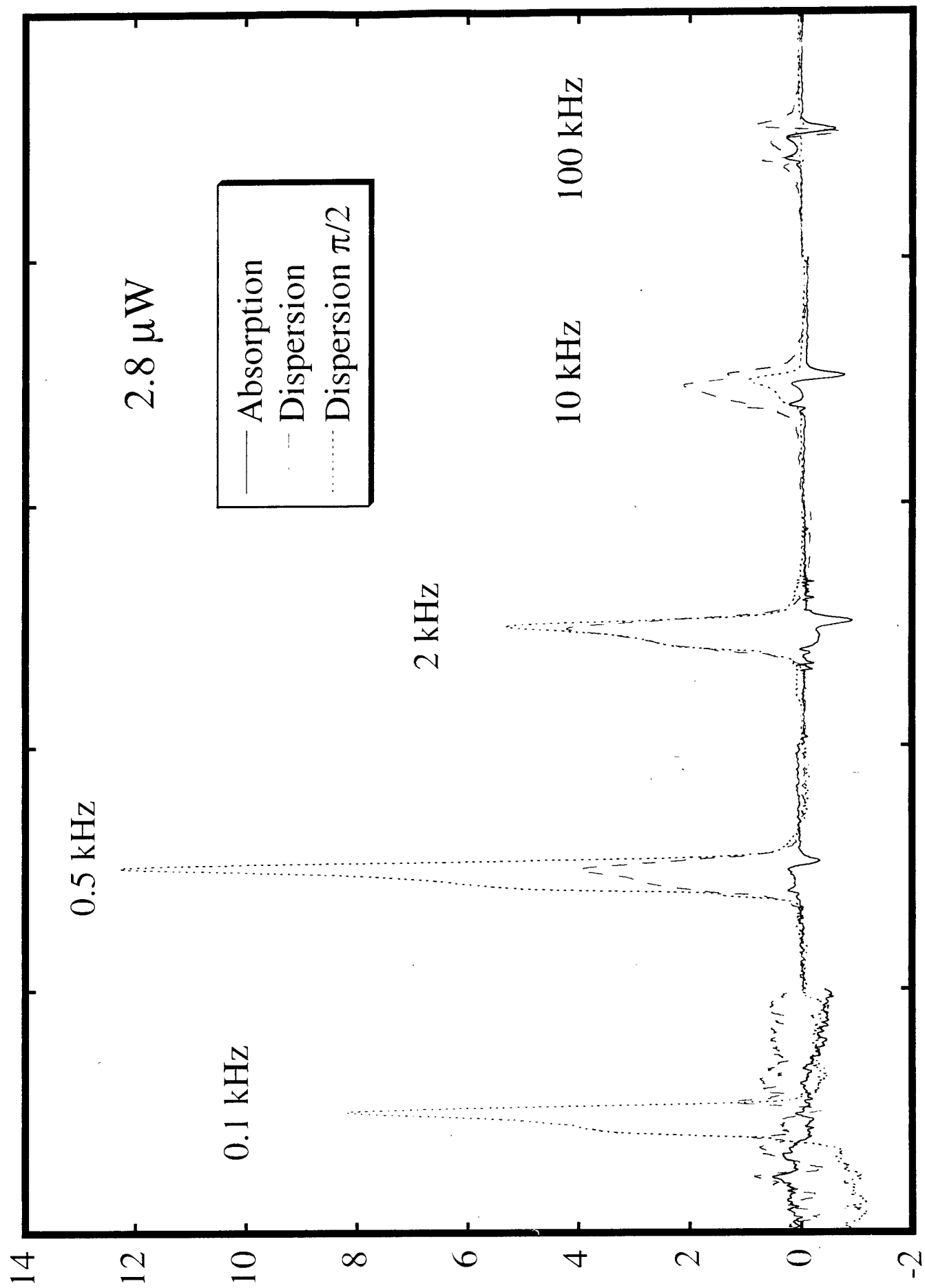
**Figure 9.** EPR signals simulated by numerical integration of the Bloch equations. Dispersion mode in phase (solid line) and in phase-quadrature (dashed line) with the magnetic field modulation. Simulations were done with the following parameters: Gaussian linewidth = 9 G,  $T_{11} = 18 \mu\text{s}$ ,  $T_2 = 1 \mu\text{s}$ ,  $B_1 = 0.065 \text{ G}$ ,  $B_m = 0.5 \text{ G}$ .

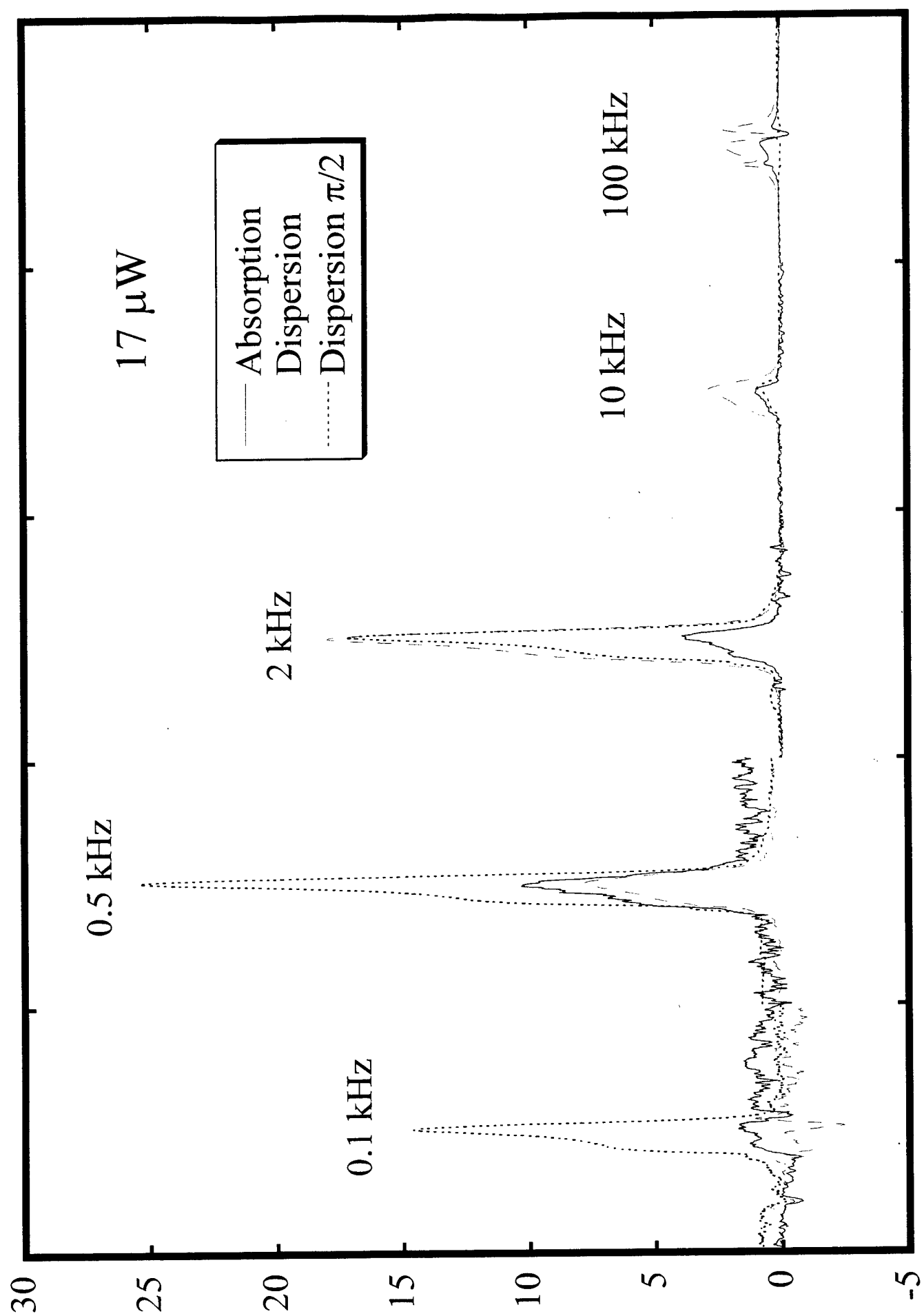
- Simulation of the behavior of these signals (Figure 9; only the 1<sup>st</sup> harmonic dispersion signals are shown) using the spectral and relaxation parameters reported by Farrar et al.[32]. These results immediately underscore the idea that dispersion rapid passage signals can provide substantially enhanced signal amplitudes. They suggest, moreover, that saturating powers can be reconciled with good spectral resolution, particularly in the case of the quadrature dispersion signal. This display also has a *line shape* that, as compared to the in-phase dispersion signal, is insensitive to  $\omega_m$  (and to relaxation properties). It therefore appears well-suited to the determination of spectroscopic parameters; knowledge of relaxation properties would be needed to quantitatively simulate the amplitude, but not the shape. This notion requires further testing in systems, such as the silica test sample, that exhibit more complicated line shapes. Moreover, it is important to test the robustness of the behaviors described above in particular with respect to variations in relaxation properties. This testing will be done through extensive numerical simulations.

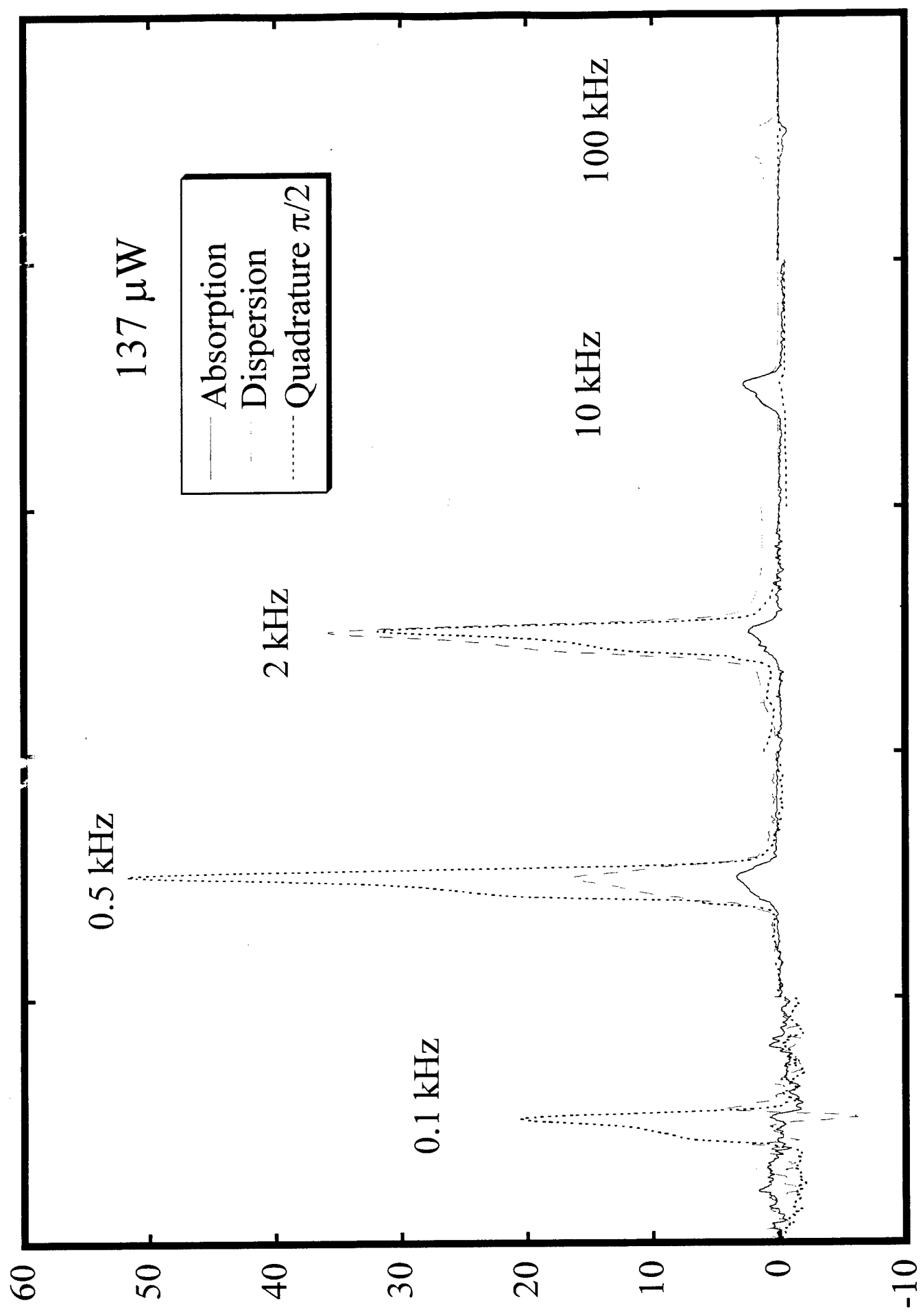
- An experimental study of the fused silica E' center as a function of power and modulation frequency. The sample used for these experiments was a tube of dimensions 0.87 mm OD, 0.7 mm ID, subjected to  $6 \times 10^5 \text{ rad}$   $^{60}\text{Co}$   $\gamma$ -irradiation. Selected results are shown in the figures on the next inserted pages. Each page exhibits a series of spectra obtained at the indicated modulation frequency and modulation amplitude of 3 G. Each spectrum entails a sweep of 200 G at a rate of 120 G/min and a time-constant of 0.3 sec. The vertical scales on each page indicate the relative amplitudes of the signals on all of the pages. Three spectral displays are

shown, namely the (low-power) absorption and dispersion signals, and the dispersion component detected  $\pi/2$  out of phase with the driving field modulation. The data on each page were obtained at a particular power level, as indicated. The fundamental result that emerges from this study is that the behavior observed is analogous to that of the BDPA/PS system provided only that the weighting of spin packets is adjusted to reflect the different inhomogeneous line shapes – a simple Gaussian for BDPA/PS, a Zeeman powder pattern for the E' center in quartz.









#### 4. Literature Cited

1. Ya. S. Lebedev, *Appl. Magn. Res.*, **7**, 339-62 (1994).  
Ya. S. Lebedev: *Modern Pulsed and Continuous-Wave Electron Spin Resonance*, ed.L. Kevan and M. K. Bowman, Wiley, New York, pp. 365-404 (1990).  
O. Ya .Grinberg, A. A .Dubinskii, and Ya. S. Lebedev, *Russian Chemical Reviews*, **52**, 850-865 (1983).
2. See for example:  
C.T. Farrar, G.J. Gerfen, R.G. Griffin, D.A. Force, R.D. Britt *J. Phys. Chem. B* **101**, 6634-41 (1997) .  
G.J. Gerfen, B. F. Bellew, R.G. Griffin, D.J. Singel, C. A. Ekberg, and J.W. Whittaker., *J. Phys. Chem.*, **100** 16739-48 (1996).  
S. Un, X.-S. Tang, B.A. Diner, *Biochem.*, **35**, 679-84 (1996).  
K Möbius, T.F. Prisner, M. Röher *Phys. Bl* , **52**, 877-880 (1996).  
W. Wang, R.L. Belford, R.B. Clarkson, P.H. Davis, J. Forrer, M.J. Nilges, M.D. Timkin, T. Walczak, M.C. Thurnauer, *Appl. Magn. Res.* **6**, 195-215 (1994).  
D.E. Budil, K.A. Earle, J.H. Freed, *J. Phys. Chem.*, **97** 1294-1303 (1993).  
G.J. Gerfen, B.F. Bellew, S.Un, J.M. Bollinger, Jr., J. Stubbe, R.G. Griffin, and D. J. Singel. *J. Amer. Chem. Soc.*, **115**, 6420-21 (1993).  
V.I.Gulin, S.A. Dikanov, Yu.D.Tsetkov, R.G. Evelo, and A.J. Hoff, *Pure and Appl. Chem.* **64** 903-906 (1992).
3. B.F. Bellew, C.J. Halkides, G.J. Gerfen, R.G. Griffin, and D.J. Singel. *Biochem.*, **35**, 12186-12193 (1996).  
B.F. Bellew, G.J. Gerfen, C.T. Farrar, P.H.Carter, B.Ruo, D.A. Evans, R.G. Griffin, and D.J. Singel. *Biochem.*, **35**, 12194-12 (1996) .
4. I. Sildos, M. Aizengendler, I. Dolindo and I. Renge, *Optics Communications* **73**, 223-226 (1989).
5. I. Sildos, M. Aizengendler and I. Dolindo, *Optics Communications* **81**, 43-46 (1991).
6. "Persistent Spectral Hole-Burning: Science and Applications", W.E. Moerner, ed., Springer Verlag (New York) 1988.
7. B.D. Evans and M. Stapelbroek, *Solid State Comm.* **33** 765-770 (1980);  
L.S. Welch, A.E. Hughes, and G.P. Pells, *J.Phys. C: Sol. St. Phys.* **13** 1805-16 (1980);  
M.J. Springis and J.A. Valbis, *Phys. Stat. Sol. B* **123** 335-343 (1984).
8. G.J. Pogatschnik, Y. Chen, and B.D. Evans, *IEEE Trans. Nucl. Sci.* **NS-34** 1709-1712 (1987);

V.I. Baryshnikov, T.A. Kolenikova, E.F. Martynovich, and L.I. Shchepina, Opt. Spect. (USSR) **66** 544-546 (1989);

K. Atobe, N. Nishimoto, and M. Nakagawa, Phys. Stat. Sol. **89** 155-162 (1984).

9. A.-L. Barra, L.-C. Brunel, D. Gatteschi, L. Pardi, and R. Sessoli, Acc. Chem. Res. **31** 460-466 (1998).

S.M.J. Aubin, N.R. Dilley, L. Pardi, J. Krystek, M.W. Wemple, L.-C. Brunel, M.B. Maple, G. Christou, and D.N. Hendrickson, J. Am. Chem. Soc. **120** 4991-5004 (1998).

10. W. B. Lynch, R.S. Boorse, and J. H. Freed, J. Am. Chem. Soc. **115**, 10909-15 (1993).

11. D.S. Tipikin, Ya.S. Lebedev, O.G. Pouletkov, and J. Schmidt, Chem. Phys. Lett., **215**, 199-202 (1993).

S.D. Chemerisov, G.D. Perekhodtsev, D.S. Tipikin, Ya.S. Lebedev, A.I. Prokof'ev, A.I. Aleksandrov, A.A. Dubinskii, K. Möbius, O.G. Pouletkov, and J. Schmidt, J. Chem. Soc. Faraday Trans. **92** 1959-68 (1996).

12. W. M. Yen: Preparation of Single Crystal Fibers, in Insulating Materials for Optoelectronics, ed. by F. Agullo-Lopez, World Scientific, Singapore, 1995.

13. O. Burghaus, M. Roher, T. Götzinger, M. Plato, and K. Möbius, Meas. Sci. Technol. **3** 765-774 (1992).

14. G.M. Zverev and A.M. Prokhorov, Journ. Exper. Theor. Phys. (USSR) **34** 513-514 (1958); Soviet Physics JETP **7**, 354-355 (1958).

15. L.S. Kornienko and A.M. Prokhorov, Journ. Exper. Theor. Phys. (USSR) **40** 1594-1601 (1961); Soviet Physics JETP **13**, 1120-1125 (1961).

16. A.A. Manenkov and A.M. Prokhorov, Journ. Exper. Theor. Phys. (USSR) **31** 346-347 (1956); Soviet Physics JETP **4**, 288-289 (1956).

17. F.L. Galeener, Journ. Non-Cryst. Solids **149** 27-31 (1992).  
 R.A.B. Devine and J. Arndt, Phys. Rev. B **39** 5132-5138 (1989).  
 R.A.B. Devine, Journ. Non-Cryst. Solids **107** 41-48 (1988).

18. B.Buijsse, J.Schmidt, I.Y. Chan, and D.J. Singel. Phys. Rev. B **51**, 6215-20 (1995).  
 A. Regev and J.H. Freed, J. Chem. Phys **103**, 5315-5325 (1995).

19. L.-B. Lin, D.-L. Luo, C.-X. Zhang, and T.-C. Lu, Nucl. Inst. Meth. Phys. Rev. B **141** 450-454 (1998).

20. R.L. Auerbach and P.L. Richards, Phys. Rev. B **12** 2588-2595 (1975).

21. T.S. Rose, M.S. Hopkins, and R.A. Fields, IEEE Journ. Quant. Elect., **31** 1593-1602 (1995),

22. A.A. Manenkov and A.M. Prokhorov, Journ. Exper. Theor. Phys. (USSR) **28** 762 (1955); Soviet Physics JETP **1** 611 (1955).

23. E.O. Schulz-Du Bois, Bell Sys. Tech. Journ. **38** 271-291 (1959).

24. H. Klein, U. Scherz, M. Schulz, H. Setyono, and K. Wisnewski, Z. Phys. B **28** 149-157 (1977).

25. G. Kido and N. Miura, Appl. Phys. Lett. **41** 569-571 (1982).

26. J.E. Geusic, Phys Rev 102 1252-1255 (1956).

27. High-Frequency (94.9 GHz) EPR Spectroscopy of a Spin 3/2 Center in a Neutron-Irradiated Sapphire Single Crystal. D.A. Schwartz, Eric D. Walter, Sean J. McIlwain, Vladimir N. Krymov, and D.J. Singel, Appl. Magn. Res., **16** 223-236 (1999).

28. W. Yen, communication.

29. J. Weil, Phys. Chem. SiO<sub>2</sub> Si-SiO<sub>2</sub> Interface 2, eds. Helms, C. Robert; Deal, Bruce E. (Plenum, New York) 131-44 (1993).

30. <http://nctn.hq.nasa.gov/innovation/Innovation73/invents.htm>

31. Portis, A. M. (1953), Phys. Rev. **91**(5): 1071-1078; Hyde, J. S. (1960), Physical Review **119**(5): 1492-1495.

32. Farrar, C. T., G. J. Gerfen, et al. (1997), J. Phys. Chem. B **101**(33): 6634-6641.

33. Krinichnyi, V. I., S. D. Chemerisov, et al. (1997), Phys. Rev. B: Condens. Matter **55**(24): 16233-16244.

34. Dalton, L. R. (1985), EPR and advanced EPR studies of biological systems. Boca Raton, CRC Press; Thomas, D. D., L. R. Dalton, and J.S. Hyde. (1976), J. Chem. Phys. **65**(8): 3006-3024.

35. Hyde, J. S. (1960), Phys. Rev. **119**(5): 1483-1492.

36. Godbole, S. V. and M. D. Sastry (1996), J. Mag. Res. Ser. A. **122**: 78-80.

37. Mailer, C. and C. P. S. Taylor (1973). Rapid adiabatic passage EPR of ferricytochrome c: signal enhancement and determination of the spin-lattice relaxation time. Biochim. Biophys. Acta. **322**: 195-203.

38. Ammerlaan, C. A. J. and A. van der Wiel (1976), J. Magn. Reson. **21**: 387-396.

39. Rinard, G. A., R. W. Quine, B.T. Ghim, S.S. Eaton, and G.R. Eaton. (1996), J. Magn. Reson. Ser. A **122**: 58-63.

40. Froncisz, W., C. S. Lai, et al. (1985), Proc Natl Acad Sci U S A **82**(2): 411-5.

41. Portis, A.M. Technical note No.1, Sarah Mellon Scaife Radiation Laboratory, University of Pittsburgh 1955 (unpublished); Portis, A. M. (1955) Phys. Rev. **100**: 1219-1221. Portis, A. M. (1998), Foundations of Modern EPR. G. R. Eaton, S. S. Eaton and K. M. Salikhov. Singapore, World Scientific Publishing Co.

42. Weger, M. (1960), Bell Sys. Tech. J. **39**: 1013-1112.

43. Cullis, P.R., Journ. Mag. Res. **21** (1976) 397-418.

44. Ruyten, W. M. (1990), *Phys. Rev. A* **42**(7): 4226-4245.
45. Robinson, B. H. (1983), *J. Chem. Phys.* **78**(5): 2268-2273; Robinson, B. H., C. Mailer, et al. (1999), *J. Magn. Reson.* **138**(2): 199-209.
46. Tsukada, N. and T. Ogawa (1973). *J. Phys. B: Atom. Molec. Phys.* **6**: 1643-49.
47. Grivet, J. (1993). *Am. J. Phys.* **61**(12): 1133-1139.
48. Press, W. H., S. A. Teukolsky, et al. (1995). *Numerical recipes in C*. Cambridge, Cambridge University Press.

## **Appendix I**

### **Schematics and Specification of the 94.9 GHz Microwave Bridge**

MICROWAVE HETERODYNE TWO-CHANNEL BRIDGE  
OF THE COHERENT W-BAND EPR SPECTROMETER  
FOR PULSED AND CW EXPERIMENTS

**Applications**

The high-frequency bridge represents a multifunctional W-band transmitter-receiver module (TRM) intended for an EPR spectrometer operation. The TRM has two coherent transmitter channels to form a probing signal at the central frequency of 94.9 GHz with the maximum total power of 280 mW as well as the high-sensitive receiver with double frequency conversion for an EPR signal detection.

Being capable of either pulsed or CW coherent operation, the system can be operated in several configurations. If integrated into measuring equipment the TRM can be employed in scientific research.

**System Description and Functional Characteristics**

A simplified functional block diagram of the TRM is shown in figure 1. The system consists of several main blocks: the double-channel transmitter, the receiver with double frequency conversion, the master oscillator (STAMO), and the transmission-reception circulator. The system performs in the following manner. The STAMO supplies coherent centimeter-wave driving signals. These signals are transferred to W-band by an IMPATT Frequency Multiplier with multiplication factor as high as 13. The transfer is realized in the transmitter channels and receiver heterodyne 1 without significant phase noise degradation.

The transmitter signal AM and two-level phase-shift keying (2PSK) are accomplished by means of external TTL control pulses supplied to the transmitter channels. The power gain is achieved due to 3-stage CW IMPATT Amplifiers. The TRM can be operated in an External Synthesizer configuration to attain the best frequency stability and possibility of frequency adjustment. Coherent summation of the outputs of two transmitter channels is carried out by means of an E-H Hybrid Tee.

The receiver is designed on the basis of a double frequency conversion circuit and has two outputs which are 90° out of phase. The Balanced Mixer input of the receiver is protected with a High-Speed PIN Switch which provides maximum attenuation while the transmitter signals pass. For the transmitter noise to be suppressed during a pause between the transmitter pulses another High-Speed PIN Switch is included at the transmitter output.

## STAMO

As mentioned above, the STAMO provides the coherent centimeter-wave driving signals for both the transmitter and receiver and can perform in two configurations.

**1. Internal Stabilized Oscillator Configuration.** In this configuration, the TRM performs at a constant frequency of 94.9 GHz. The system output frequency stability is determined by the stability of a Transistor Oscillator at 7.16 GHz stabilized with a high-Q Dielectric Resonator.

**2. External Synthesizer Configuration.** In this configuration, the reference frequency signal  $(7.16 \pm 0.004)$  GHz is sampled from an External Synthesizer. The operating output frequency in the range of  $(94.9 \pm 0.05)$  GHz and output frequency stability are determined by the External Synthesizer signal parameters.

As seen from figure 1, the STAMO forms the following signals:

1) the signal for driving the transmitter channel 1.

The central frequency is 7.3 GHz.

2) the signal for driving the transmitter channel 2.

The central frequency is 7.3 GHz. There is placed a manually adjustable phase shifter in the channel.

3) the signal for driving the receiver heterodyne 1.

The central frequency is 7.16 GHz. There is placed a manually adjustable phase shifter in the channel.

4) the signal for driving the receiver heterodyne 2.

The central frequency is 1.82 GHz.

5) the signal for testing the transmitter reference frequency.

An interconnection scheme of the STAMO is shown in figure 2.

### Transmitter

The transmitter comprises two identical coherent channels. Each transmitter channel is a converter-amplifier appliance which enables transferring the STAMO signal at 7.3 GHz into the signal at 94.9 GHz without significant noise phase degradation and amplifying the last one up to  $\sim 300$  mW. Efficient frequency conversion is carried out by an IMPATT CW Frequency Multiplier with a multiplication factor as high as 13 and conversion losses no more than 16 dB. The transmitter channel power gain is carried out by means of a 3-stage IMPATT CW Amplifier with 17 dB gain.

For output power control, included at the output of each transmitter channel is a current-controlled PIN Attenuator with power suppression of 40 dB. The output signal AM for each transmitter channel is realized by 2-stage High-Speed PIN Switches 1,2 with isolation of 70 dB

and switching time about of 10 ns. Such a value of isolation is attained due to the architecture of these 2-stage Switches both consisting of two High-Speed PIN Switches connected in series.

The output signal  $[0-\pi]$  2PSK for each transmitter channel is carried out by means of a High-Speed PIN Two Level Phase Shifter. Coherent summation of the outputs of two transmitter channels is provided by the E-H Hybrid Tee, as mentioned above.

To suppress the noise of amplifying stages during a pause between the pulses High-Speed PIN Switch 3 with suppression no less than 30 dB is included at the transmitter output.

At the transmission-reception Circulator output each of the transmitter channels supplies an output power no less than 70 mW, the maximum total power of both channels being about of 280 mW at the central frequency.

### Receiver

The receiver is designed on the basis of a double frequency conversion circuit. The STAMO sends two signals to the receiver: the driving signal for the receiver heterodyne 1 at 7.16 GHz and that for the receiver heterodyne 2 at 1.82 GHz. An IMPATT CW Frequency Multiplier converts the 7.16 GHz signal into the 93.08 GHz signal with a multiplication factor as high as 13 in heterodyne 1 track. For the Multiplier AM noise to be suppressed a Band-Pass Filter is placed within heterodyne 1 track.

The heterodyne power enters the Balanced Mixer input through High-Speed PIN Switch 4 due to which it is modulated. The heterodyne power modulation is injection-locked with the transmitter outputs and thus the linear behaviour of the receiver is provided.

An EPR signal enters the Balanced Mixer signal input through the transmission-reception Circulator. The signal input of the Balanced Mixer is protected with High-Speed PIN Switch 5. A series of the transmitter signals passing, the Switch provides isolation of 40 dB.

The IF signal at 1.82 GHz is amplified by a Low-Noise Preamplifier, divided by two equal parts and they enter the inputs of Mixers. The IF signal bandwidth is 150 MHz and is determined by a bandwidth of the Band-Pass Filter. After the second frequency conversion the receiver has two outputs which are out of phase at the zero IF. The receiver provides a noise figure no more than 12.5 dB and power gain 20 dB with a through frequency band no less than 150 MHz.

An interconnection scheme of the TRM is shown in figure 3.

## Product Design

The product is fabricated as a stand-alone unit with dimensions  $470 \times 300 \times 120 \text{ cm}^3$ . Led out on the back panel is the unit waveguide output connected to the EPR spectrometer waveguide. The waveguide size is WR-10. The waveguide flange is UG-387/U.

On the front panel, as seen from figure 4, there are allocated all of the controls of the unit as well as the supply voltage connector, the latter being arranged in the left lower corner of the panel. The microwave coaxial connectors OSM(SMA) Jack are utilized for control signals to be supplied.

EPR SIGNAL OUTPUT 1 - second IF output of channel 1 of the receiver.

EPR SIGNAL OUTPUT 2 - second IF output of channel 2 of the receiver which has  $90^\circ$  of phase shift with respect to OUTPUT 1.

R PS ADJ - manual phase adjustment for the receiver heterodyne 1.

T PS ADJ - manual phase adjustment for the transmitter channel 2.

RF TEST - (the left side of the panel) the transmitter reference frequency testing at 7.3 GHz.

EXT-INT - operating configuration switch. "EXT" position corresponds to the External Synthesizer configuration whereas "INT" position corresponds to the Internal Stabilized Oscillator configuration.

RF EXT IN - External Frequency Synthesizer input at  $(7.16 \pm 0.004) \text{ GHz}$ .

TST ON - thermostat system switch for the Transistor DRO at 7.16 GHz.

REC CONT TTL GATE - the receiver control connector.

While applying TTL pulses, PIN Switch 5 included at the receiver input is on provided these pulses are not injection-locked to the pulses of the transmitter channels.

TRANS CONT - series of the transmitter control connectors:

AM CHAN-1 TTL TRIG - connector for the transmitter AM to be triggered by TTL control pulses supplied to channel 1.

AM CHAN-2 TTL TRIG - connector for the transmitter AM to be triggered by TTL control pulses supplied to channel 2.

2PSK CHAN-1 TTL TRIG - connector for the transmitter  $[0-\pi]$  two-level phase-shift keying (2PSK) to be triggered by TTL control pulses supplied to channel 1.

2PSK CHAN-2 TTL TRIG - connector for the transmitter  $[0-\pi]$  2PSK to be triggered by TTL control pulses supplied to channel 2.

ATT CONTROL DC CHAN-1 - connector for the transmitter output to be attenuated by control DC supplied to channel 1.

AT1 CONTROL DC CHAN-2 - connector for the transmitter output to be attenuated by control DC supplied to channel 2.

#### OPER MODE

PULSE-CW - the TRM operating mode switch. "PULSE" position corresponds to the pulsed mode whereas "CW" position corresponds to the CW mode of operation.

MEASUR-TUNING - operating submode switch which allows the TRM to pass from tuning condition to measuring one.

#### **Pulsed mode**

In the pulsed mode, the TRM supplies AM modulated microwave output. For each transmitter channel the microwave pulse length and period of pulse repetition are determined by the parameters of the TTL control pulses supplied to the input connectors TTL TRIG AM CHAN-1 and TTL TRIG AM CHAN-2.

Turning on and off the receiver is attained by the TTL control pulses supplied to the connector TTL GATE. The transmitter signal AM and the receiver switching are carried out by means of five High-Speed PIN Switches (see block diagram, figure 1).

High-Speed PIN Switch 1 provides the transmitter channel 1 output AM with isolation of 70 dB.

High-Speed PIN Switch 2 provides the transmitter channel 2 output AM with isolation of 70 dB.

High-Speed PIN Switch 3 with isolation of 30 dB introduces an additional depth of modulation of the transmitter output and suppresses the CW IMPATT Amplifier noise of the transmitter channels 1 and 2 during a pause between microwave power pulses as well.

The transmitter power flowing, High-Speed PIN Switch 4 turns off the receiver heterodyne 1 power, which permits the receiver to perform in linear conditions.

High-Speed PIN Switch 5 with isolation of 40 dB protects the receiver Balanced Mixer from the transmitter microwave power pulses.

For the proper order of switching on and off the High-Speed PIN Switches there is a logic and five drivers in the system. Figure 5 shows a switching scheme of the High-Speed PIN Switches as a function of the control signals derived from the External TTL Pulse Oscillator and supplied to the control connectors TTL TRIG AM and TTL GATE.

"On" Switch state corresponds to the minimum loss performance, while "Off" state corresponds to the maximum isolation performance.

The TTL high ("1") signal supply to the input connector TTL TRIG AM results in the transmitter channels power being emitted while the TTL low ("0") signal supply causes their power being suppressed.

The receiver is driven by the control signal entering the input connector TTL GATE, the TTL high ("1") signal turning the receiver on and TTL low ("0") signal turning the receiver off. However (as seen from figure 5, versions a, b, c), any transmitter channel emitting microwave power pulses, the receiver is always off irrespective of a signal at the control connector TTL GATE. The receiver is on only for a case of the transmitter power being suppressed when the TTL high signal enters the connector TTL GATE (version e). This prevents the possibility of the Balanced Mixer failure.

While operating in the pulsed mode, there is the possibility of 2PSK the output signal for each transmitter channel. The TTL low or TTL high signal supply to the input connector 2PSK CHAN-1 TTL TRIG results in  $180^\circ$  of phase change of the transmitter channel 1 output. The TTL low or TTL high signal supply to the input connector 2PSK CHAN-2 TTL TRIG results in  $180^\circ$  of phase change of the transmitter channel 2 output.

The output pulse power of each transmitter channel can be attenuated by a control current supply to the input connectors ATT CONTROL DC CHAN-1 and ATT CONTROL DC CHAN-2. Figure 6 shows the attenuation as a function of a control current for channel 1 and channel 2.

The pulsed mode has two submodes: the measuring submode and tuning one.

In the measuring submode, the transmitter emits microwave power pulses which duration and period of repetition are determined by the control pulse parameters. After double frequency conversion and addition-subtraction processing the EPR signal detected by the receiver is sent to the connectors EPR SIGNAL OUTPUT 1 and EPR SIGNAL OUTPUT 2. The output signals at these connectors have  $90^\circ$  of phase shift with respect to each other. In the measuring submode, the transmitter microwave pulses don't penetrate into the receiver due to high isolation between the receiver and transmitter.

Tuning submode is employed for the EPR spectrometer resonator being tuned. In this submode, isolation between the transmitter and receiver is intentionally reduced, which is achieved by switching High-Speed PIN Switch 4 to "on" state, and as a result the receiver heterodyne 1 power enters the Balanced Mixer even though for a case of the transmitter pulses being emitted.

### CW Mode

In the CW mode, the TRM supplies an output power of 5 mW. There is utilized only channel 2 of the transmitter in this mode. Channel 1 of the transmitter is completely off.

So as to avoid the Balanced Mixer overload and failure the current-controlled PIN Attenuator included at the output of channel 2 introduces continued attenuation of 8 dB. The output power control can be accomplished only towards power level reduction.

In the CW mode, High Speed PIN Switches 2,3,4,5 are in "on" state, which corresponds to the minimum insertion loss performance. The High-Speed PIN Two Level Phase Shifter of channel 2 is off.

### Operating Order

1. Attach the TRM output waveguide flange to the waveguide track of the EPR spectrometer.

2. Supply the TRM with voltages by means of a feeding cable in accordance with a table of supply voltages.

**Attention.** The voltage of +12 V is allowed to be applied to the supply voltage connector only after supplying the voltage of minus 12 V. Turning the supply voltages off should be performed in a reverse order.

3. While operating in the Internal Stabilized Oscillator configuration, put the switch INT-EXT (the right side of the panel) into "INT" position.

Testing of the transmitter reference frequency of 7300 MHz can be carried out by connecting a frequency meter to the connector RF TEST. The testing signal power at the connector RF TEST is about 1 mW.

4. While operating in the External Synthesizer configuration, supply the External Synthesizer signal to the connector RF EXT IN. The signal frequency is within the range (7156-7164) MHz. The Synthesizer power output is of (5-10) mW.

Put the switch INT-EXT (the right side of the panel) into "EXT" position.

5. While operating in the pulsed mode, put the switch PULSE-CW into "PULSE" position.

While tuning the EPR spectrometer resonator, put the switch MEASUR-TUNING into "TUNING" position.

While measuring, put the switch into "MEASUR" position.

The control signals should be supplied to the connectors REC CONT and TRANS CONT in accordance with a section: Pulsed Mode.

The transmitter channel 2 phase adjustment should be carried out by turning the knob T PS ADJ.

The receiver heterodyne 1 phase adjustment should be carried out by turning the knob R PS ADJ.

After double frequency conversion the EPR signal detected by the receiver enters the connectors EPR SIGNAL OUTPUT 1 and EPR SIGNAL OUTPUT 2. The output signals at these connectors have 90° of phase shift with respect to each other.

6. While operating in the CW mode, put the switch PULSE-CW into "CW" position and the switch MEASUR-TUNING put into "MEASUR" position.

The transmitter channel 2 phase adjustment should be carried out by turning the knob T PS ADJ.

The receiver heterodyne 1 phase adjustment should be carried out by turning the knob R PS ADJ.

After double frequency conversion the EPR signal detected by the receiver enters the connectors EPR SIGNAL OUTPUT 1 and EPR SIGNAL OUTPUT 2. The outputs at these connectors have 90° of phase shift with respect to each other.

#### Duty conditions

1. The product is to be incorporated in the EPR spectrometer and employed for in-door operation under standard climatic conditions free of mechanical perturbations:

- Ambient Temperature, °C ..... 25±10
- Relative Humidity, % ..... 70

2. The product should be installed so that a value of an external magnetic field and its deviation for a single EPR experiment could not exceed 1 mT and 0.02 mT, respectively.

3. **A t t e n t i o n.** While transporting, storing, assembling, and operating, it is necessary to preclude entering any particles (especially magnetic ones) into the waveguide channel so as to avoid the product failure.

4. Warming-up time after switching on is 1 hour (max).

5. Continuous duty time is 8 hours.

6. Guarantee period is 2 years.

# SPECIFICATIONS

## 1. TRANSMITTER

### *PULSE MODE*

#### *Internal Stabilized Oscillator Configuration*

Characteristic, units	Standards of Performance Specifications	Measured Value
1. Output frequency fixed, GHz	94.90	94.900
2. Output frequency instability, kHz/h	150	130
3. Output spectral linewidth at the level -3dB, kHz	6	< 3
4. AM noise with offset from carrier, dB/Hz		
1 kHz	-120	-120
10 kHz	-130	-130
100 kHz	-135	-135
5. Output power of channel 1, mW	65	69
6. Output power of channel 2, mW	65	70
7. Output power attenuation range, dB		
Channel 1	40	60
Channel 2	40	60
8. Maximum output power of two channels, mW	250	275
9. Microwave pulse duration at the level -3dB, ns		
min	20	20
max	continuous	continuous
10. Pause duration between microwave pulses, ns		
min	20	20
max	continuous	continuous
11. Microwave power switching time at the level 0.1/0.9, ns	5	<3
12. Microwave power suppression during a pause between pulses, dB	90	100
13. Switching time up to maximum suppression level, ns	10	10
14. Accuracy of 180 deg phase shift keeping of 2PSK for 94.9 GHz frequency, deg	-	<2
15. Switching time for 2PSK, ns	-	<5
16. Output parasite AM level for 2PSK, dB	1	<1

## 2. TRANSMITTER

### PULSE MODE

#### *External Synthesizer Configuration*

Characteristic, units	Measured Value				
1. Output frequency, GHz	94.770	94.835	94.900	94.965	95.030
2. Output power of channel 1, mW	76	73	69	66	64
3. Output power of channel 2, mW	66	68	70	71	72
4. Maximum output power of two channels, mW	282	280	275	273	270
5. Microwave power suppression during a pause between pulses, dB	>100	>100	>100	>100	>100
6. Accuracy of 180 deg phase shift keeping for 2PSK, deg	3	2	1	1	1
7. Output parasite AM level for 2PSK, dB	<1	<1	<1	<1	<1

## 3. TRANSMITTER

### CW MODE

Characteristic, units	Measured Value				
1. Output frequency, GHz	94.770	94.835	94.900	94.965	95.030
2. Output power, mW	5.4	5.5	5.5	5.5	5.4

## 4. RECEIVER

#### *Internal Stabilized Oscillator or External Synthesizer Configurations*

Characteristic, units	Measured Value				
1. Input signal frequency, GHz	94.770	94.835	94.900	94.965	95.030
2. Noise figure, dB	10.7	11.1	11.6	11.8	11.7
3. Power gain, dB	EPR signal 1	22.5	22.5	22.5	22.0
	EPR signal 2	22.0	22.0	22.0	22.0
4. Through band, MHz	200				

## 5. TRANSMITTER - RECEIVER

1. Total phase drift - 5deg/15 minutes.
2. Manual signal phase adjustment for channel 2 - more than 360 deg.
3. Manual signal phase adjustment for receiver heterodyne 1 - more than 360 deg.

## 6. SUPPLY VOLTAGE AND DRAIN CURRENT PARAMETERS

Supply Voltage	Drain Current	
	Pulsed Mode	CW Mode
$U_1 = +27V \pm 1V$	$I_1 = 1.82-1.53 A$	$I_1 = 0.9 A$
$U_2 = +12V \pm 0.5V$	$I_2 = 2.5 A$	$I_2 = 1.97 A$
$U_3 = -12V \pm 0.5V$	$I_3 = 0.45 A$	$I_3 = 0.42 A$

## 7. THE TTL CONTROL PULSE PARAMETERS

TTL high ("1")  $(+2.4 - +4) V$

TTL low ("0")  $(0 - +0.4) V$

Switching time  $0.1/0.9 \times V$  no more than 1 ns

Load resistance 50 ohm

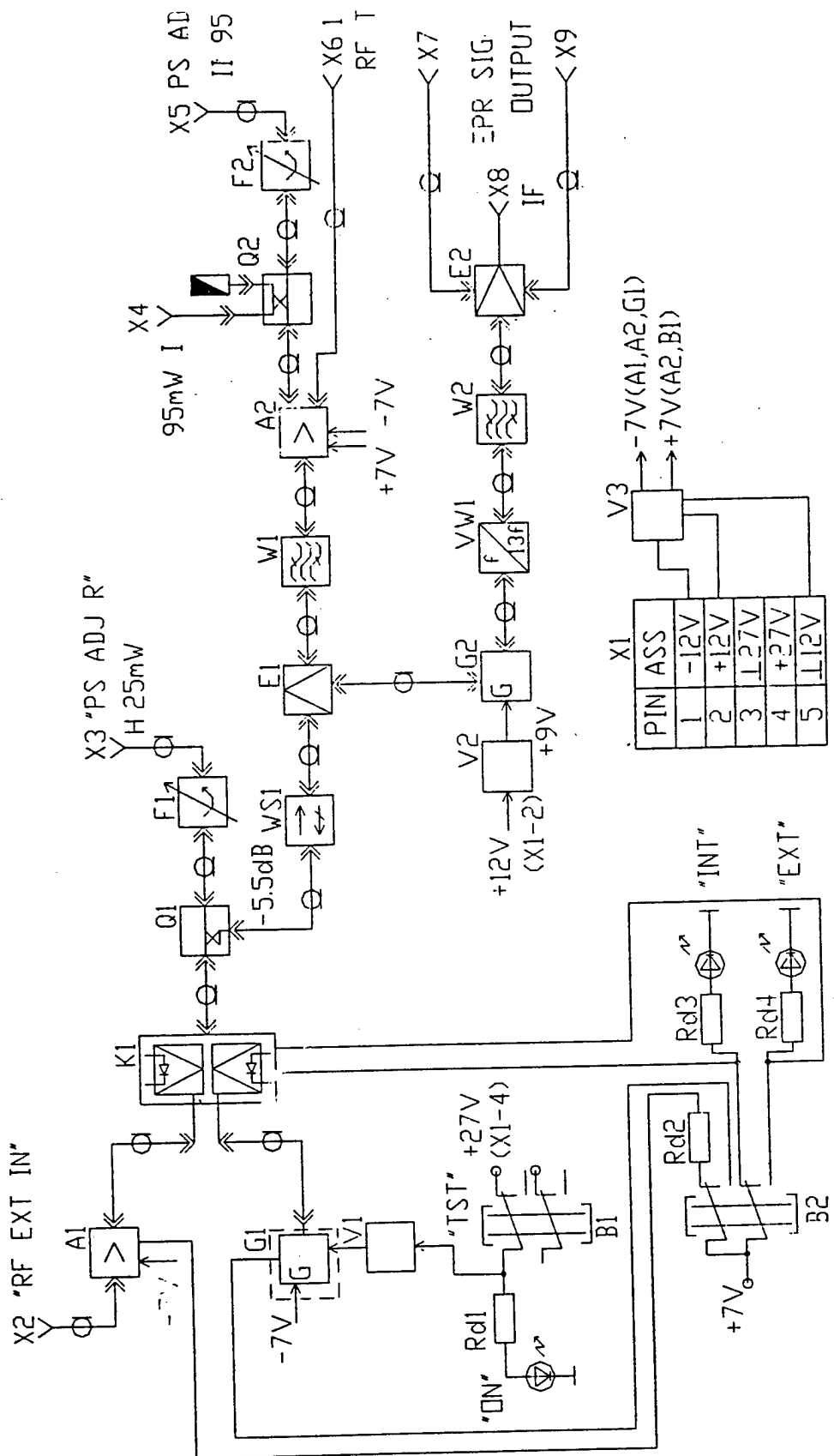
## 8. REFERENCE DATA

1. The output power at the connector RF TEST is about 1.6 mW.

2. The input power supplied by the External Synthesizer to the connector RF EXT IN is (5-10) mW.

3. The output signal frequency of the transmitter is related to the input signal frequency of the External Synthesizer by the following relationship:

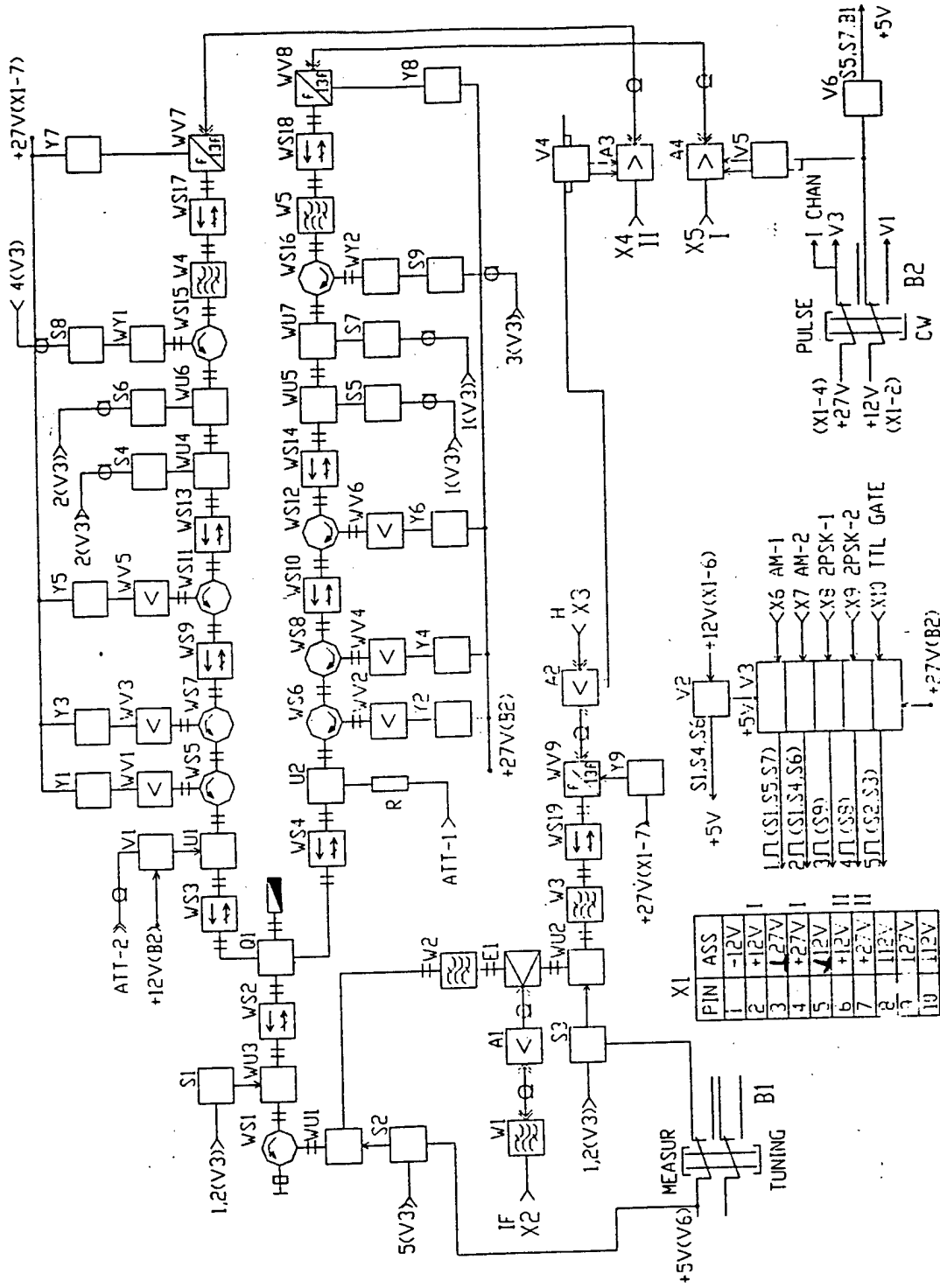
$$F_{out\ T}(\text{MHz}) = [F_{input\ syn}(\text{MHz}) + 140] \times 13.$$



## Interconnection scheme of STAMO (module B).

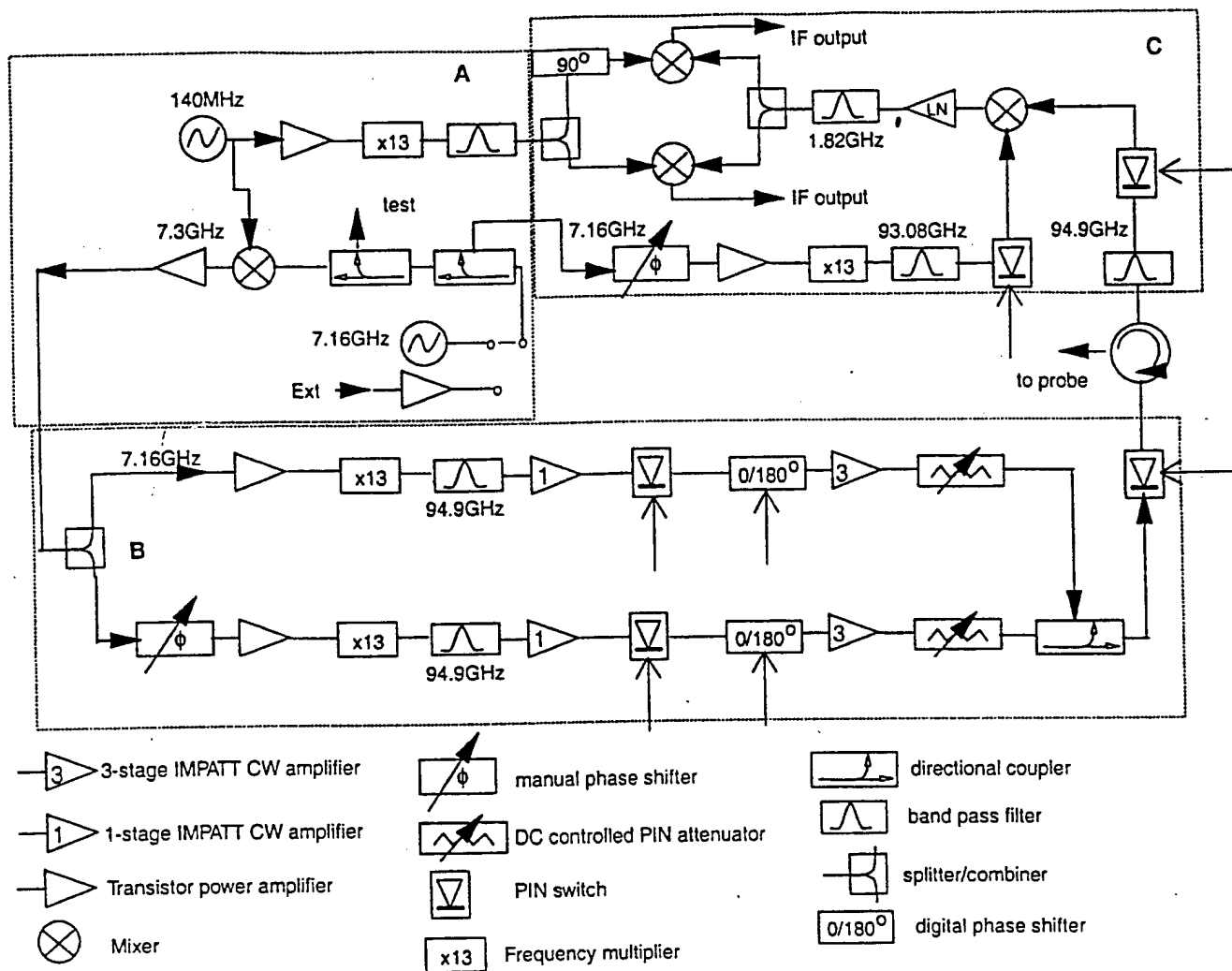
Component Designation	Component Name
G1	Transistor DRO
G2	Reference Crystal Oscillator
A1÷A2	Transistor Power Amplifier
W1÷W2	IF Band Pass Filter
Q1	Microstrip Directional Couple.
Q2	Microstrip Power Divider
F1, F2	Manual Adjust Coaxial Phase Shifter
E1	SSB Upconverter
E2	Double-Output Mixer
WV1	Frequency Multiplier $\times 13$
V1	Thermostat Control Circuit
V2, V3	Regulation Circuit
B1÷B2	Switch
K1	Coaxial Switch
X1	Voltage Supply Connector
X2÷X9	Connector OSM (SMA)

List of Component to Interconnection Scheme of  
the STAMO



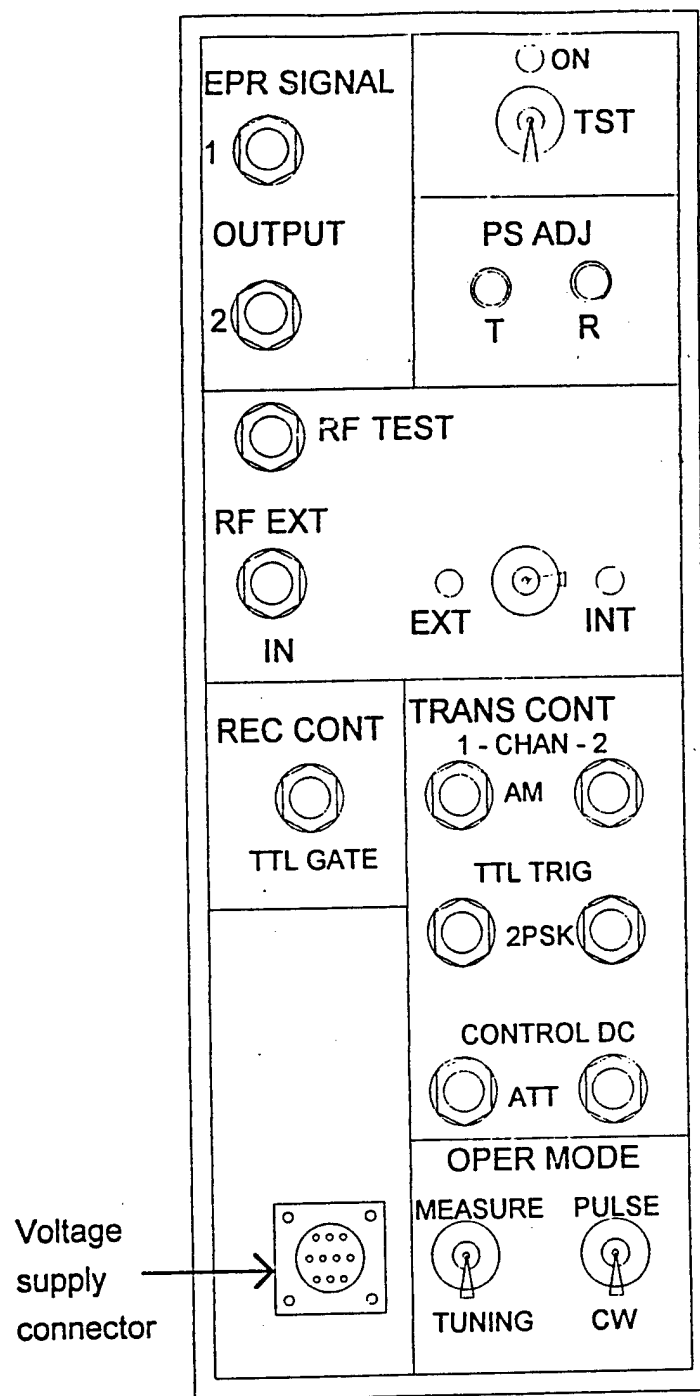
Component Designation	Component Name
WS1÷WS19	Waveguide Circulator
WV7÷WV9	IMPATT CW Frequency Multiplier
WV1÷WV6	IMPATT CW Amplifier
WU1÷WU7	High-Speed PIN Switch
WY1, WY2	High-Speed PIN Two Level Phase Shifter
U1, U2	PIN Attenuator
S1÷S9	Driver
Y1÷Y9	Current Regulator
W1	IF Band Pass Filter
W2÷W5	Waveguide Band Pass Filter
E1	Balanced Mixer
Q1	E-H Hybrid Tee
A1	Low Noise Preamplifier
A2÷A4	Transistor Power Amplifier
V1÷V6	Voltage Regulator and Control Circuit
X1	Voltage Supply Connector
X2÷X5	Connector OSM (SMA)
X6÷X10	Connector OSM (SMA)
B1, B2	Switch

List of Component to Interconnection Scheme of  
the Transmitter-Receiver Module (fig.3).

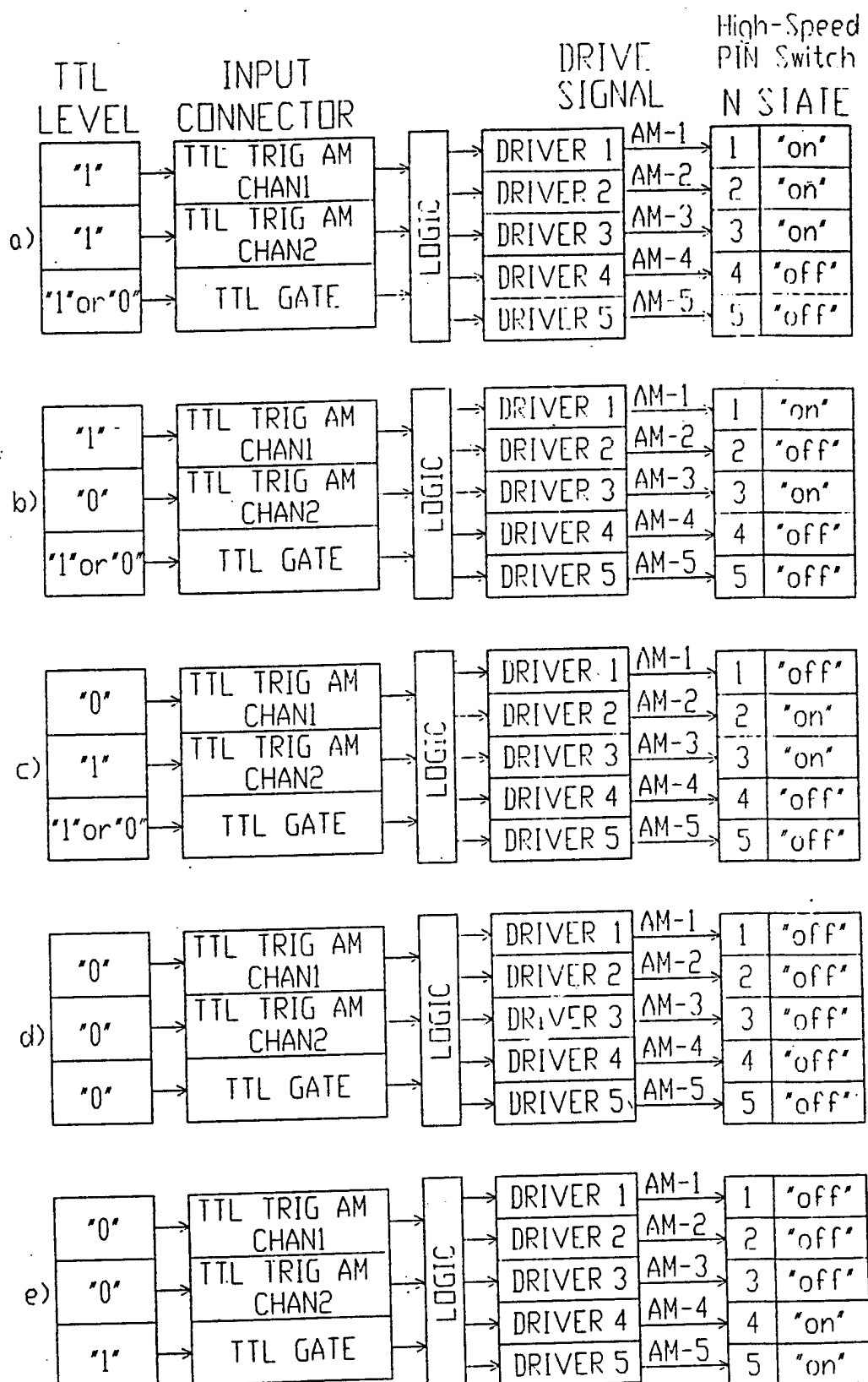


#### 94.9 GHz EPR spectrometer microwave bridge

Block diagram showing the W-band spectrometer bridge. The high stability (STAMO) master frequency oscillator system lies in block (A) of the diagram. The two-channel, phase-adjustable, pulsed transmitter assembly lies in block (B). Block (C) is the quadrature receiver unit.

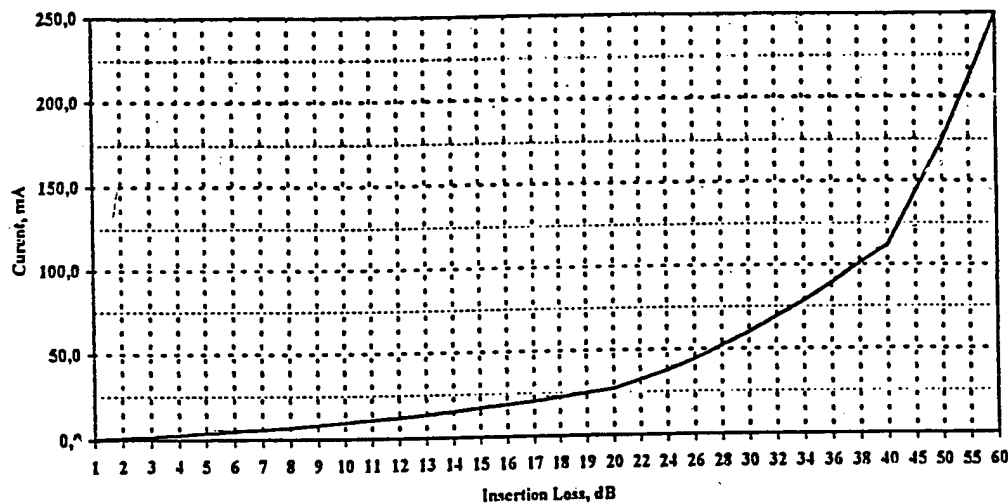


Front Panel



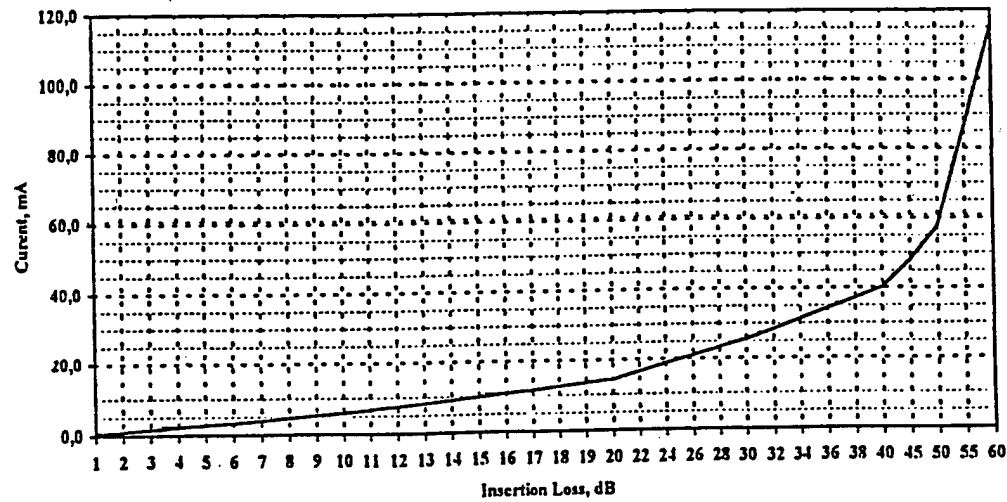
Switching Scheme.

I,mA	0.59	1.28	1.96	2.78	3.68	4.62	5.64	6.72	8.05	9.35	10.72	11.98	13.57	15.04	17.04
$\alpha$ ,dB	1	2	3	4	5	6	7	8	9	10	11	12	13	14	15
I,mA	18.54	20.4	22.5	24.9	27.1	32.4	37.8	44.4	52.1	59.7	69.1	78.4	89.3	101	111
$\alpha$ ,dB	16	17	18	19	20	22	24	26	28	30	32	34	36	38	40
I,mA	144	174	210	250											
$\alpha$ ,dB	45	50	55	60											



Microwave power attenuation as a function of a current value.(Channel I)

I,mA	0.51	1.03	1.6	2.14	2.72	3.3	3.393	4.6	5.28	5.98	6.7	7.52	8.25	9.08	9.91
$\alpha$ ,dB	1	2	3	4	5	6	7	8	9	10	11	12	13	14	15
I,mA	10.8	11.6	12.54	13.45	14.44	16.58	18.78	21.0	23.4	25.9	28.5	31.4	34.3	37.1	40.2
$\alpha$ ,dB	16	17	18	19	20	22	24	26	28	30	32	34	36	38	40
I,mA	48.1	57.7	86.4	115.5											
$\alpha$ ,dB	45	50	55	60											

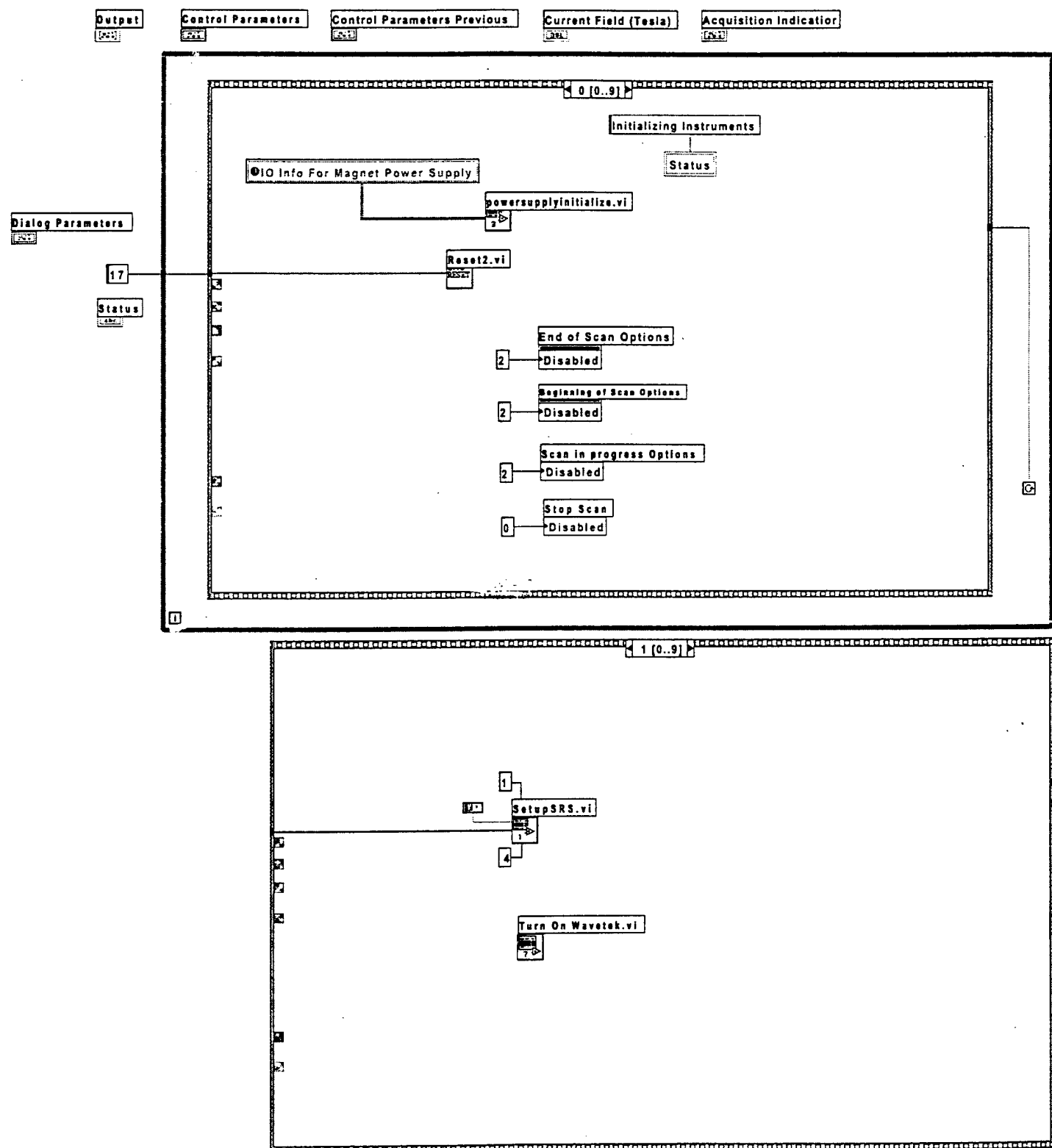


Microwave power attenuation as a function of a current value. (Channel II)

## **Appendix II**

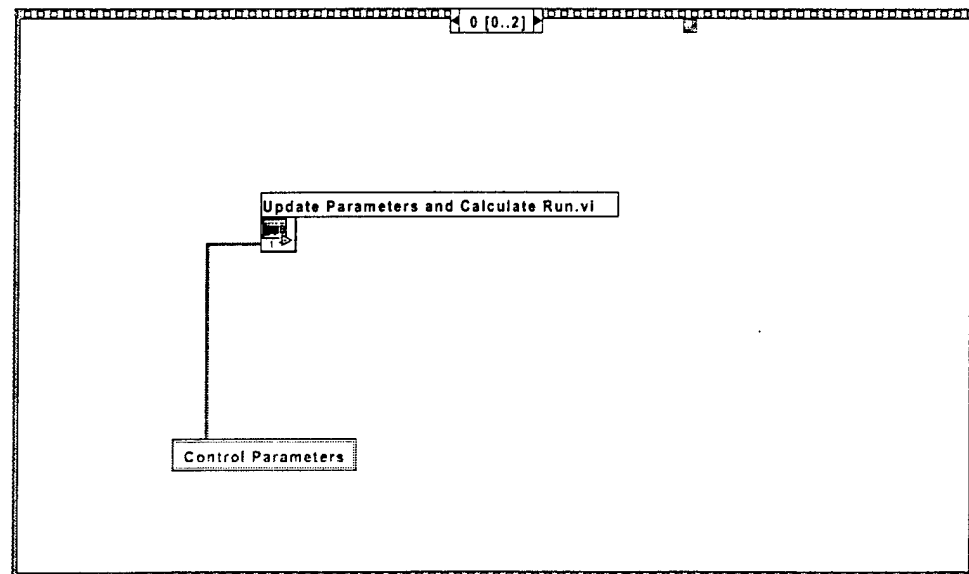
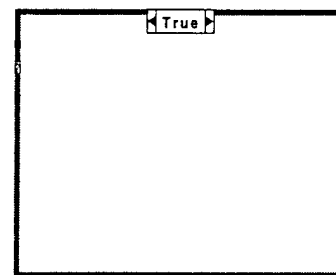
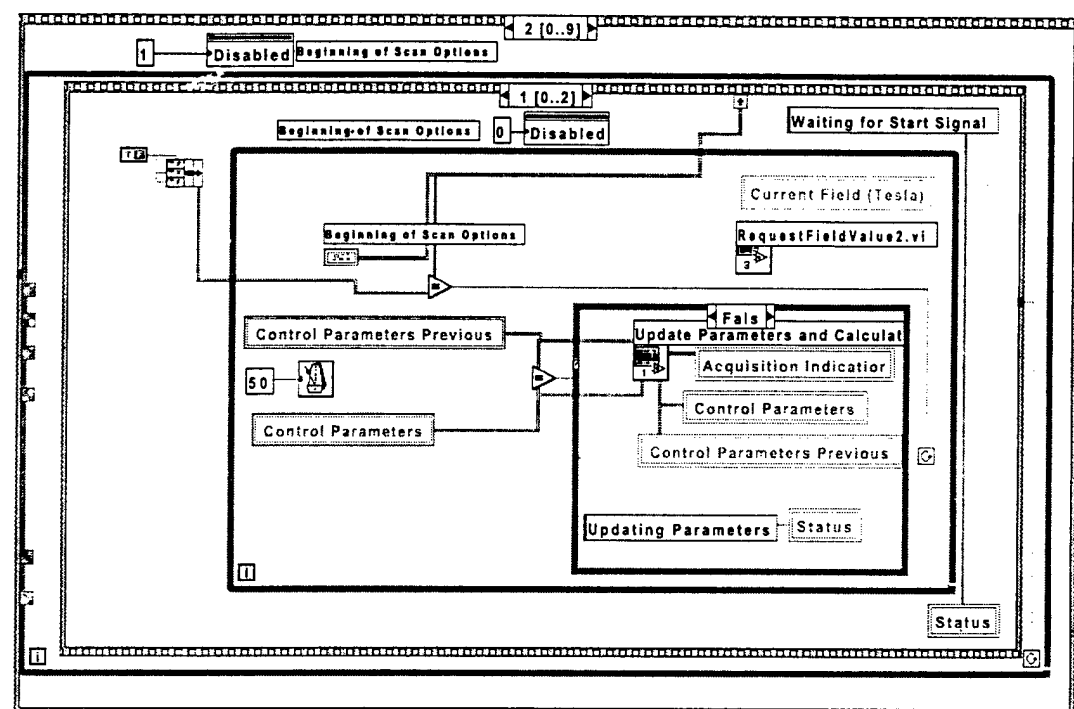
### **LabVIEW Code for EPR Spectrometer Control, Data Acquisition, and Manipulation**

Labview Routine for EPR Control and Data Acquisition: Labview Code

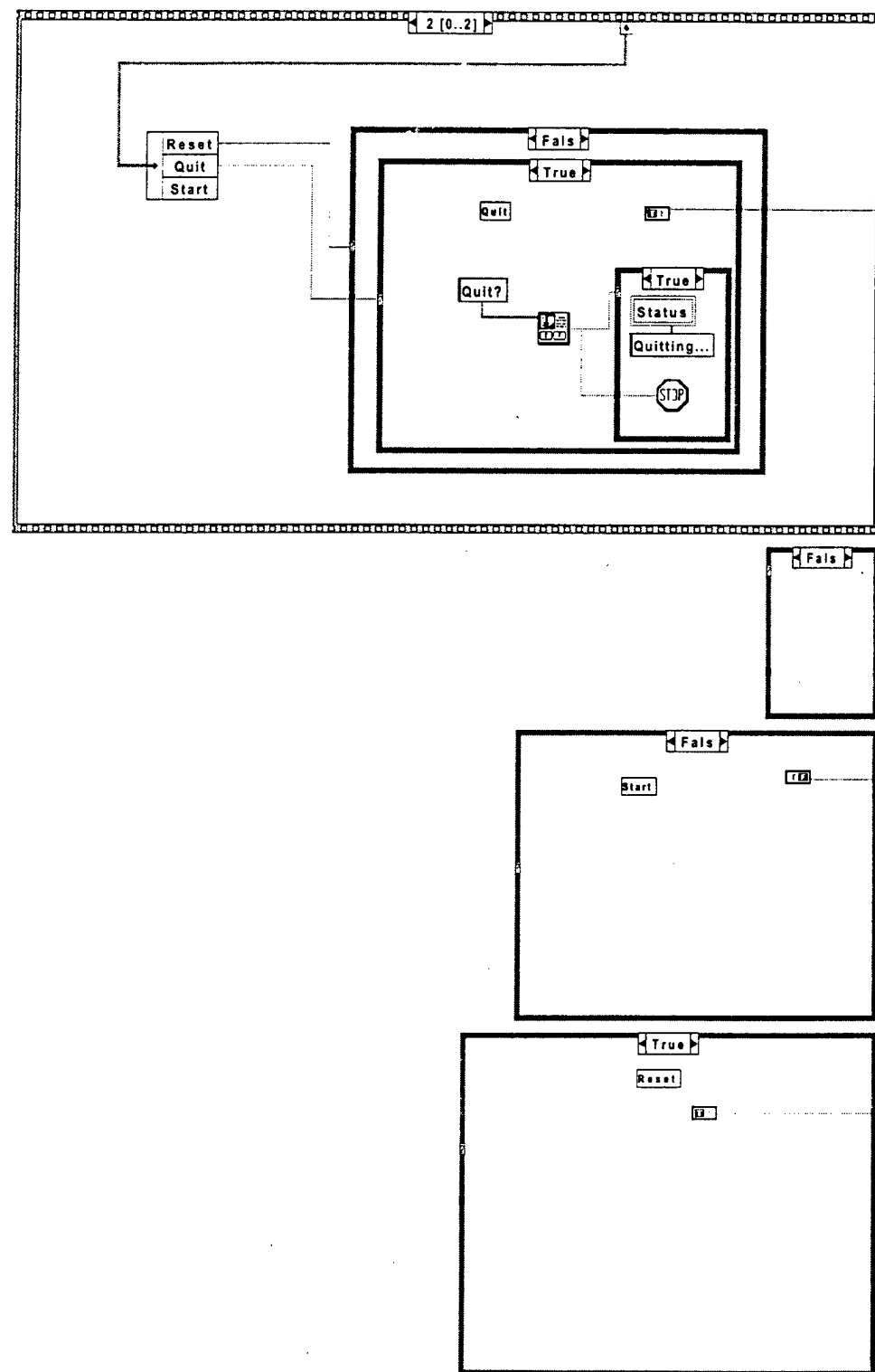


# epr program version 1.5.5.vi

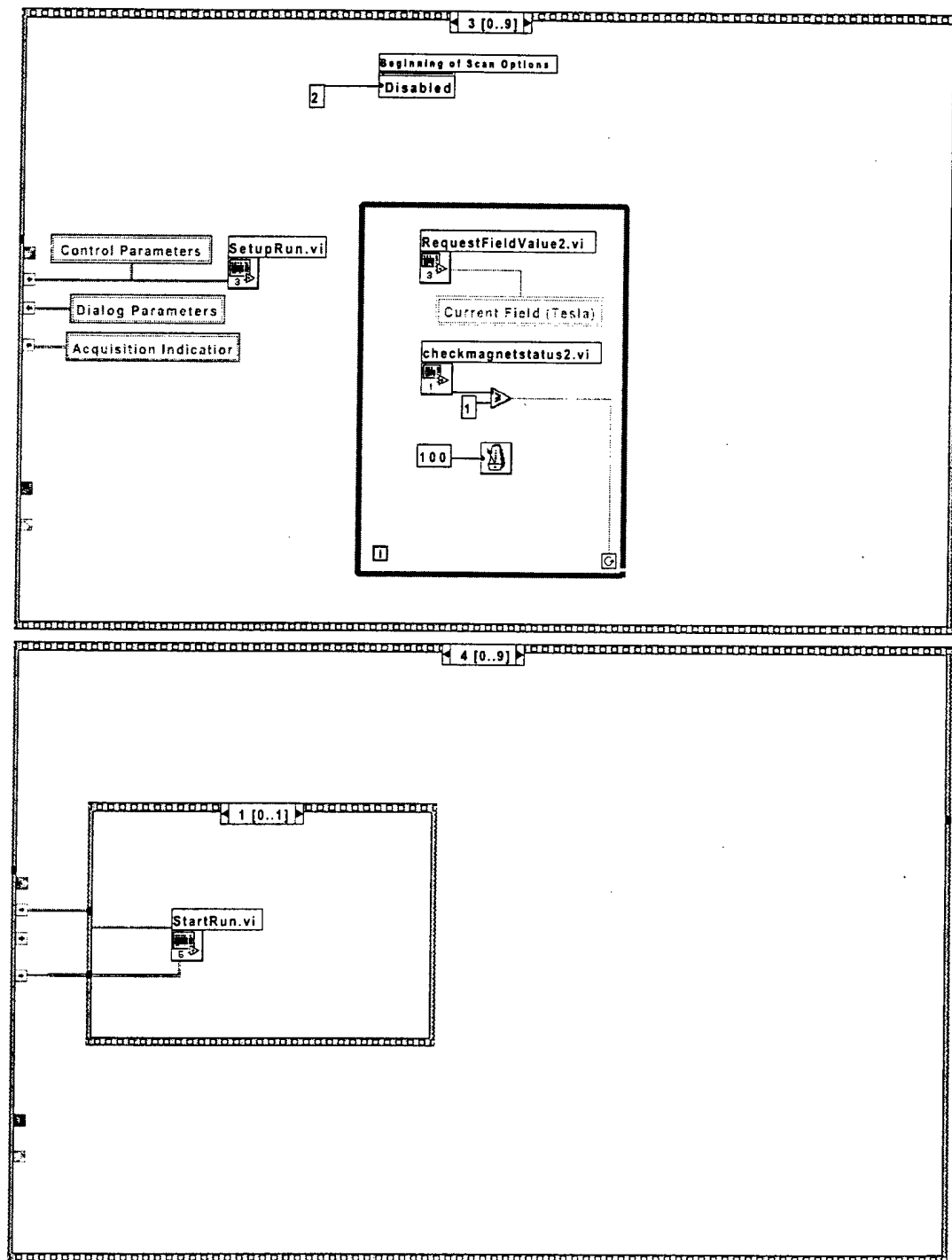
1



# epr program version 1.5.5.vi

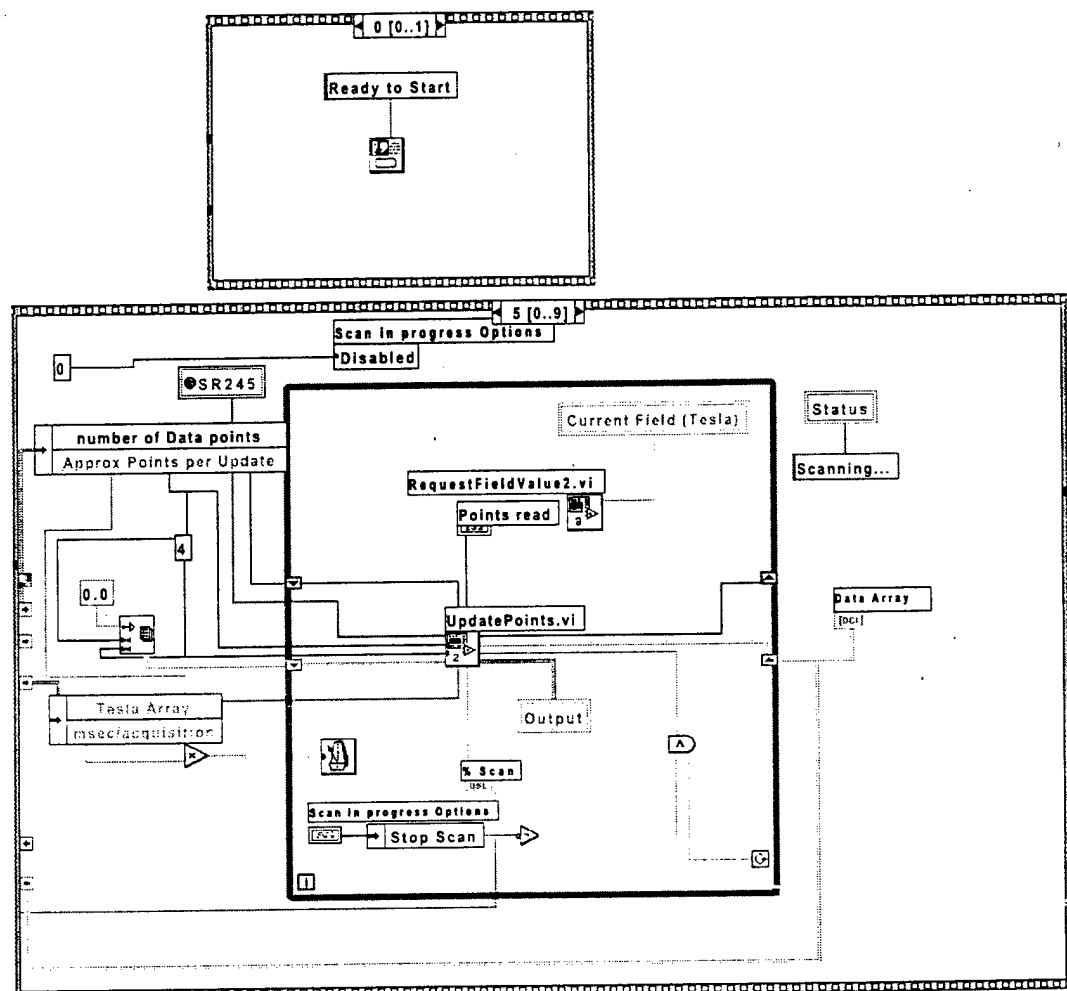


## epr program version 1.5.5.vi



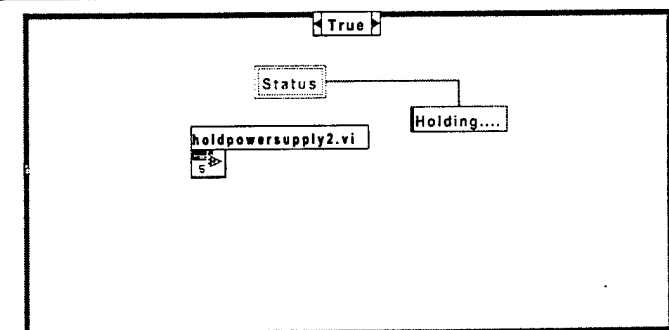
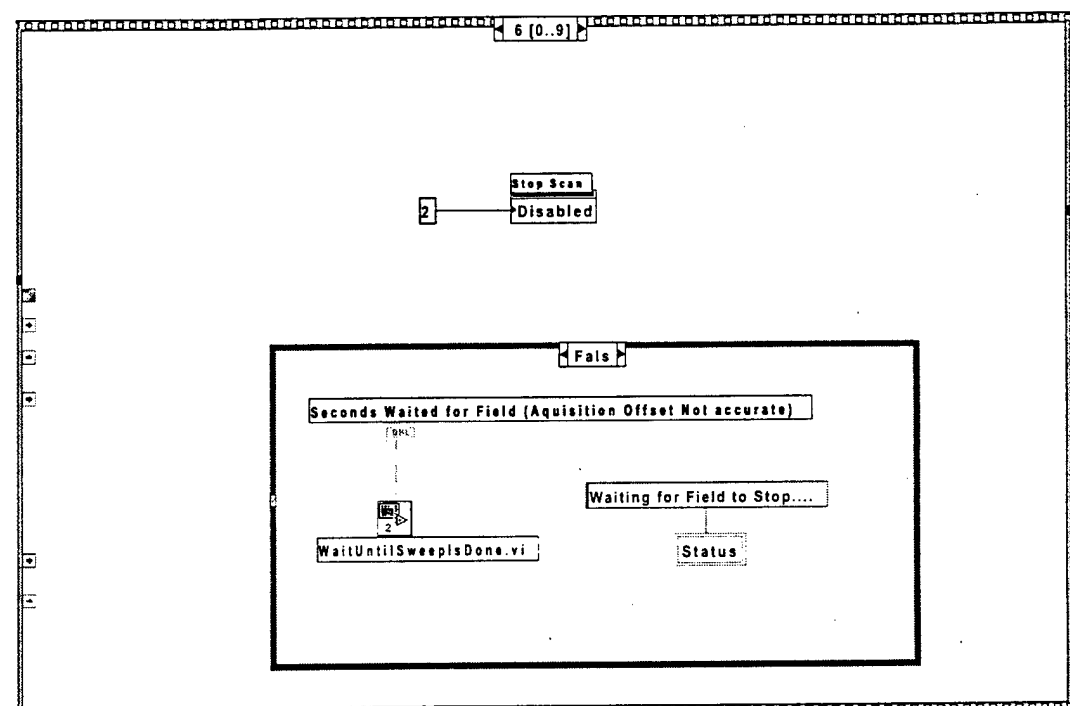
# epr program version 1.5.5.vi

1

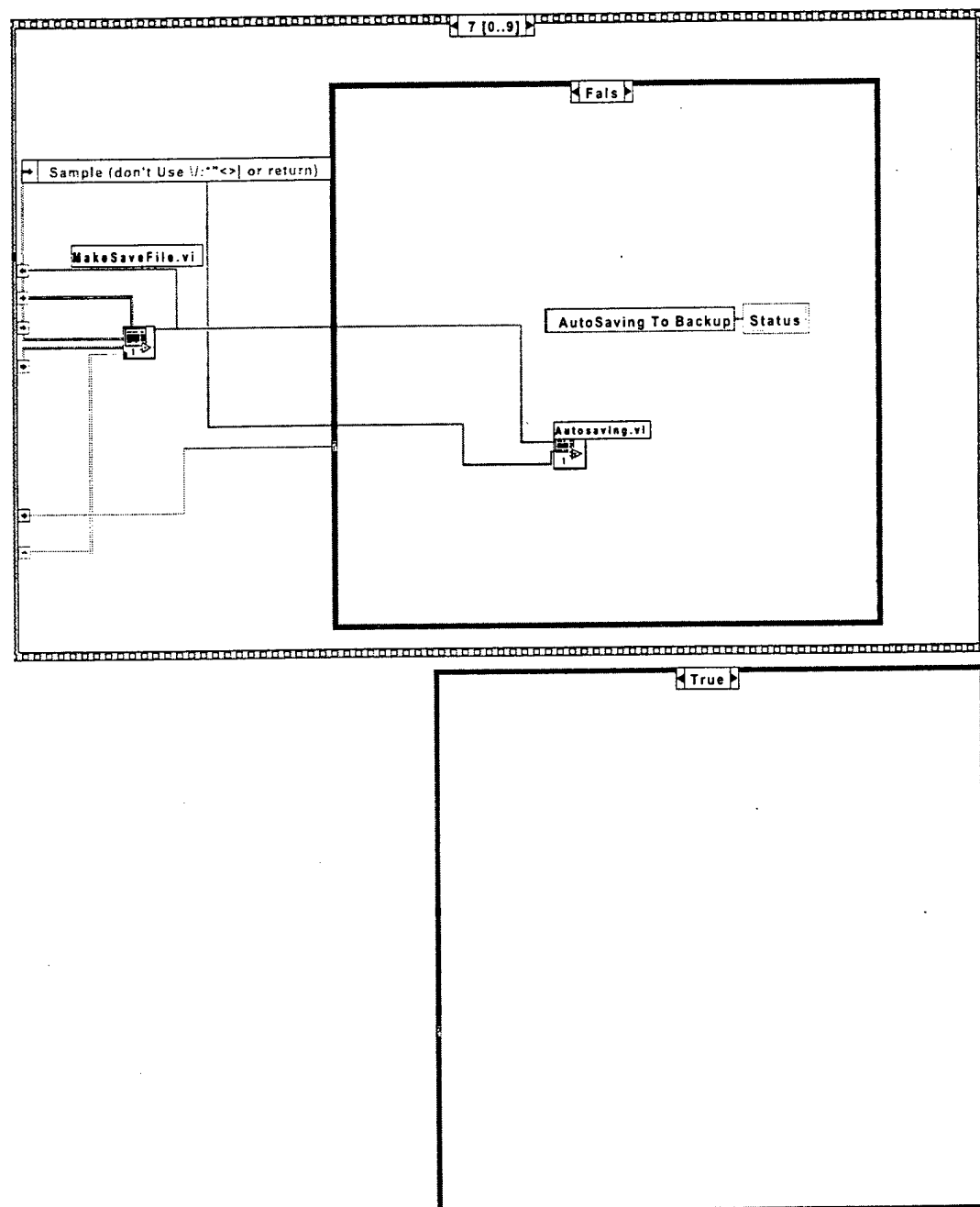


epr program version 1.5.5.vi

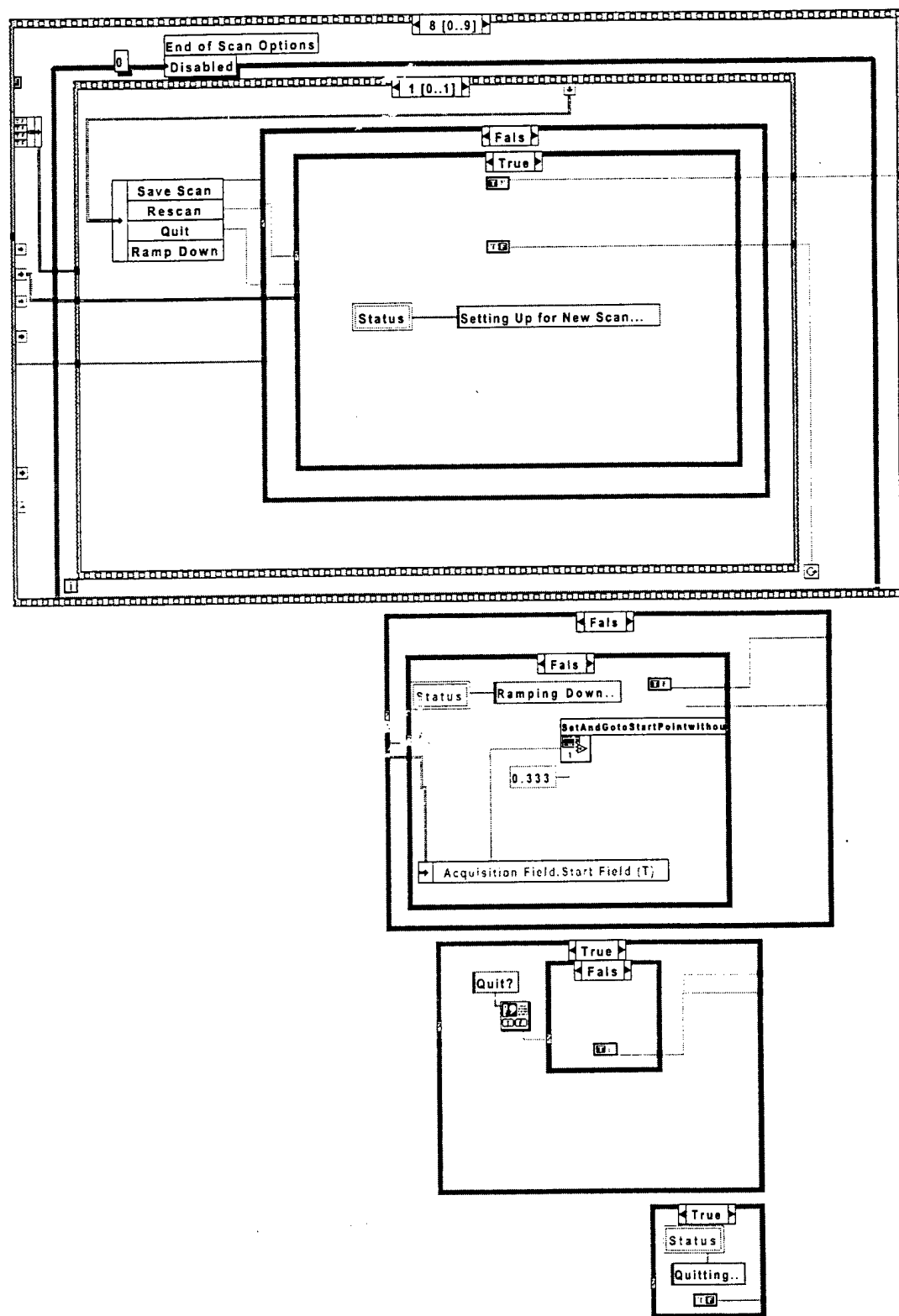
1



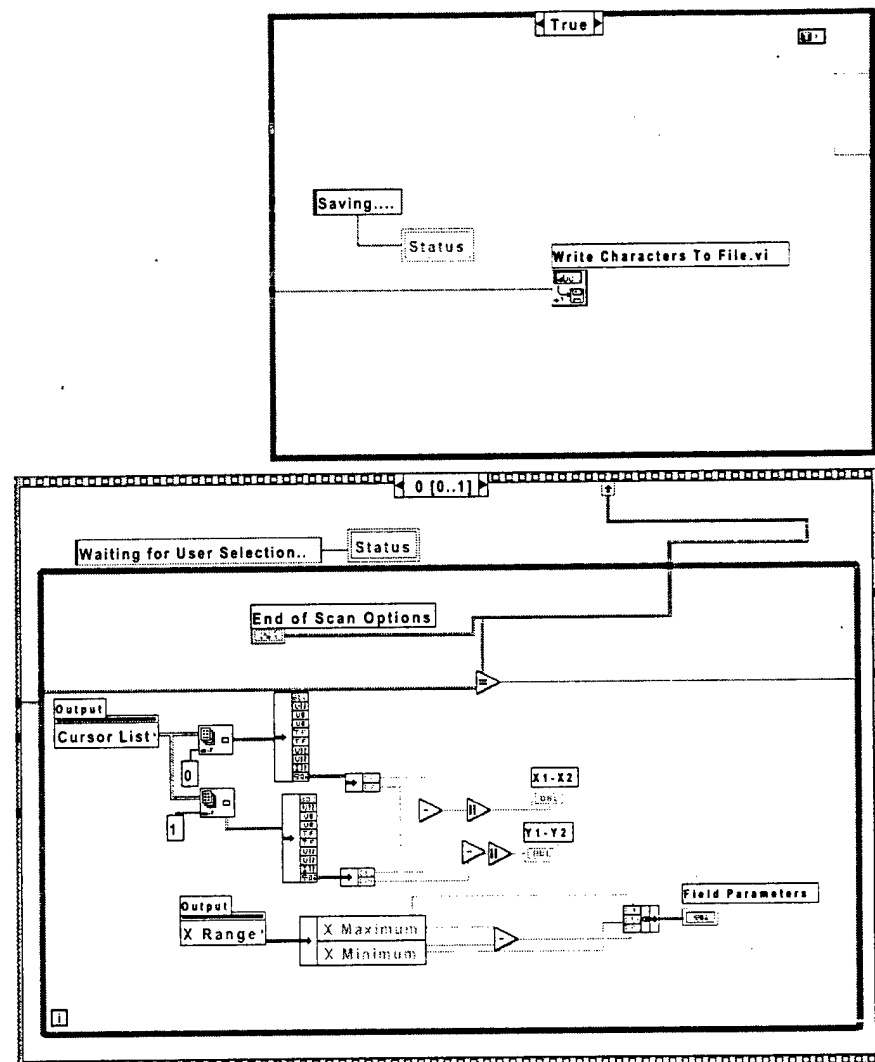
## epr program version 1.5.5.vi



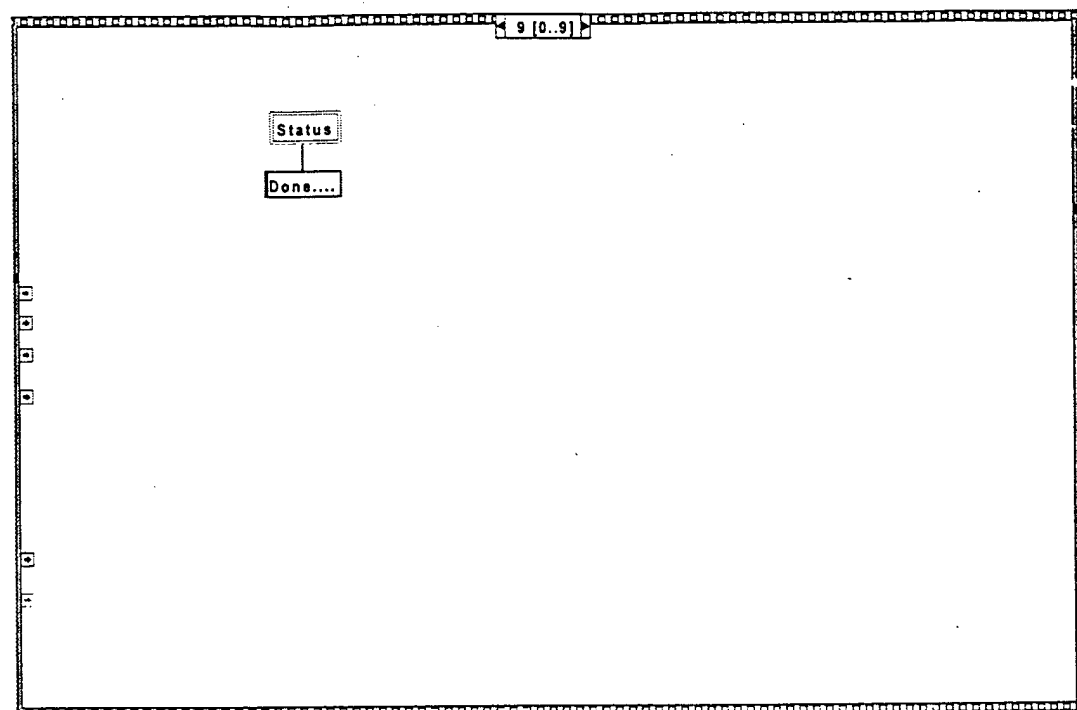
# epr program version 1.5.5.vi



## epr program version 1.5.5.vi



**epr program version 1.5.5.vi**



### Appendix III

#### A Search for High-Spin Zeeman Effects in the 94.9 GHz EPR spectrum of Cr<sup>3+</sup> in $\alpha$ -Al<sub>2</sub>O<sub>3</sub>

## 94.9 GHz EPR Study of Cr<sup>3+</sup> in $\alpha$ -Al<sub>2</sub>O<sub>3</sub>

D. A. Schwartz, E. D. Walter and D. J. Singel

### Abstract

We present results of a high-frequency (94.9 GHz) continuous wave (CW) room-temperature electron paramagnetic resonance (EPR) study of Cr<sup>3+</sup> (S=3/2) in a small neutron-irradiated and thermally annealed single crystal of  $\alpha$ -Al<sub>2</sub>O<sub>3</sub> (sapphire) grown by the laser heated pedestal method. Through analysis of the angular variation patterns of the three nominally allowed electronic spin transitions of Cr<sup>3+</sup>, we have measured spin-Hamiltonian parameters ( $g_{\perp} = 1.9812$ ,  $g_{\parallel} = 1.9820$ ,  $|D| = 5.737$  GHz) and have considered the potential impact of high-spin Zeeman terms (terms of the form  $BS^3$ ) on the outcome of spin-Hamiltonian parameter assessment. Our results indicate the marginal relevance of higher order terms to the satisfactory analysis of the observed angular variation patterns and ultimately, to the assessment of the point symmetry of Cr<sup>3+</sup> in sapphire.

### Introduction

Previously we reported the observation, via EPR spectroscopy at 94.9 GHz, of a number of paramagnetic centers in a single-crystal fiber of sapphire ( $\alpha$ -Al<sub>2</sub>O<sub>3</sub>) that had been treated by neutron-irradiation followed by thermal annealing. In addition to EPR signals attributable to radiation-induced defects (color-centers), we also observed resonances from Cr<sup>3+</sup> and Fe<sup>3+</sup> ions. The identity of the ions was established by comparing values of spin-Hamiltonian (SH) parameters that we estimated from the 94.9 GHz EPR spectra with values previously reported in the literature.

We noted previously that the EPR literature on Cr<sup>3+</sup> in sapphire, while extensive, is not completely consistent. We detail previous measurements of sapphire:Cr<sup>3+</sup> spin-Hamiltonian parameters in Table 1. Manenkov and Prokhorov [1, 2] originally reported the room temperature SH parameter values  $g_{\parallel} = 1.984$ ,  $g_{\perp} = 1.9867$ , and  $|D| = 5.732$  GHz on the basis of work at 8.96 and 11.97 GHz. Subsequent work at 37.86 GHz by Zverev and Prokhorov [3, 4] yielded (presumably also at room-temperature)  $g_{\parallel} = 1.982$ ,  $g_{\perp} = 1.979$  and  $D = -5.732$  GHz, while

Geusic [5], working at 9.309 and 11.593 GHz and room temperature, reported  $g_{\parallel} = 2.003$ ,  $g_{\perp} = 2.00$ , and  $D = 5.786$  GHz, and Zaripov and Shamonin, working at 9.58 GHz, reported  $g_{\parallel} \approx g_{\perp} = 1.98$  and  $|D| = 5.70$  GHz [6, 7], also at room temperature. In later work, several other groups [8, 9] determined SH parameter values that were more like the values Manenkov and Prokhorov initially reported in 1955. Still others [10], [11] cited the values reported by Manenkov and Prokhorov.

Klein and co-workers [9] detailed the effect of temperature on the EPR parameters of  $\text{Cr}^{3+}$  in ruby. They state that within the accuracy of their measurements there was no temperature dependence of the g-values, however, their Figure 2 seems to show otherwise and the data therein may support an alternate explanation of the temperature-dependence of the g-values. They observed  $|D|$ , however, to increase from 5.726 GHz to 5.816 GHz over the temperature range 88 K to 575 K. Thus, the variations in the D values reported previously might be taken to indicate variations in the experimental temperatures of the above studies. These results, however, suggest that variation in observed  $|D|$  values due to possible temperature variation ( $\sim 0.24$  MHz/K near RT) cannot completely explain the range of previously reported D values. The variety of previously reported g-values, too, cannot be explained on the basis of this variable temperature study.

The lack of consistency in these reported g-values may, of course, simply reflect limitations present on the quantitative analysis of complex EPR spectra at the time of the early studies. A detailed study, with extensive numerical analysis, was reported in 1978 by Chang, *et al.*, [12] who found:  $g_{\parallel} = 1.9817$  and  $g_{\perp} = 1.9819$ , and  $D = -5.746$  GHz.

A consistent feature of all previous EPR studies of sapphire:Cr<sup>3+</sup> is the use of a “conventional” spin-Hamiltonian (CSH) for summarizing the experimental results. This CSH, an effective Hamiltonian operating on the ground state crystal field manifold, derives from a perturbation treatment of the spin-orbit coupling and electronic Zeeman interaction within the zero-order crystal field states [13], and contains only three parameters,  $g_{\parallel}$ ,  $g_{\perp}$ ,  $D$ . It does not contain the HSZ (“high-spin Zeeman”) terms – terms linear in applied magnetic field and tri-linear in spin operators – that are included for S=3/2 centers in the GSH (“generalized” spin Hamiltonian) treatments presented by numerous authors (see, *e.g.*, Roitsin [14], McGavin, *et*

*al.*[15] and references cited *in loc.*). While HSZ terms are often dismissed *a priori* as negligible, Geusic, specifically called attention to their possible importance in his 1956 study of the EPR of Cr<sup>3+</sup> in sapphire[5].

As operating frequencies are increased, the HSZ interactions could gain in significance relative to the field-independent fine structure interaction. The capacity to measure such interactions could be an important singular achievement of the emerging field of “high-frequency” ( $\geq 100$  GHz) EPR spectroscopy (see, e.g., Buckmaster *et al.*[16]). One benefit of such measurements relates to the ability of SH terms supralinear in spin operators to reflect the point group of the paramagnetic ion, as discussed in detail by Roitsin[14] and by Grachëv[17].

In the conventional approach the 32 crystallographic point groups subdivide into three categories, characterized by isotropic, axial, and rhombic tensorial interactions. The applicable GSH's, however, subdivide in as many as eleven distinct symmetry categories, or “aggregates”[14]. Thus, for example, systems of C<sub>3</sub>, C<sub>3v</sub>, and C<sub>3h</sub> symmetries possess distinct spin-Hamiltonians; if the distinguishing terms in the SH are of sufficient magnitude, such systems could be distinguished by magnetic resonance spectroscopy. Such discriminating power would be of great value, particularly for any variation from idealized uniaxial symmetry in the environments of paramagnetic centers, *e.g.*, in bioinorganic complexes.

With the goals of precisely characterizing the angular dependence of the EPR of Cr<sup>3+</sup> in sapphire, and of assessing the significance of the HSZ interactions at high field in this system, we have carried out a study of the orientation dependence of the room-temperature EPR spectra of sapphire:Cr<sup>3+</sup> at 94.9 GHz. We have measured Zeeman ( $g_{\parallel}$ ,  $g_{\perp}$ ) parameters and the fine structure parameter ( $|D|$ ) from the angular variations of resonance fields under the assumption of uniaxial symmetry. We have also analyzed the observed orientation dependence of resonance fields for possible HSZ effects consistent with various point symmetries possible in this system. In light of the present results, we summarize some prerequisites for successful observation of HSZ effects.

## Theory

The CSH for an S=3/2 center located at a site of axial symmetry in a crystal can be expressed as:

$$\mathcal{H} = + |\mu_B| |\mathbf{B}_0| \{ g_{\parallel} \cos\Theta S_z + g_{\perp} \sin\Theta S_x \} + D S_z^2; \quad S = 3/2, \quad (1)$$

in which  $\mu_B$  is the Bohr magneton,  $\mathbf{B}_0$  is the applied magnetic field, and  $g_{\parallel}$ ,  $g_{\perp}$  and  $D$  are parameters that gauge the Zeeman ( $g_{\parallel}$ ,  $g_{\perp}$ ) and fine structure ( $D$ ) interactions. In the axis system implied by equation (1)  $z$  is the unique symmetry axis in the crystal, and  $\Theta$  is the angle between  $\mathbf{B}_0$  and the  $z$  axis. For paramagnetic centers with lower than axial symmetry, the Zeeman portion of the spin hamiltonian is parameterized by  $g_{xx}$ ,  $g_{yy}$ , and  $g_{zz}$ , and the fine structure interaction is commonly parameterized by  $D = 3D_{zz}/2$  and  $E = (D_{xx} - D_{yy})/2$  to give

$$\begin{aligned} \mathcal{H} = & + |\mu_B| |\mathbf{B}_0| \{ g_{zz} \cos\Theta S_z + g_{yy} \sin\Theta \sin\phi S_y + g_{xx} \sin\Theta \cos\phi S_x \} \\ & + D S_z^2 + E (S_x^2 - S_y^2) \end{aligned} \quad (2)$$

where  $\phi$  is the angular displacement of  $\mathbf{B}_0$  from the  $x$  axis about the  $z$  axis, and the cartesian axes correspond to the principal axes of the Zeeman and fine structure terms.

Several authors have presented schemes for constructing more general SH's (e.g., refs 3a, 4-6 of Roitsin[14], refs 1-16 of Grachëv[17], refs 4 and 5 of McGavin, *et al.*[15], Geschwind[18]. This development was initiated by Koster and Statz[19], and has been discussed in detail by Roitsin[14], Buckmaster, *et al.*[16, 20], Grachëv[17], and McGavin, *et al.*[15]. The GSH's presented by these authors are designed to contain all terms, for a given value of  $S$ , that are consistent with the symmetry properties of a crystallographic point, and thus can include additional terms not present in the CSH (eq. (1)).

For an  $S=3/2$  system, the additional terms,  $\mathcal{H}_{BS^3}$  -- which are linear in  $\mathbf{B}_0$  and tri-linear in  $\mathbf{S}$  [21, 22] -- are illustrated most lucidly in the formulation of Roitsin[14]:

$$\mathcal{H}_{BS^3} = \sum_{x,y,z} (\mathbf{B}_0)_i \left( \sum_{m=0}^3 B_{3i}^m O_3^m + \sum_{m=1}^3 C_{3i}^m \Omega_3^m \right) \quad (3)$$

in which:  $(B_o)_i$  is a Cartesian component of the applied magnetic field,  $B_{3i}^m$  and  $C_{3i}^m$  gauge the SH terms, and  $O_n^m$  and  $\Omega_n^m$  are tri-linear spin operators expressed in irreducible tensorial form (tabulated in Appendix V of Alt'shuler and Kozirev[23]). As expressed in equation (3),  $\mathcal{H}_{BS^3}$  contains 21 adjustable parameters.

A reconstruction of the GSH has been given by Grachev[17] (see also Alt'shuler and Kozirev [23], pp.85ff, and Grant and Strandberg[24]). This proceeded by coupling the field and spin vector operators, decomposing the products according to irreducible tensorial forms and creating tesseral linear combinations of these tensor operators [25, 26].

McGavin, *et al.*, following this approach, give the following terms for addition to the CSH of equation (1):

$$\mathcal{H}_{HSZ} = g_e |\mu_B| B_0 \left[ \sum_{m=-2}^2 B_{2,m} U_{2,m} + \sum_{m=-4}^4 B_{4,m} U_{4,m} \right] \quad (4)$$

The  $B_{l,m}$  parameters in  $\mathcal{H}_{HSZ}$  are unitless variables indicating the size of the interaction and the  $U$ 's are operators that are products of  $H_x$ ,  $H_y$ ,  $H_z$ ,  $S_x$ ,  $S_y$ , and  $S_z$ , as detailed in McGavin, *et al.*[15]. We have dropped superscripts for  $B$ 's since we are only considering terms of the form  $BS^3$  (*i.e.*, our terms  $B_{n,m}$  and  $B_{n,m}$  above are analogous to symbols  $B_{2,m}^{1,3}$  and  $B_{4,m}^{1,3}$  of McGavin, *et al.*[15], eq. 23).

An important advantage of this approach to reconstructing the GSH is that it effects the removal of certain redundant parameters from the SH of Roitsin[17]. The number of terms  $BS^3$  is reduced from 21 in equation (3) to 14 in equation (4). Finally, as pointed out by Grachëv, these terms constitute an orthogonal set.

The number of terms in this  $\mathcal{H}_{HSZ}$  can be further reduced by point symmetry constraints. Each term in the SH applicable to a paramagnetic center must transform as the identical (totally symmetric) representation of the point group of the center. To illustrate this adaptation in some generality we consider  $C_3$  and all other trigonal groups, as well as the hexagonal groups with a three-fold major proper rotation axis. In doing so, we aim to characterize what is offered by including these terms.

To induce irreducible representations of point groups upon the SH terms in (4) we take advantage of the fact that they transform like the tesseral and sectoral harmonic functions. We therefore simply test for invariance of the tesseral and sectoral harmonic functions with respect to the operations of a point group. The test proceeds by considering the point group symmetry operations  $\mathfrak{R}$ . These map a general point  $P$  in Cartesian space, with coordinates  $(x, y, z)$ , to the point  $P'$  with coordinates  $(x', y', z')$ . Consider a function,  $f$  (exemplified by a tesseral or sectoral harmonic function) which is expressed as  $f(x, y, z)$ . We construct operators-on-functions,  $O_{\mathfrak{R}}$ , corresponding to each of the point group symmetry operations  $\mathfrak{R}$  such that  $O_{\mathfrak{R}}f = f'$ , where  $f'$  is a new function that assigns to a general point  $P'$  the same value as the function  $f$  assigns to  $P$  (see Schonland[27], ch. 4). If  $O_{\mathfrak{R}}f = f$  in general, for all  $\mathfrak{R}$  in a point group, then  $f$  transforms according to the identical representation of that point group. A spherical tensor operator analogous to the function  $f$  (analogous in the sense of operator equivalence to the symmetry adapted Cartesian function) then belongs to the spin-Hamiltonian appropriate to the point group whose operations  $\mathfrak{R}$  were considered.

The GSH for  $S=3/2$  systems becomes

$$\mathcal{H} = \mathcal{H}_c + \mathcal{H}_{HSZ} \quad (5)$$

where  $\mathcal{H}_c$  is the CSH appearing equation (1). The high-order terms of equation (4) which survive the  $C_3$  symmetry operations are

$$\mathcal{H}_{HSZ}(C_3) = +g_e |\mu_B| B_0 (B_{2,0}U_{2,0} + B_{4,0}U_{4,0} + B_{4,3}U_{4,3} + B_{4,-3}U_{4,-3}) \quad (6)$$

where  $g_e$  is the free electron  $g$  value.

Table 2 shows the allowed terms from equation (4) for the several point groups we are considering. This tabulation illustrates the great advantage of this derivation of the SH: it allows distinctions between point groups that might otherwise be lumped into the "axial" set by analysis employing only the CSH of equation (1).

### Materials and Instrumentation

The single crystal of  $\alpha$ -Al<sub>2</sub>O<sub>3</sub> studied in the present work was fabricated in the laboratory of Professor William Yen (University of Georgia) by the laser-heated pedestal-growth method from materials of 99.999% purity[28]. This sample was neutron irradiated, and then thermally

annealed at ~600K by Professor Ilmo Sildos (University of Tartu, Estonia). We obtained this crystal – a right circular cylinder of ~0.5 mm diameter – from Professor Alexander Rebane of the Montana State University Department of Physics. This crystal was found to contain detectable amounts of  $\text{Cr}^{3+}$  and  $\text{Fe}^{3+}$  by EPR spectroscopy at 94.9 GHz[29]. Our instrumentation, described in more detail elsewhere[29], includes a 94.9 GHz microwave bridge and cavity obtained from the Physico-Technical Institute of Donetsk, Ukraine and a sweepable Oxford Teslatron superconducting magnet. The cavity apparatus provides for full rotation of the sample about the cavity axis, and in our instrument this axis may be oriented perpendicular to the applied static magnetic field ( $\mathbf{B}_0$ ).

### Experiments and Results

CW EPR spectra were obtained at 94.9 GHz as a function of the crystal's orientation in the applied magnetic field  $\mathbf{B}_0$ . Measured resonance fields due to  $\text{Cr}^{3+}$  are shown in Figure 1 for data obtained from a plane containing the  $z$  axis. The sample was positioned for rotation by the standard method: it was placed in the magnetic field with its cylinder axis (nominally the crystallographic  $b$  axis) approximately perpendicular to the applied magnetic field and nominally parallel to the rotation axis. The sample was then oriented further by rotation about the cylinder axis and another axis perpendicular to  $\mathbf{B}_0$  until the smallest value of a resonance field  $B_{\text{res}}$  was observed for any of the strong high-field  $\text{Cr}^{3+}$  transitions of this sample (*c.f.* Schwartz, *et al.*[29]). As a point of departure, rotation of the sample proceeded from this point about the cylinder axis with EPR spectra and resonance fields for the three high-field  $S=3/2$  transitions being obtained at intervals of  $\Delta\theta=0.04\pi$  ( $=8^\circ$ ) or less. This rotation corresponds (nominally) to a rotation of  $\mathbf{B}_0$  in the crystal's  $xz$  plane where  $\theta=0$  corresponds (nominally) to  $\mathbf{B}_0 \parallel c$  axis. Resonance fields were also measured from other orientations, out of the  $xz$  plane by adjustment of the microwave coupling adjustment (which effects sample rotation about another axis  $\perp \mathbf{B}_0$ ). Substantial misadjustment of microwave coupling did not interfere with the unambiguous observation of the strong  $\text{Cr}^{3+}$  resonances in this sample.

SH parameter optimizations based on observed AVP's (angular variation patterns) of resonance fields were conducted using the EPR-NMR magnetic resonance simulation and analysis software package[30]. This software provides for exact diagonalization of a large

variety of SH's applicable to electron and nuclear magnetic resonances. Hamiltonians amenable to analysis with this program include general SH's applicable to S=3/2 systems (e.g. eq. (5)).

### Analysis and Discussion

Analysis of observed resonance field AVP's commenced by fitting the parameters of the SH of eq. (1) to resonance field data in Figure 1. The results of this and all other parameter optimizations were produced with the computer program EPR-NMR and are tabulated in Table 3. With linewidths ranging from 10-40 Gauss, the size of the root mean square deviation (RMSD) between calculated and observed resonance fields for this initial analysis (24.86 G) is not unexpected. Nevertheless, we are interested in the possibility that BS<sup>3</sup> effects are discernible in the observed resonance fields even though these effects may be very small[16]. Accordingly, we shall explore several explanations for the deviations between calculated and observed resonance fields for this initial parameter determination. The deviations, if properly accounted for, may allow HSZ effects in sapphire:Cr<sup>3+</sup> to be quantified. Contributions to the RMSD between observed resonance fields and those calculated from the CSH include: 1) effects on the positions of resonance fields (including, but not limited to effects on the angular positions of the extrema of the resonance field tracks) due to HSZ effects; 2) improper positioning of the sample in the magnetic field such that sample rotation was carried out with some systematic error in the determination of the angular sample position; 3) some combination of 1) and 2); and 4) non-systematic errors in the determination of sample angular positions.

We now consider the impact of various  $B_{n,m}U_{n,m}$  terms on the quality of the SH parameter fits to uncorrected resonance fields. In the presence of unmistakable HSZ effects, we expect to see one of the sets of parameters shown in Table 2 emerging with unambiguously non-zero values from fits of the resonance field data. In Table 3 we summarize the impact of various  $B_{n,m}U_{n,m}$  term combinations on the parameter determination; these parameter optimizations employed SH's encompassed by equation (5) and term combinations suggested by Table 2. It is clear from these results that HSZ terms do not significantly improve the quality of the SH parameter fit; a small reduction in RMSD between observed and calculated resonance fields is to be expected from the addition of any extra term to the SH. The table shows that the only term with even marginal significance to the fits is the  $B_{4,3}U_{4,3}$  term (its error being the only one smaller than the respective fitted parameter value).

We show in Figure 2 the differences, calculated for both W- and X-band at intervals over a hemisphere ( $0 \leq \theta \leq \pi$ ,  $0 \leq \phi \leq \pi$ ), between the resonance fields of the  $3 \leftrightarrow 4$  AVP computed with the ( $\phi$ -independent) CSH and the corresponding resonance fields computed with a ( $\phi$ -dependent) SH containing the HSZ term  $B_{4,3}U_{4,3}$ . The plots in Figure 2 (a) exemplify the differences computed for the other five  $\text{Cr}^{3+}$  EPR transitions while the X-band differences (Figure 2 (b)) are smaller by a factor of  $\sim 10$  and exhibit varying overall shapes. The difference map computed with the  $B_{4,-3}U_{4,-3}$  term is related to that shown for  $B_{4,3}U_{4,3}$  by a shift of  $\pi/6$  along the  $\phi$  coordinate at both fields. What may be seen in Figure 2 (a) and Figure 3 is that a contribution from a term  $B_{4,3}U_{4,3}$  (with  $B_{4,3} = 0.0005$ ) creates deviations in a transition's AVP of at most  $\pm 20$  G relative to the CSH AVP; this deviation is of the order of the RMSD's for SH parameter fits we have calculated so far. Furthermore, in consideration of Figure 3 (b) (especially, the flatness near  $\theta = 0, \pi$ ) and Figure 3 (a) (especially, the rate of change of  $H_{\text{res}}$  near  $\theta=0$ ), it is reasonably clear (at least for magnitudes of HSZ parameter values encountered so far in this analysis) that the protocol established above for placing  $\mathbf{B}_0$  parallel to the crystal  $c$  axis is appropriate for EPR spectroscopy of the sapphire:Cr<sup>3+</sup> system at this frequency. In fact, several calculations of GSH AVP's with several values of  $B_{4,-3} \leq 0.05$  show that  $\mathbf{B}_0 \parallel c$  always corresponds to at least a local extremum in the observed resonance field for the  $3 \leftrightarrow 4$  transition. It was precisely this concern, about the BS<sup>3</sup> effects on the position of Cr<sup>3+</sup> resonance field, which led us to initially describe the angles  $\theta$  and  $\phi$  as "nominal;" the angle assignments were based on an assignment of  $\theta=0$  which derived from the conventional z-axis alignment approach described above.

Regarding possible errors in the angular coordinates at which resonance fields were measured, a possible correction to the data in Figure 1 involves a systematic correction to the value of  $\theta$ , where it is assumed that the magnetic field is positioned at  $\phi=0$  (the xz plane) for all measurements. The functional forms for an  $S=3/2$  system's resonance field AVP's due to the sum of Zeeman and fine structure interactions, in the limit of high field (and in the limit of very small higher order effects) are known for  $\phi=0$ [31]. A  $\theta$  correction may be achieved by a separate least-squares fit of the data for each transition's AVP with an adjustable parameter,  $\delta\theta$ , corresponding to a required correction to the "nominal"  $\theta$  angles. Analysis of the five "high field" AVP's of Figure 1 in this way yielded  $\delta\theta$  corrections of  $0.00093\pi$ ,  $-0.00056\pi$ ,  $0.0017\pi$ ,

0.00095 $\pi$ , and 0.0025 $\pi$  (0.17, -0.10, 0.31, 0.17, 0.45 degrees) respectively, and a new angle,  $\Theta=\theta+\delta\theta$ , is defined for each resonance field. SH parameter determination of the  $\Theta$ -adjusted AVP's based on equation (1) yielded CSH parameters similar to those of the previous analysis, but the quality of the fit improved substantially (RMSD = 17.54 G, see Table 3).

It is of interest to consider the deviations of resonance fields for two calculated 3 $\leftrightarrow$ 4 AVP's which differ only in the value of  $\theta$  assigned to each resonance field ( $\delta\theta = 0.3$ ). The differences between these two sets of computed resonance fields as a function of  $\theta$  models the deviations one would observe between a resonance field data set exhibiting systematic error in assigning  $\theta$  to resonance field measurements and a calculation. This is shown in Figure 4. We note that this pattern of deviation bears some qualitative and quantitative similarity to the deviation in calculated resonance fields produced by including the  $B_{4,3}U_{4,3}$  HSZ term ( $B_{4,3}=0.0005$ ) in the SH (relative to a calculation employing only the CSH). The latter deviation is shown in Figure 3 (b). Comparison of the qualitative features of these deviations indicates that there may be some "crosstalk" between an error in assigning  $\theta$  and the effect of the  $B_{4,3}$  HSZ interaction on resonance fields measured in the xz plane. Examination of Table 3, however, demonstrates that  $\theta$  corrections did not appreciably change the fitted size of HSZ effects in the resonance fields. The HSZ terms still contribute negligibly to the quality of SH parameter determination as evidenced by the minimal reduction in the RMSD between observed and calculated resonance fields as HSZ terms were added to the analysis of  $\theta$ -corrected data.

Further angle corrections may be of interest because we generally observed slight resonance field differences in pairs of resonance field measurements that differ only by a nominal  $\pi$  rotation of the crystal. One of our 3 $\leftrightarrow$ 4 AVP's is exemplary of this phenomenon:  $B_{\text{res}}(\theta=0, \phi=0) = 3.0084$  T,  $B_{\text{res}}(\pi, 0) = 3.0092$  T. We conclude from this that rotation of the  $B_0$  field did not occur strictly in the xz plane, *i.e.*, that the crystal *b* axis (*y* direction) was not parallel to the effective sample rotation axis. Therefore some (additional) correction to the nominal angle assignments may be appropriate. Small angle corrections addressing this problem may be computed by noting that the resonance fields of the outer AVP's are proportional to  $\cos^2(\theta)$  for  $\theta$  values near 0 and  $\pi$  (in the limit of very small higher order interactions):

$$B_{\text{res}}(\theta) = A + B\cos^2(\theta) \quad (7)$$

The  $\theta=0,\pi$  resonance fields may be used, in conjunction with a  $\cos^2(\theta)$  fit of the whole  $3\leftrightarrow 4$  AVP, to compute an apparent  $\theta$  for a  $\pi$  rotation about the effective rotation axis (the actual value of  $\theta$  and the rotation angle,  $\pi$ , are different because the rotation axis is not exactly parallel to the crystal  $b$  axis). By assuming that resonance fields near the  $yz$  plane vary as  $\cos^2(\theta)$ , we have:

$$B_{\text{res}}(0 \text{ rotation}) - B_{\text{res}}(\pi \text{ rotation}) = 0.0008 \text{ Tesla} = B(\cos^2(0) - \cos^2(\theta_\pi)) \quad (8)$$

where  $\theta_\pi$  is the angle  $\mathbf{B}_0$  makes with the  $z$ -axis after a  $\pi$  rotation about the effective rotation axis, and

$$\cos(\theta_\pi) = -|[(0.0008/B) + 1]^{1/2}| \quad (9)$$

where the value of  $B$  was obtained to a good approximation from the  $\cos^2(\theta)$  fit of the whole  $3\leftrightarrow 4$  AVP. Using the actual rotation angle ( $\pi$ ) and the effective  $\theta_\pi$  computed in this way we may employ a rotation matrix, which depends only on the effective rotation axis vector components (referred to the laboratory frame) and the actual angle of rotation about the effective axis, to compute two components of the rotation axis vector. We make the simplifying assumption that the rotation axis lies in the  $yz$  plane. With knowledge of the effective rotation axis we may discern the corrected values of  $\theta$  and  $\phi$  for resonance fields of each rotation position in the AVP. This angle correction – applied only to the one  $3\leftrightarrow 4$  AVP mentioned above as a supplement to the  $\theta + \delta\theta$  corrections mentioned above (applied previously to all AVP's) – improved the overall SH parameter fit, giving a RMSD of 16.00 G (see table Table 3).

We note that since this angle correction positions some data away from the  $xz$  plane (to which data were nominally assigned at first), the determination of the  $B_{4,-3}$  parameter value is now not accompanied by a large error. Its value (from the EPRNMR parameter optimization) increased dramatically as well. The values of the CSH parameters, however, were not appreciably changed, indicating their robustness *vis a vis* our data, the several HSZ scenarios considered, and this  $\theta$  and  $\phi$  angle correction employed. This robustness may be good evidence for the  $\phi$ -independence of the EPR spectra. If the spectra are  $\phi$ -independent, detectable HSZ effects associated with SH terms  $B_{4,\pm 3}U_{4,\pm 3}$  should be absent. Note that effects due to terms

$B_{2,0}U_{2,0}$  and  $B_{4,0}U_{4,0}$  are inherently  $\phi$ -independent and may therefore not be ruled out by such geometric considerations.

In addition to producing reasonable values of the CSH parameters, the analysis to this point serves to underscore the importance of including data that falls outside principal planes in the assessment of HSZ parameters. When data is not obtained outside of the principal planes, some dimensions of the SH parameter space are left unexplored due to the periodic zero crossings – some of which lie in principal planes – of the HSZ term contributions. Examples of such zero-crossings may be seen in Figure 2 (a). With the goal of gaining a more secure foundation on which to include or neglect HSZ effects in the interpretation of the EPR of the sapphire:Cr<sup>3+</sup> system, we now consider some resonance field data collected outside of the xz plane.

With the present sample and sample-rotation apparatus, we are unable to effect full rotations of  $\mathbf{B}_0$  in planes far from the plane perpendicular to the fiber axis. Nevertheless, we can rotate  $\mathbf{B}_0$  away from this plane, by as much as  $\pm\pi/9$ , by means of the microwave coupling adjustment. These rotations are fruitful because the signals of interest are of more than adequate strength even when microwave coupling is suboptimal, and because a rotation of this extent does not substantially decrease the component of  $\mathbf{B}_1 \perp \mathbf{B}_0$ . Resonance fields were measured at various coupling adjustments (away from the position where  $\mathbf{B}_0$  is nominally perpendicular to the sample's long axis, *i.e.*, at positions where  $\mathbf{B}_0$  is nominally out of the xz plane) for many rotational positions of the sample about its long axis. For such measurements, the  $(\Theta, \phi)$  orientation of  $\mathbf{B}_0$  in the crystal may be calculated from the cumulative effects of rotations of the crystal about two axes in the laboratory reference frame: the sample's cylinder axis (oriented initially along the laboratory frame y-direction) and the coupling rotation axis (oriented along the laboratory frame x-axis). We measured resonance fields (as many as three of the “strong” Cr<sup>3+</sup> EPR transitions) at over 100 field positions in the crystal frame, and these positions are shown in Figure 5.

The results of spin-Hamiltonian parameter optimization on this set of 297 in- and out-of-plane resonance fields are listed in Table 3. An initial optimization was performed employing the CSH and no angle corrections, and the overall quality of the parameter optimization is indicated in the table (RMSD  $\approx 39.85$  for 297 data points). This optimization clearly represents an inferior parameter optimization *vis a vis* even the optimizations for angle-uncorrected in-plane

date reported in Table 3. This may indicate the need for resonance field orientation corrections. Further support for this hypothesis is indicated by the dramatic improvement achieved in a parameter fit minimization in which all elements of the  $\mathbf{g}$  and  $\mathbf{D}$  matrices were allowed to vary (RMSD = 22.39). Several orientation corrections to this data are now considered.

Parametric variation of  $\theta_a$  (the raw azimuthal angle, *i.e.*, the angle of rotation about the sample's cylinder from the point where  $\mathbf{B}_0 \parallel \mathbf{z}$ ) and  $\gamma$  (the raw coupling angle), the angles used to calculate  $\theta$  and  $\phi$  direction of  $\mathbf{B}_0$  in the crystal, reveal only small improvements to fits when new angles  $\Theta$  and  $\Phi$  are defined (derived from  $\theta_a \rightarrow \theta_a + \delta\theta_a + \varepsilon_\theta * \theta_a$  and  $\gamma \rightarrow \gamma + \delta\gamma + \varepsilon_\gamma * \gamma$ , where parameters were varied in these ranges:  $-1.0 \leq \delta\theta_a, \delta\gamma \leq +1.0$  and,  $-0.06 \leq \varepsilon_\theta, \varepsilon_\gamma \leq 0.06$ ). The angle corrections which produced both the minimum RMSD and the minimum rhombicity of the  $\mathbf{D}$  tensor (under optimization in which all  $\mathbf{D}$  matrix elements are allowed to vary) are:  $\delta\theta_a = 0.75$ ,  $\delta\gamma = 0.0$ ,  $\varepsilon_\theta = 0.0$ ,  $\varepsilon_\gamma = 0.03$ .

Our CSH parameter values are in good agreement with the values reported by Chang, *et al.*[12] We have noted that these values are stable when fits of HSZ terms are attempted and suggested that this may be due to the lack of significant HSZ effects in the resonance fields. The quantum mechanical perturbation treatment of electronic states shows that HSZ effects trilinear in electronic spin vector components are proportional to  $(\lambda/\Delta)^3$  (where  $\lambda$  is the spin orbit coupling constant for  $\text{Cr}^{3+}$  and  $\Delta$  is the crystal field splitting). In consideration of published literature in which HSZ effects are observed[32], and in consideration of the quantum mechanical origin of these terms, it is likely that paramagnetic ions with even marginally higher spin-orbit couplings ( $\lambda$ ) are better candidates than  $\text{Cr}^{3+}$  for observation of HSZ effects.

We have alluded to previous measurements of HSZ effects[32] and wish to further comment on the relative success these authors enjoyed. The sapphire: $\text{Cr}^{3+}$  system possesses electronic quadrupole splitting which is evidenced by the substantial variation of the resonance fields of the outer ( $3/2 \leftrightarrow 1/2$ ,  $-1/2 \leftrightarrow -3/2$ ) transitions as a function of crystal orientation in the magnetic field. But we have also noted some similarity between the errors in the AVP's that are produced by angular misalignment and the computed effects in the AVP's due to addition of certain HSZ terms. The work on Co shows that, with  $D=0$  (rigorously), the HSZ effect appears on an otherwise stationary  $B_{\text{res}}$  background and is thus easily discernible without consideration of small angular location errors. On the other hand, the determination of small HSZ effects from

the  $\text{Cr}^{3+}$  system appears to require forbidding angular precision given the large variation, due to the fine structure interaction, of resonance fields with angle.

The relationship between the values of the readily observed EPR parameters ( $g_{\parallel}$ ,  $g_{\perp}$ ,  $D$ ) and the arrangement of the electronic states of  $\text{Cr}^{3+}$  in  $\alpha\text{-Al}_2\text{O}_3$  has been discussed thoroughly by Macfarlane[33-35] in the context of a crystal field model. It was already apparent from published experimental data that the “textbook” relationship ( $D = \lambda(g_{\parallel} - g_{\perp})$ ,  $\lambda$  = spin-orbit coupling parameter) was not applicable to  $\text{Cr}^{3+}$  in sapphire. It was with Macfarlane’s work and that of Sugano and Tanabe[36] that the complexity of the quantum mechanical relationship between  $D$  and the  $g$ -values began to be rationalized. This complexity arises from the fact that the second-order contributions that lead to the textbook expression vanish in sapphire:  $\text{Cr}^{3+}$ , so that only in higher order calculations are the origin of and relationship between  $D$  and  $g$ -values revealed. Exact calculations of  $D$  and  $g$  are extremely difficult; the theoretical derivations provided in the work of Macfarlane show that  $D$  and  $g$  arise from numerous small high-order contributions. Even so, the optical spectrum provides  $\lambda$  and the Racah parameters  $B$ , and  $C$  so that decent approximations of the EPR parameters may be found. We note in this context that Rimmer and Johnston[37] identified small adjustments to the parameter values of Macfarlane’s model that allowed much improved agreement of the computations of EPR parameters with experimentally observed values.

In view of the complexity of the likely models of  $\text{Cr}^{3+}$  in a trigonal field, Macfarlane, commenting on the analysis of Tanabe and Sugano, pointed out the disagreeable nature of including, *ad hoc*, spin-orbit coupling anisotropy and multiple spin-orbit coupling parameters in the treatment of this system. Even so, Klein, *et al.*, introduced these phenomenological parameters and was able to rationalize the (probably incorrect)  $g$ -values of Manenkov and Prokhorov[1, 2]. We find, however, that if we attempt to analyze the degree of spin-orbit coupling anisotropy using Klein’s model (which posits spin-orbit coupling anisotropy) and our (better)  $g$ -values which exhibit small  $\Delta g$ , we calculate the spin-orbit anisotropy to be 0.5% (a factor of 32 smaller than the figure of Klein). In other words, our measurements of  $\Delta g$ , in agreement of those of several other groups, predict essentially isotropic spin-orbit coupling within the Klein model. Macfarlane’s simpler analysis is therefore to be preferred as it finds the

correct g-anisotropy. This position is further sustained if we consider this model in light of the better EPR parameter values, *e.g.*, those of Chang, *et al.*[12] or those of the present work

### Conclusion

We have presented the results of a study of the orientation dependence of 94.9 GHz Cr<sup>3+</sup> EPR spectra in a single-crystal of neutron-irradiated white sapphire. We discussed the results of previous EPR studies of this system, and the heretofore universal application of the CSH to the interpretation of these results. We examined a key weakness of the CSH, the absence of HSZ terms which are in principle relevant on group theoretical grounds to the study of S = 3/2 systems. The prospects for the high-field EPR determination of the size of HSZ effects in the sapphire:Cr<sup>3+</sup> system were analyzed, and we discussed the significant benefit that positive identification of such effects would entail, namely, the more complete elucidation of the point symmetry of the paramagnetic ion in the crystal. This investigation revealed no conclusive evidence of HSZ effects; in light of this result, we discussed possible alterations and improvements of experimental conditions that may facilitate the identification of HSZ effects, namely, improvement of angular measurements and the use of measurements out of the xz plane. We believe that unambiguous measurements of HSZ effects, if fruitful, would constitute a significant achievement for high-field EPR spectroscopy. The ability to measure HSZ effects could have much to offer in the analysis of chemical structure problems from biology to material science.

### Acknowledgements

We wish to acknowledge helpful discussions with Professors John A. Weil (University of Saskatchewan, Saskatoon, SK) and Michael J. Mombourquette (Queens University, Kingston, ON).

## Figure Captions

Figure 1 Angular variation of the three "high field" 94.9 GHz EPR resonance fields of  $\text{Cr}^{3+}$  in nominally pure neutron-irradiated thermally annealed  $\alpha\text{-Al}_2\text{O}_3$  (sapphire) single crystal. Rotation occurred (nominally) about the crystal  $b$  axis ( $\phi=0$ ); at  $\theta=0$ ,  $B_{\text{ext}}$  is parallel to the crystal  $c$  axis. The five tracks include three for the  $3\leftrightarrow 4$  transition ( $\circ, \square, \diamond$ , lowest  $B_{\text{res}}$  at  $\theta=0$ ), and one each for the  $2\leftrightarrow 3$  transition ( $\triangle$ , intermediate  $B_{\text{res}}$  at  $\theta=0$ ) and the  $1\leftrightarrow 2$  transition ( $\nabla$ , lowest  $B_{\text{res}}$  at  $\theta=\pi/2$ ).

Figure 2 Calculated angular variation (a) at W-band (94.9 GHz) and (b) at X-band (9.49 GHz) of the contribution of the  $B_{4,3}U_{4,3}$  SH term to the resonance field of the  $3\leftrightarrow 4$  transition of an  $S=3/2$  system with SH parameters  $g_{\perp} = 1.9814$ ,  $g_{\parallel} = 1.9810$ ,  $D = -5.7413$  GHz,  $B_{4,3} = 0.0005$  (dimensionless[15]).

Figure 3 The calculated angular variation pattern of the  $3\leftrightarrow 4$  transition resonance fields ( $0 \leq \Theta \leq \pi, \phi=0$ ) of (a) the CSH; (b) the slice of the difference plot of Figure 2 (a) for  $\phi = 0$ ; (c) the slice of the difference plot of Figure 2 (a) ( $\Theta = 2\pi/3, 0 \leq \phi \leq \pi$ ). Figures (b) and (c) show the maximum possible contributions of the  $B_{4,3}U_{4,3}$  term to the ( $\phi$ -independent)  $B_{\text{res}}$  surface exemplified by the ( $\phi=0$ ) slice (a).

Figure 4 The difference between two  $3\leftrightarrow 4$  CSH AVP's computed with  $g_{\perp} = 1.9811$ ,  $g_{\parallel} = 1.9820$ ,  $D = -5.7413$  GHz. AVP's differ in that one is shifted along the  $\theta$  coordinate ( $\theta \rightarrow \theta + 0.00167\pi$ ). The plot indicates the effect of a systematic error in assigning  $\theta$  to sample positions and should be compared to Figure 3 (b).

Figure 5 The orientations, in the crystal's reference frame, of the applied magnetic field for 294 rotation/coupling variations.

## Tables

v (GHz)	g <sub>  </sub>	g <sub>⊥</sub>	D (GHz)	Reference
8.96, 11.97	1.984±0.0006	1.9867±0.0006	5.732*†	[1, 2]
37.86	1.982±0.002	1.979±0.009	-5.732±0.03	[3, 4]
9.309, 11.593	2.003±0.006	2.00±0.02	5.79±0.03	[5]
9.58	1.98*	1.98*	5.7*†	[6, 7]
9-18	~1.982*‡	~1.982*‡	5.74§	[9]
24.2	1.97*‡	1.97*‡	5.807*†	[38]
9.5, 24	1.9817±0.0004	1.9819±0.0006	-5.7465±0.002	[12]
94.9	1.9812xxx	1.9820xxx	5.737xxx	This work

Table 1 Room temperature EPR studies sapphire:Cr<sup>3+</sup>, with reported spectrometer frequency and spin hamiltonian parameter measurements.

- † value reported as absolute value
- \* no error reported
- ‡ only one g-value reported
- § value extracted from plot figure

Symmetry	$\mathcal{H} = \mathcal{H}_c$	$\mathcal{H} = \mathcal{H}_c$	$\mathcal{H} = \mathcal{H}_c$
Compliant	+B <sub>2,0</sub>	+B <sub>2,0</sub>	+B <sub>2,0</sub>
Spin	+B <sub>4,0</sub>	+B <sub>4,0</sub>	+B <sub>4,0</sub>
Hamiltonain		+B <sub>4,±3</sub>	+B <sub>4,+3</sub>
terms			+B <sub>4,-3</sub>
Point group symmetry	C <sub>3h</sub> D <sub>3h</sub>	C <sub>3v</sub> D <sub>3</sub> D <sub>3d</sub>	C <sub>3</sub> S <sub>6</sub>

Table 2 The SH terms from equation (10 - 4) which comply with the symmetry restrictions of several point groups.

Description of Hamiltonian	$g_1$	$g_{\perp} (g_{xx})$	$g_{yy}$	$ D  (\text{GHz})$	$\eta$	$B_{2,0}$	$B_{4,0}$	$B_{4,3}$	$B_{4,3}$	$\theta$ corr	$\phi$ corr	RMSD (G)	# resonance field measurements
CSH	1.98125 $\pm 0.00032$	1.98197 $\pm 0.00023$	-	5.733 $\pm 0.008$	0.0	-	-	-	-	0	0	24.86	115
CSH + $B_{2,0}; B_{4,0}$	1.98111 $\pm 0.00036$	1.98201 $\pm 0.00024$	-	5.740 $\pm 0.011$	0.0	4.9e-5 $\pm 1.1e-4$	6.3e-5 $\pm 1.0e-4$	-	-	0	0	24.76	115
GSH	1.98111 $\pm 0.00037$	1.98202 $\pm 0.00024$	-	5.740 $\pm 0.011$	0.0	4.7e-5 $\pm 1.1e-4$	6.9e-5 $\pm 1.1e-4$	-1.7e-4 $\pm 1.1e-4$	-4.5e-5 $\pm 1.1e-4$	0	0	24.49	115
Of eq. (5)													
CSH (eq. 1)	1.98134 $\pm 0.00023$	1.98196 $\pm 0.00016$	-	5.731 $\pm 0.006$	0.0	-	-	-	-	$\Theta=0.80$	0	17.54	115
CSH + $B_{2,0}; B_{4,0}$	1.98122 $\pm 0.00025$	1.98200 $\pm 0.00017$	-	5.736 $\pm 0.008$	0.0	1.6e-5 $\pm 7.7e-5$	7.0e-5 $\pm 7.3e-5$	-	-	$\Theta=0.80$	0	17.44	115
GSH with all terms of eq. (6)	1.98122 $\pm 0.00026$	1.98201 $\pm 0.00017$	-	5.736 $\pm 0.008$	0.0	1.4e-5 $\pm 7.7e-5$	7.5e-5 $\pm 7.4e-5$	-1.3e-4 $\pm 0.8e-4$	1.9e-5 $\pm 3.4$	$\Theta=0.80$	0	17.22	115
GSH with all terms of eq. (6)	1.98116 $\pm 0.00024$	1.98191 $\pm 0.00016$	-	5.737 $\pm 0.007$	0.0	3.8e-5 $\pm 7.2e-5$	5.0e-5 $\pm 6.8e-5$	-5.0e-5 $\pm 7.9e-5$	4.9e-6 $\pm 1.3e-3$	See text	See text	16.00	115
CSH	1.9803 $\pm 0.0004$	1.9818 $\pm 0.0002$	-	5.732 $\pm 0.009$	0.0	-	-	-	-	0	0	41.57	294
GSH with all terms of eq. (6)	1.9802 $\pm 0.0004$	1.9818 $\pm 0.0002$	-	5.742 $\pm 0.011$	0.0	2.5e-4 $\pm 1.0e-4$	8.8e-6 $\pm 1.2e-4$	1.0e-4 $\pm 1.3e-4$	4.5e-5 $\pm 6.5e-5$	0	0	41.13	294
SH of eq. 2	1.98043 $\pm 0.0004$	1.9819 $\pm 0.0002$	1.9799 $\pm 0.002$	5.734 $\pm 0.011$	$\leq 0.004$	-	-	-	-	0	0	41.52	294
SH of eq. 2 + all terms of eq. (6)	1.9801 $\pm 0.0005$	1.9819 $\pm 0.0003$	1.9804 $\pm 0.0025$	5.753 $\pm 0.014$	$\leq 0.0076$	3.0e-4 $\pm 1.1e-4$	4.0e-5 $\pm 1.2e-4$	1.1e-4 $\pm 1.3e-4$	4.4e-5 $\pm 1.3e-4$	0	0	40.99	294
Fully unconstrained $g$ and $D$ matrices	1.9808 $\pm 0.0007$	1.9817 $\pm 0.0002$	1.9821 $\pm 0.0008$	5.703 $\pm 0.007$	$\leq 0.0076$	-	-	-	-	0	0	23.74	294
Fully unconstrained $g$ and $D$ matrices + all terms of eq. (6)	1.9808 $\pm 0.0006$	1.9817 $\pm 0.0002$	1.9821 $\pm 0.0008$	5.705 $\pm 0.009$	$\leq 0.0077$	9.4e-6 $\pm 6.9e-5$	2.5e-5 $\pm 7.2e-5$	-6.9e-5 $\pm 7.7e-5$	-8.1e-5 $\pm 7.7e-5$	0	0	23.65	294

Description of spin Hamiltonian	$g_1$	$g_{\perp} (g_{xx})$	$g_{yy}$	$ D  (\text{GHz})$	$\eta$	$B_{2,0}$	$B_{4,0}$	$B_{4,3}$	$B_{4,-3}$	$\theta$ corr	$\phi$ corr	RMSD (G)	# resonance field measurements
CSH	1.9806 $\pm 0.0003$	1.9818 $\pm 0.0002$	—	5.732 $\pm 0.009$	0	—	—	—	—	0	0	36.55	280
GSH with all terms of eq. (6)	1.9806 $\pm 0.0003$	1.9818 $\pm 0.0002$	—	5.740 $\pm 0.010$	0	1.9e-4 $\pm 1.0e-4$	-5.9e-7 $\pm 1.0e-4$	1.7e-4 $\pm 1.2e-4$	3.3e-5 $\pm 5.8e-5$	0	0	36.18	280
SH of eq. 2	1.9807 $\pm 0.0004$	1.9818 $\pm 0.0003$	1.9816 $\pm 0.0024$	5.7304 $\pm 0.0038$	—	—	—	—	—	0	0	36.55	280
SH of eq. 2 + all terms of eq. (6)	1.9804 $\pm 0.0004$	1.9818 $\pm 0.0003$	1.9816 $\pm 0.0023$	5.745 $\pm 0.013$	$\leq 0.0051$	2.0e-4 $\pm 1.1e-4$	-1.4e-5 $\pm 1.1e-5$	1.7e-4 $\pm 1.1e-4$	3.0e-5 $\pm 1.2e-4$	0	0	36.16	280
Fully unconstrained $g$ and $D$ matrices	1.9813 $\pm 0.0004$	1.9818 $\pm 0.0002$	1.9813 $\pm 0.0016$	5.709 $\pm 0.0072$	$\leq 0.0072$	—	—	—	—	0	0	21.71	280
Fully unconstrained $g$ and $D$ matrices + all terms of eq. (6)	1.9803 $\pm 0.0008$	1.9818 $\pm 0.0002$	1.9822 $\pm 0.0008$	5.712 $\pm 0.009$	$\leq 0.0072$	2.5e-5 $\pm 6.7e-5$	-1.8e-5 $\pm 6.7e-5$	-1.1e-5 $\pm 7.2e-5$	6.5e-5 $\pm 7.2e-5$	0	0	21.67	280
CSH	1.9802 $\pm 0.0003$	1.9818 $\pm 0.0002$	—	5.728 $\pm 0.009$	0	—	—	—	—	0	0	39.85	297
Fully unconstrained $g$ and $D$ matrices	1.9808 $\pm 0.0015$	1.9818 $\pm 0.0001$	1.9813 $\pm 0.0003$	5.698 $\pm 0.007$	$\leq 0.009$	—	—	—	—	0	0	22.39	297
Fully unconstrained $g$ and $D$ matrices and angle offset optimization	1.9812 $\pm 0.0002$	1.9821 $\pm 0.0011$	1.9817 $\pm 0.0002$	5.725 $\pm 0.006$	$\leq 0.002$	—	—	—	—	$\delta\theta_1 = 0.75$ $\epsilon_0 = 0.0$ (see text)	$\delta\gamma = 0.0$ $\epsilon_7 = 0.03$ (see text)	19.95	297

Table 3 Root mean-square deviations (RMSD) of simulated resonance fields from observed resonance fields.  $B_{l,m}$  are HSZ parameters discussed in the text. See the text for information about  $\delta\theta$  values used in certain fits. Extremely large errors (e.g., data row 3, data col. 9) indicate that the impact of that parameter on the computed resonance fields is negligible for the angular orientations of the fitted data.

## References

- [1] A. A. Manenkov, A. M. Prokhorov, *J. Exp. Theor. Phys. (USSR)* 28 (1955) 762.
- [2] A. A. Manenkov, A. M. Prokhorov, *Sov. Phys. JTEP* 1 (1955) 611.
- [3] G. M. Zverev, A. M. Prokhorov, *J. Exp. Theor. Phys. (USSR)* 34 (1958) 513.
- [4] G. M. Zverev, A. M. Prokhorov, *Sov. Phys. JTEP* 7 (1958) 354.
- [5] J. E. Geusic, *Phys. Rev.* 102 (1956) 1252.
- [6] M. M. Zaripov, I. I. Shamoinin, *J. Exp. Theor. Phys. (USSR)* 30 (1956) 291.
- [7] M. M. Zaripov, I. I. Shamoinin, *Sov. Phys. JTEP* 3 (1956) 171.
- [8] E. O. S.-D. Bois, *Bell Sys. Tech. J.* 38 (1959) 271.
- [9] H. Klein, U. Scherz, M. Schulz, H. Setyono, K. Wisnewski, *Z. Phys. B* 28 (1977) 149.
- [10] G. Kido, N. Miura, *Appl. Phys. Lett.* 41 (1982) 569.
- [11] R. W. Terhune, J. Lambe, C. Kikuchi, J. Baker, *Phys. Rev.* 123 (1961) 1265.
- [12] T. Chang, D. Foster, A. H. Kahn, *J. Res. NBS* 83 (1978) 133.
- [13] A. Abragam, M. H. L. Pryce, *Proc. Royal Soc. A* 205 (1951) 135.
- [14] A. B. Roitsin, *Phys. Stat. Sol. (b)* 104 (1981) 11.
- [15] D. G. McGavin, W. C. Tennant, J. A. Weil, *J. Mag. Res.* 87 (1990) 92.
- [16] H. A. Buckmaster, R. Chaterjee, Y. H. Shing, *J. Mag. Res.* 4 (1971) 85.
- [17] V. G. Grachëv, *Sov. Phys. JTEP* 65 (1987) 1029.
- [18] S. Geschwind, *Phys. Rev.* 121 (1961) 363.
- [19] G. F. Koster, H. Statz, *Phys. Rev.* 113 (1959) 445.
- [20] H. A. Buckmaster, R. Chaterjee, Y. H. Shing, *Phys. Stat. Sol. A* 13 (1972) 9.
- [21] B. Bleaney, *Hyperfine Interactions*, Academic Press, New York 1967.
- [22] B. Bleaney, *Proc. Phys. Soc. A* 73 (1959) 939.
- [23] S. A. Alt'shuler, B. M. Kozirev, *Electron Paramagnetic Resonance in Compounds of Transition Elements*, John Wiley & Sons, New York 1972.
- [24] W. J. C. Grant, M. W. P. Strandberg, *J. Phys. Chem. Sol.* 25 (1964) 635.
- [25] G. Bacquet, J. Dugas, C. Escribe, J. M. Gaite, J. Michoulier, *J. Chem. Phys. C* 7 (1974) 1551.
- [26] J. Michoulier, J. M. Gaite, *J. Chem. Phys.* 56 (1972) 5205.
- [27] D. S. Schonland, *Molecular Symmetry: An Introduction to Group Theory and its Uses in Chemistry*, Van Nostrand Reinhold Co., London 1965.
- [28] W. M. Yen, *Preparation of Single Crystal Fibers*, World Scientific, Singapore 1995.
- [29] D. A. Schwartz, E. D. Walter, S. J. McIlwain, V. N. Krymov, D. J. Singel, *Appl. Magn. Reson.* 16 (1999) 223.
- [30] M. J. Mombourquette, J. A. Weil, D. G. McGavin, University of Saskatchewan, Saskatoon 1993.
- [31] A. Abragam, B. Bleaney, *Electron Paramagnetic Resonance of Transition Ions*, Clarendon Press, Oxford 1970.
- [32] F. S. Ham, G. W. Ludwig, G. D. Watkins, H. H. Woodbury, *Phys. Rev. Lett.* 5 (1960) 468.
- [33] R. M. Macfarlane, *J. Chem. Phys.* 39 (1963) 3118.
- [34] R. M. Macfarlane, *J. Chem. Phys.* 42 (1965) 442.
- [35] R. M. Macfarlane, *Phys. Rev. B* 1 (1970) 989.
- [36] S. Sugano, Y. Tanabe, *J. Phys. Soc. Jap.* 13 (1958) 880.
- [37] D. E. Rimmer, D. F. Johnston, *Proc. Phys. Soc.* 89 (1966) 943.
- [38] C. Kikuchi, J. Lambe, G. Makhov, R. W. Terhune, *J. Appl. Phys.* 30 (1959) 1061.

## **Appendix IV**

### **C++ Code for Simulation of Rapid Passage Effects in EPR**

# Numerical Simulation of the Bloch Equations In CW-EPR

## I. Introduction

This document discusses methods to simulate CW-EPR spectra through numerical integration of the bloch equations.

## II. Equations & Theory

The magnetization vector,  $\hat{M}$ , is defined as:

$$\hat{M} = \begin{pmatrix} M_x \\ M_y \\ M_z \end{pmatrix}$$

When a collection of spins resting at equilibrium  $\hat{M}^o = \begin{pmatrix} 0 \\ 0 \\ M_o \end{pmatrix}$  are submitted to a

modulated magnetic field  $\rho(t)$  (shown below) along the z-axis and microwaves at amplitude power  $H_1$  along the x-axis of the rotating frame, their behavior is defined via the following differential equations:

$$\frac{\partial \hat{M}}{\partial t} = \begin{pmatrix} -\frac{1}{T_2} & -\gamma \cdot \rho(t) & 0 \\ \gamma \cdot \rho(t) & -\frac{1}{T_2} & -\gamma \cdot H_1 \\ 0 & \gamma \cdot H_1 & -\frac{1}{T_1} \end{pmatrix} \cdot \hat{M} + \begin{pmatrix} 0 \\ 0 \\ \frac{M_o}{T_1} \end{pmatrix}$$

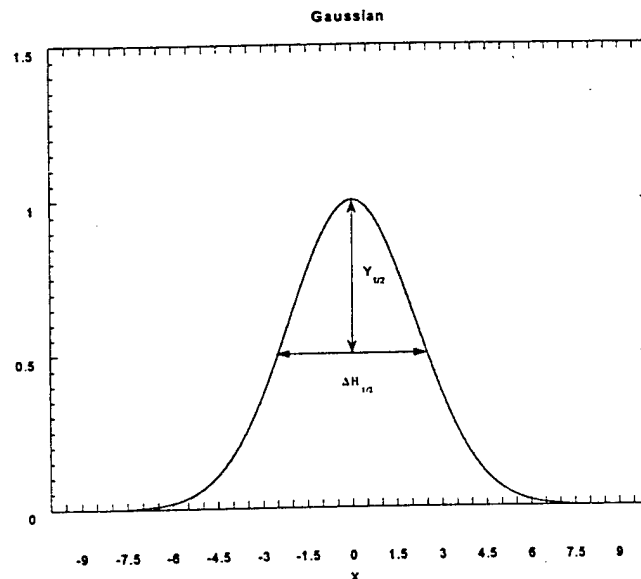
$$\rho(t) = H_o - (H_c + H_m \cos(\omega_m \cdot t))$$

Where  $T_1$  and  $T_2$  are the relaxation rates,  $\gamma$  is the gyro-magnetic ratio for a free electron,  $H_o$  is the resonant field,  $H_c$  is the current field,  $\omega_m$  is the modulation frequency (rad/sec), and  $H_m$  is the modulation amplitude. The Jacobian is obtained below for use with other simulation methods, such as LSODES, a stiff numerical integration method in the ODEPACK bunch of FORTRAN programs.

$$J = \begin{pmatrix} \frac{\partial \hat{M}_x}{\partial t \cdot \partial \hat{M}_x} & \frac{\partial \hat{M}_x}{\partial t \cdot \partial \hat{M}_y} & \frac{\partial \hat{M}_x}{\partial t \cdot \partial \hat{M}_z} \\ \frac{\partial \hat{M}_y}{\partial t \cdot \partial \hat{M}_x} & \frac{\partial \hat{M}_y}{\partial t \cdot \partial \hat{M}_y} & \frac{\partial \hat{M}_y}{\partial t \cdot \partial \hat{M}_z} \\ \frac{\partial \hat{M}_z}{\partial t \cdot \partial \hat{M}_x} & \frac{\partial \hat{M}_z}{\partial t \cdot \partial \hat{M}_y} & \frac{\partial \hat{M}_z}{\partial t \cdot \partial \hat{M}_z} \end{pmatrix}$$

$$J = \begin{pmatrix} -\frac{1}{T_2} \frac{\partial M_x}{\partial M_x} - \gamma \frac{\partial \rho(t)}{\partial M_x} M_y - \gamma \rho(t) \frac{\partial M_y}{\partial M_x} & -\frac{1}{T_2} \frac{\partial M_x}{\partial M_y} - \gamma \frac{\partial \rho(t)}{\partial M_y} M_y - \gamma \rho(t) \frac{\partial M_y}{\partial M_y} & -\frac{1}{T_2} \frac{\partial M_x}{\partial M_z} - \gamma \frac{\partial \rho(t)}{\partial M_z} M_y - \gamma \rho(t) \frac{\partial M_y}{\partial M_z} \\ \frac{\partial \gamma \rho(t)}{\partial M_x} M_x + \gamma \rho(t) \frac{\partial M_x}{\partial M_x} - \frac{1}{T_2} \frac{\partial M_y}{\partial M_x} - \gamma H_1 \frac{\partial M_z}{\partial M_x} & \frac{\partial \gamma \rho(t)}{\partial M_x} M_x + \gamma \rho(t) \frac{\partial M_x}{\partial M_y} - \frac{1}{T_2} \frac{\partial M_y}{\partial M_y} - \gamma H_1 \frac{\partial M_z}{\partial M_y} & \frac{\partial \gamma \rho(t)}{\partial M_x} M_x + \gamma \rho(t) \frac{\partial M_x}{\partial M_z} - \frac{1}{T_2} \frac{\partial M_y}{\partial M_z} - \gamma H_1 \frac{\partial M_z}{\partial M_z} \\ \gamma H_1 \frac{\partial M_y}{\partial M_x} - \frac{1}{T_1} \frac{\partial M_z}{\partial M_x} & \gamma H_1 \frac{\partial M_y}{\partial M_y} - \frac{1}{T_1} \frac{\partial M_z}{\partial M_y} & \gamma H_1 \frac{\partial M_y}{\partial M_z} - \frac{1}{T_1} \frac{\partial M_z}{\partial M_z} \end{pmatrix}$$

$$J = \begin{pmatrix} -\frac{1}{T_2} & -\gamma \rho(t) & 0 \\ \gamma \rho(t) & -\frac{1}{T_2} & -\gamma H_1 \\ 0 & \gamma H_1 & -\frac{1}{T_1} \end{pmatrix}$$



The line-shape function  $L(H)$  will be defined as (see above):

$$L(H) = e^{-\ln 2 \cdot \left( \frac{H_0 - H}{\frac{1}{2} \Delta H_{1/2}} \right)^2}$$

Others line-shape functions may later be implemented (e.g. Lorentzian, Voigt) and or powder patterns generated by program and/or experiments. This document will deal with the basic gaussian function so that the implementation can be checked for errors and/or inconsistencies before writing additional functionality.

The solutions to the equations at different offset values ( $H_c$ ) are called wavepackets or spinpackets throughout this document. A multitude of packets with  $H_c$  ranging from  $-H_{\max}$  to  $+H_{\max}$  in increments of  $H1$  (G) or  $1/T2$  (G), depending on which is smaller (increment value is deemed  $dH$ ), are created to be used to simulate a spectrum using the equations below.

$H_i$  is then defined as

$$H_i = H_{s,i} - H_{c,i}$$

The spinpackets are then summed up over the line shape function through the equation:

$$(1) \sum_j(t) = \sum_{i=0}^{n=\text{number\_of\_packets}} L(H_i) \cdot \text{packets}_i(t) \cdot dH$$

The spectrum for the 0 & 90 degrees out of phase is then extracted by calculating the fourier coefficients for each  $\text{pt}(j)$  on the line using (2) & (3)

$$(2) \text{spectra}^{0,h}_j = \sum_{t=t_o}^{t_{\max}} \sum_j(t) \cdot \cos(h \cdot \omega_m t) \cdot \frac{2 \cdot dt}{(t_{\max} - t_o)}$$

$$(3) \text{spectra}^{90,h}_j = \sum_{t=t_o}^{t_{\max}} \sum_j(t) \cdot \cos(h \cdot \omega_m t + \frac{\pi}{2}) \cdot \frac{2 \cdot dt}{(t_{\max} - t_o)}$$

$$h \geq 1$$

$\text{spectra}^{0,h}$  and  $\text{spectra}^{90,h}$  is calculated for the  $M_x$  and  $M_y$  packet set. Small  $h$  in these equations is the integral harmonic spectrum (relative to modulation), to be extracted.

### III. Programming Method

Using fourth order Runge-Kutta integration methods, a program was written in Matlab to produce a plot of one Wavepacket,  $M_x, M_y$ , and  $M_z$  as a function of time. Later, an offsets were added for the acquisition of an evenly spaced array of wavepackets, with the offset depending on  $H_1$  (G) or  $1/T_2$  (G), whichever was smallest. Due to the relative inefficient of the interpreted language in Matlab, a C version of the code on a UNIX system was implemented, thus giving rise to the blochc programs. As a result, wavepackets were simulated in ~360 fold less time than the Matlab product. Further improvements were added to automatically catch and handle when the integration "blows-up", i.e. the magnetization vector components absolute values become larger than a programmed ceiling value.

After the method for simulating multiple wavepackets in a reasonable amount of time was formulated, a new program called spec was implemented. This program takes the output wavepackets from the blochc program. After subtracting the packet offsets, for each point on the spectrum, spec sums the wavepackets with the gaussian function weight centered around the selected point and demodulates the composite Wavepacket time to obtain the Fourier coefficient. The Fourier coefficients are calculated for each point on the spectral line. Using the demodulation function, a  $n^{\text{th}}$  harmonic spectrum can also be produced. The current version of spec only implements the 1<sup>st</sup> and 2<sup>nd</sup> harmonic of the calculation.

### IV. Performance & Data Analysis

To quantify the performance of the blochc program, several factors have to be considered. Some these factors include, but are not limited to, modulation frequency, modulation amplitude,  $T_2$  values, and Wavepacket offset. These all effect the step size required by the Runge-Kutta method to produce a "reliable" result. This section will play with the parameters of the blochc program while measuring the amount of time required to finish the Wavepacket. First, we will deal with a spinpacket with offset of zero, varying the parameters that may affect the performance of the program. Nine runs will be averaged to obtain the proper spectrum. The computer used will be an Octane 250MHz computer running DEC UNIX (version?). The parameters and results for the center wavepackets are shown below in Table I below.

**Table I – Performance Analysis Using the Central Spinpacket**

Run #	H1 (G)	T1 (sec)	T2 (sec)	Hv (Hz)	Hm (G)	Cycles	Date/Time	Time Completed
1	0.065	18e-6	1e-6	500	0.5	3		
2	0.065	18e-6	1e-6	1000	0.5	3		
3	0.005	18e-6	1e-6	500	0.5	3		
4	0.005	18e-6	1e-6	1000	0.5	3		
5	0.065	36e-6	1e-6	500	0.5	3		
6	0.065	36e-6	1e-6	1000	0.5	3		
7	0.005	36e-6	1e-6	500	0.5	3		
8	0.005	36e-6	1e-6	1000	0.5	3		
9	0.065	18e-6	1e-6	500	1.0	3		
10	0.065	18e-6	1e-6	1000	1.0	3		
11	0.005	18e-6	1e-6	500	1.0	3		
12	0.005	18e-6	1e-6	1000	1.0	3		

#### IV. Conclusion

##### A. Usage of the blochc4 program

This is the command line for running blochc4.

> *Blochc4 <packets> <substeps> <fps> <Hm> <v> <H1> <T1> <T2> <cycles> <filename>*

<i>&lt;packets&gt;</i>	(integer) The number of packets to calculate. The packets are offset by H1 at each iteration, i.e. Offset of 1 <sup>st</sup> packet will be (H1(G) or 1/T2(G))*(packets/2-1), center packet will have an resonance offset of zero. This will only apply if <packets> is an odd integer, otherwise, no calculation of the zero offset will be performed.
<i>&lt;substeps&gt;</i>	(integer) Initial number of substeps between points to take. Program will adjust this number to obtain a “non-blowup” result of the simulation.
<i>&lt;fps&gt;</i>	(integer) Number of points to save to a file. File format will be discussed below.
<i>&lt;Hm&gt;</i>	(real) ½ the desired modulation height (G) for the simulation. Okay to set to zero if no modulation is desired.
<i>&lt;v&gt;</i>	(real) Modulation frequency (Hz)
<i>&lt;H1&gt;</i>	(real) Microwave power amplitude (G).
<i>&lt;T1&gt;</i>	(real) Relaxation Rate (sec)
<i>&lt;T2&gt;</i>	(real) Relaxation Rate (sec)
<i>&lt;cycles&gt;</i>	(integer) Number of modulation cycles to run simulation. Must be at least one.
<i>&lt;filename&gt;</i>	(file string) filename of where the results are to be saved. When blochc4 is done, the results are saved in the ./work directory of where blochc4 is run. For proper operation, make sure that the ./work directory exists.

File format of blochc4 program is in ASCII text. When given a filename, blochc4 creates three files. Two of these files are <filename>x.red and <filename>y.red which are the Mx and My components of the magnetization vector as a function of time. In the first row of the file is the offsets that were used for each Wavepacket. The 1<sup>st</sup> column contains the time vector that was used. The remaining columns are for the magnetization components that were calculated for each Wavepacket. The third file contains the parameters that were used to calculate the simulation (<filename>.par).

## B. Usage of spec programs

This is the command line for running the spec program.

```
> spec <basefile> <points> <linewidth> <bfield> <efield> <Center>
```

<basefile>	(filename string) Wavepacket filename. Notice that this is the basfilename, i.e., when calculating a spectrum from the wavepackets generated using <filename> above, only use the filename as entered into the blochc4 program. This program will append to appropriate extension and load in the Mx and My components of the simulation. Also note that spec expects to read from the same ./work directory as blochc4 does.
<points>	(integer) Number of data that you want calculated with the spectrum. (1000 usually used).
<linewidth>	(real) Linewidth of the gaussian function (1/2 height) of which you are calculating
<bfield>	(real) beginning field of spectrum. Note : this needs to be less than <efield>.
<efield>	(real) ending field of spectrum.
<Center>	(real) point in the spectrum where the gaussian function reaches its maximum (central) value.

This program will generate two files, one for the spectra calculated using the Mx component ( called <basefile>x.spec) and the other for the My component (called <basefile>y.spec).

## C. Usage of bspec scripting program

Here is the command line for the bspec UNIX script.

```
Bspec2 <packets> <subpts> <packetpts> <Hm> <v> <HI> <T1> <T2> <cycles>
<spec pts> <linewidth> <bfield> <efield> <center> <basefile>
```

Bspec2 combines the functionality of blochc4 and spec. The parameters are analogous as in the above charts for blochc4 and spec. This program will generate the spectrum given the parameters for blochc4 and for spec. The results are saved as <basefile>x.spec, <basefile>y.spec, and <basefile>.par. The magnetization components calculated for blochc4 are deleted after the spectrum is calculated. This reduces disk space usage and allows a more efficient way of obtaining spectra.

## D. Usage of genpar programs

The genpar type programs work to generate a scripting file that will perform multiple runs of the bspec program. Basic command line is as follows.

```
Genpar <tol> <linewidth> <HI> <T1> <T2> <Hm> <specwidth> <points>
<nfreq> <freqoff> <basefile>
```

<i>&lt;Tol&gt;</i>	(real) Specified tolerance of gaussian line, i.e. number of wavepackets to calculate such that on a central line of a gaussian function, the value is equal or less this tolerance level.
<i>&lt;Linewidth&gt;</i>	Linewidth of gaussian function (G)
<i>&lt;H1&gt;</i>	(real) Microwave power amplitude (G).
<i>&lt;T1&gt;</i>	(real) Relaxation Rate (sec)
<i>&lt;T2&gt;</i>	(real) Relaxation Rate (sec)
<i>&lt;Hm&gt;</i>	(real) $\frac{1}{2}$ the desired modulation height (G) for the simulation. Okay to set to zero if no modulation is desired.
<i>&lt;Specwidth&gt;</i>	(real) Width of spectrum (G)
<i>&lt;Points&gt;</i>	(integer) Number of points in the spectrum
<i>&lt;Nfreq&gt;</i>	(integer) Number of modulation frequencies to calculate
<i>&lt;Freqoff&gt;</i>	(real) Modulation frequency offset between runs
<i>&lt;Basefile&gt;</i>	(filename string) Filename of the set of generated spectra.

## E. Further Programming Ideas

- 1) In the spec program, the only linshape function (L(H) as above) applied is a gaussian. More functions would be desirable. Another improvement would be to read in a calculated powder spectrum or other generated spectrums, and run the spec program, interpolating between the calculated values for the weight values of each spin packet.
- 2) Adaptive step sizes to reduce integration errors should be introduced. This would allow a more accurate simulation of the spinpacket magnetization values as a function of time, giving a more reliable spectrum overall. With the current blochc program, the wavepackets out on the wings are the most inaccurate. The inner wavepackets, require a smaller step size to be as accurate as the outside, but the constant stepsize causes them to overstep. Using an adaptive stepsize would not only increase the robustness of the calculations for the outer packets, but would most likely improve overall performance, due to a smaller required step size for the inner packets.

## F. Source Listing .

### Bspec2

```

#!/bin/csh -f

#1 - spinpackets
#2 - subpoints
#3 - packet points
#4 - Hm
#5 - Modulation Frequency (Hz)
#6 - Microwave Power (G)
#7 - T1 (sec)
#8 - T2 (sec)
#9 - cycles
#10 - spec points
#11 - linewidth
#12 - begin field
#13 - end field

```

#14 - Center  
#15 - Base File  
.blochc4 \$1 \$2 \$3 \$4 \$5 \$6 \$7 \$8 \$9 \$15  
.spec \$15 \$10 \$11 \$12 \$13 \$14  
rm ./work/\*.red

---

```

/* port of Sean McIlwain's matlab code for integrating the Bloch equations.
*
*
*  port of file blochc.m
* Sean's comments are preceded by '%' characters.
*/
/*
%Bloch Equations for EPR
%Will Aproxiamate the Bloch Equations given the parameters
%Using Bloch4 Function
%
%H1 - microwave field
%
% - Center of Resonance
%T1
%T2
*/
#include <string.h>
#include <stdio.h>
#include <stdlib.h>
#include <strings.h>
#include <math.h>
#include <malloc.h>
#include "sutil.h"
/*#include "bdef.h"*/
#include "blochb.h"

#define MinPacketStep 0.05
#define FACTOR 100
/*#define MAXBUF 80*/



/* I suppose this is the main program */
void main(int argc, char *argv[])
{
    /* argv[1] = spinpackets
    argv[2] = substeps
    argv[3] = filepoints
    argv[4] = Hm (1/2 Modamp (Gauss)
    argv[5] = v (Mod Freq in Sec^-1)
    argv[6] = H1 (Gauss)
    argv[7] = T1 (Sec)
    argv[8] = T2 (Sec)
    argv[9] = cycles
    argv[10] = filename
    */
    { /* beginning of main program */

    /*
    %Parameters - Function
    */

    long i,j;
    long filepoints;
    long spinpackets;
    long points;
    long subpoints;
    int Blowup;
    double modfreq; /* Hz */
    /*double pi = 3.1415927; */
    double Wm; /* Modulation Frequency (v(Hz)*2*pi) */
    double Hm; /* Modulation Amplitude (Gauss) */
    double T1; /* in sec */
    double T2; /* in sec */
    double H1; /* in Gauss */
    double Ho = 0; /* Center of Resonance (Gauss) */
    double Mc = 1; /* Lineshape Height */
    double k = 1/2; /* Lineshape Width */
    double offset; /* Offset to calculate for spin packet */
    double deltaH; /* Number of spin packets to calculate */
    double stepsize;
    long cycles;
}

```

```

long Hc_size;
double *Hc;
double *timearray;
double maxtime;
double Mo = 1;
double time;
double dt;
double mintime;
double temptime;
bloch_par b_par;

/*
%Parameters - Integration
*/

/*
%Parameters - File saving
*/
char param[300];

double *Mnext; /* defined by calloc, used as M[points][4] in bloch4.c */

double *hsave;

double **sresultx;
double **sresulty;
double **sresultz;

double *tempx,*temp2x;
double *tempy,*temp2y;
double *tempz,*temp2z;

/* assigning filenames */
char filedir[MAXBUF] = "./work/";
char filename[MAXBUF];
char filename2x[MAXBUF];
char filename2y[MAXBUF];
char filename2z[MAXBUF];
char filename3 [MAXBUF];
FILE *file1, *file2, *file3;

if (argc != 11)
{
    printf ("Insufficient # of arguments\n");
    printf ("Usage blochc <packets> <substeps> <fps> <Hm> <v>\n");
    printf ("<H1> <T1> <T2> <cycles> <filename>\n");
    exit(-1);
}
else
{
    spinpackets = atoi(argv[1]);
    subpoints = atoi(argv[2]);
    filepoints = atoi (argv[3]);
    points = filepoints;
    /*
    Hm = atof(argv[4]);
    modfreq = atof(argv[5]);
    H1 = atof(argv[6]);
    T1 = atof(argv[7]);
    T2 = atof(argv[8]);
    */
    modfreq = atof(argv[5]);
    b_par.Mo = 1;
    b_par.H1 = atof(argv[6]);
    b_par.T1 = atof(argv[7]);
    b_par.T2 = atof(argv[8]);
    b_par.Hm = atof(argv[4]);
    b_par.Wm = atof(argv[5]) * 2.0 * pi;
}

```

```

b_par.H0 = 0.0;
cycles = atoi(argv[9]);
strcpy(filename,argv[10]);

filename2x[0] = '\0';
strcpy(filename2x,filedir);
strcat(filename2x,filename);
strcat(filename2x,"x.red");

filename2y[0] = '\0';
strcpy(filename2y,filedir);
strcat(filename2y,filename);
strcat(filename2y,"y.red");

filename2z[0] = '\0';
strcpy(filename2z,filedir);
strcat(filename2z,filename);
strcat(filename2z,"z.red");

filename3[0] = '\0';
strcpy(filename3,filedir);
strcat(filename3,filename);
strcat(filename3,".par");

/* Wm = 2*pi*modfreq; */
maxtime = (double)(cycles+1) * (1.0/modfreq);
mintime = (1/modfreq);
deltaH = (double) spinpackets;

if ((1/b_par.T2/HzperGauss) < b_par.H1)
{
    stepsize = 1/b_par.T2/HzperGauss;
}
else
{
    stepsize = b_par.H1;
}
if (MinPacketStep >= stepsize)
{
    stepsize = MinPacketStep;
}

offset = (deltaH-1.0)/2.0 * stepsize;
Hc_size = spinpackets+1;

printf ("\nSpinpackets = %d\n",spinpackets);
printf ("points = %d\n",points);
printf ("filepoints = %d\n",filepoints);
printf ("Hm = %f\n",b_par.Hm);
printf ("Wm = %f\n",b_par.Wm);
printf ("H1 = %f\n",b_par.H1);
printf ("T1 = %f\n",b_par.T1);
printf ("T2 = %f\n",b_par.T2);
printf ("cycles = %d\n",cycles);
printf ("filename = %s\n",filename);
printf ("maxtime = %f \n",maxtime);
printf ("offset = %f \n",offset);
printf ("DeltaH = %f \n",deltaH);
printf ("stepsize = %f \n",stepsize);
printf ("Hc_size = %d \n",Hc_size);

}

printf("ready to calloc \n");

/* from seanutil.c */
hsave = array(Hc_size);
Hc = array(spinpackets);

```



```

timearray[0] = time;
sresultx[0][0] = time;
sresulty[0][0] = time;
/*sresultz[0][0] = time; */
i = 1;

printf ("Entering Integration Loop \n");
while ((Blowup == FALSE) && (i < filepoints))
{
    /*printf ("Filepoint # %d of %d\n",i,filepoints); */
    /*printf ("Calling substep\n"); */
    Blowup = substep(Mnext,Hc[j],b_par,&time,dt,subpoints);

    if (Blowup == FALSE)
    {

        /*printf ("time = %f\n",time); */
        timearray[i] = time;
        sresultx[i][0] = time;
        sresulty[i][0] = time;
        /*sresultz[i][0] = time; */
        /*printf ("sresultx[%d][0] = %f\n",i,time); */

        /*if (i%100 == 0)
        {
            printf ("Assigning #%d to sresult[%d]\n",i,j+1);
        } */
        sresultx[i][1] = Mnext[1];
        sresulty[i][1] = Mnext[2];
        /*sresultz[i][1] = Mnext[3]; */
        i++;
    }

} /* end of while ((Blowup == FALSE) && (i < filepoints)) */

if (Blowup == TRUE)
{
    i = 0;
    time = 0.0;
    Mnext[0] = 0.0;
    Mnext[1] = 0.0;
    Mnext[2] = 0.0;
    Mnext[3] = Mo;
    j = 0;
    printf ("\nBlew up, trying %d + %d",subpoints,FACTOR);
    subpoints = subpoints + FACTOR;
    printf (" = %d\n",subpoints);
}
}

//Now have a substep that doesn't cause the program to blow up
//generate cos array for mass scale integration.
//gencos (b_par.Wm,dt);
printf ("Starting second integration\n");

for (j=1;j<spinpackets;j++)
{
    time = 0.0;

    Mnext[0] = 0;
    Mnext[1] = 0;
    Mnext[2] = 0;
    Mnext[3] = b_par.Mo;
    /*
     *calculate M up to min time in hopes of removing the
     *transient from the spectrum
     */
    printf ("Advancing time to %g\n",mintime);
    while (time < mintime)
    {
        /*

```

```

*substep is a procedure that affects time and Mnext
*it basically calculates the next value(s) of the
*magnetization vector and time, given dt. It also
*has a feature that it returns an error value to
*which signifies a blowup state. Using this state,
*rest of the program can determine if it needs to
*increase the # of substeps for which to take
*/
Blowup = substep(Mnext,Hc[j],b_par,&time,dt,subpoints);
} /*end of while ((time < mintime))*/
printf ("Current time is %lg\n",time);
sresultx[0][j+1] = Mnext[1];
sresulty[0][j+1] = Mnext[2];
sresultz[0][j+1] = Mnext[3];

/*printf ("Entering Integration Loop \n");*/

}

printf ("Into integration\n");
cosarray = array (subpoints+1);
cosarrayh = array (subpoints);

for (i=1;i < points;i++)
{
//printf ("point # %d\n",i);
//printf ("time %lg\n",timearray[i]);
temptime = timearray[i];
tempx = sresultx[i-1];
tempy = sresulty[i-1];
tempz = sresultz[i-1];

temp2x = sresultx[i];
temp2y = sresulty[i];
temp2z = sresultz[i];

gencos2 (modfreq,b_par.Hm,temptime,dt,subpoints+1,cosarray);
gencos2 (modfreq,b_par.Hm,temptime+0.5*dt,dt,subpoints,cosarrayh);

for (j=1; j < spinpackets;j++)
{
    time = temptime;
    Mnext[0] = time;
    //Mnext[1] = sresultx[i-1][j+1];
    //Mnext[2] = sresulty[i-1][j+1];
    //Mnext[3] = sresultz[i-1][j+1];

    Mnext[1] = tempx[j+1];
    Mnext[2] = tempy[j+1];
    Mnext[3] = tempz[j+1];

    /*printf ("Filepoint # %d of %d\n",i,filepoints);*/
    //printf ("Calling substep\n");
    Blowup = substep(Mnext,Hc[j],b_par,&time,dt,subpoints);
    /*if (i%100 == 0)
    {
        printf ("Assigning #%d to sresult[%d]\n",i,j+1);
    }*/
    //printf ("Assigning values\n");
    //sresultx[i][j+1] = Mnext[1];
    //sresulty[i][j+1] = Mnext[2];
    //sresultz[i][j+1] = Mnext[3];
    temp2x[j+1] = Mnext[1];
    temp2y[j+1] = Mnext[2];
    temp2z[j+1] = Mnext[3];
}

/* end of for (j < spinpackets)*/

} /*end of for (i < points)*/

```

```

hsave[0] = 0;
for (i = 1; i < (Hc_size); i = i + 1)
{
    hsave[i] = Ho-Hc[i-1]; /* %Place Delta as a header */
}

/*
%Save Files
%eval (['save ' filename1x ' savefile1x -ascii -tabs -double']);
*/
printf("deltaH = %f \n",deltaH);
printf("filepoints = %d \n",filepoints);

printf("now opening file1 \n");
file1 = fopen(filename2x,"w");
if (!file1)
{
    printf("file1 opening seems to have failed\n");
    exit(-1);
}
else
printf("file1 opening seems to have succeeded \n");

for (j = 0; j < Hc_size ; j++)
{
    fprintf(file1,"%g\t",hsave[j]);
}
fprintf(file1,"\n");
for (j = 0; j < filepoints; j = j + 1)
{
    /*printf("j = %d \n",j); /* */

    /*fprintf(file1,"%g\t",sresultx[j][(int)deltaH]);*/

    for (i = 0; i < Hc_size; i = i + 1)
    {
        /*          printf("In Loop\n");
        printf("sresultx[%d][%d] = %f \n",j,i,sresultx[j][i]);
        */
        fprintf(file1,"%g\t",sresultx[j][i]);
    }
    fprintf(file1,"\n");
}
fclose(file1);

/*
%eval (['save ' filename1y ' savefile1y -ascii -tabs -double']);
*/
printf("now opening file2 \n");
file2 = fopen(filename2y,"w");
/* fprintf(file2,"%f %f\n",hsave[0],hsave[1]); /* */
for (j = 0; j < Hc_size ; j++)
{
    fprintf(file2,"%g\t",hsave[j]);
}
fprintf(file2,"\n");
for (j = 0; j < filepoints; j = j + 1)
{
    /*fprintf(file2,"%g\t",sresulty[j][(int)deltaH]);*/
    for (i = 0; i < Hc_size; i = i + 1)
    {
        fprintf(file2,"%g\t",sresulty[j][i]);
    }
    fprintf(file2,"\n");
}

```

```

        }
fclose(file2);

/*
%eval (['save ' filename1z ' savefile1z -ascii -tabs -double']);
 */
/*
printf("now opening file3 \n");
file3 = fopen(filename2z,"w");

for (j = 0; j < Hc_size ; j++)
{
    fprintf(file3,"%g\t",hsave[j]);
}
fprintf(file1,"\n");
for (j = 0; j < filepoints; j = j + 1)
{
    for (i = 0; i < Hc_size; i = i + 1)
    {
        fprintf(file3,"%g\t",sresultz[j][i]);
    }
    fprintf(file3,"\n");
}
fclose(file3);
*/
printf("now opening file1 again \n");
file1 = fopen(filename3,"w");
fprintf(file1,"%s\n",param);

fclose(file1);

free_matrix (sresultx,filepoints);
free_matrix (sresulty,filepoints);
/*free_matrix (sresultz,filepoints); */
free_array (Mnext);

} /* end of main program */

```